The micro-layered fast-neutron detector

by

Priyarshini Ghosh

B.E., Birla Institute of Technology, India, 2015

AN ABSTRACT OF A DISSERTATION

submitted in partial fulfillment of the requirements for the degree

DOCTOR OF PHILOSOPHY

Alan Levin Department of Mechanical & Nuclear Engineering
Carl R. Ice College of Engineering

KANSAS STATE UNIVERSITY
Manhattan, Kansas

2021

Abstract

The Micro-Layered Fast-Neutron Detector (MLFD) is a novel fast-neutron detection technology that has been developed from concept stage to demonstrable functionality in a laboratory environment. The MLFD boasts a high fast-neutron detection efficiency of 9.2% at 43 mm length-of-detector, a near-100% gamma-ray rejection capability without requiring pulse shape discrimination or any additional electronics or techniques, and suppression of Ĉerenkov radiation generation inherently by design. These features have been achieved by careful material selection in suitable geometrical fashion. Polymethyl methacrylate (PMMA) was used as a neutron converter (by proton recoil) and light guide, and zinc sulfide as an inorganic scintillator, in an alternating layer configuration such as to maximize scintillation photon collection from neutron interactions while minimizing Ĉerenkov generation. A photodetector attaches to the side of the MLFD, which can either be a photomultiplier tube (PMT) or a silicon photomultiplier (SiPM), depending on the application desired. The orientation of the photodetector on the side (parallel to the longest length of the MLFD) also reduces probability of forward-propagational Ĉerenkov photons from being collected. The detection efficiency can also be scaled by simply increasing the number of layers, i.e., the length of the detector. The vastly different decay pulse times for protons (700 ns to 10,000 ns) and electrons (12 ns) leads to a very distinct neutron and gamma-ray event separation, leading to a PSD ratio of 4.56. Furthermore, replacing the PMT with SiPMs reduces the Ĉerenkov radiation developed in the PMT photocathode window, thereby eliminating the need for pulse shape discrimination altogether, and only requires a low LLD to reject almost all gamma radiation.

Although originally designed for use at the TREAT facility of Idaho National Laboratory, the MLFD has exhibited performance that makes it versatile for extended application in SNM searches. Therefore, the MLFDs were coupled to an array of SiPMs as an imager to locate the direction of a neutron source in a mixed radiation environment, and was successfully able to predict the location within 30 seconds in a 5cm radius. The imaging system can be configured to have all necessary electronics on-board, making it light-weight, portable and compact. The MLFD can be batch-fabricated with ease and in a simple four-step process using commonly-found laboratory equipment.

The micro-layered fast-neutron detector

by

Priyarshini Ghosh

B.E., Birla Institute of Technology, India, 2015

A DISSERTATION

submitted in partial fulfillment of the requirements for the degree

DOCTOR OF PHILOSOPHY

Alan Levin Department of Mechanical & Nuclear Engineering
Carl R. Ice College of Engineering

KANSAS STATE UNIVERSITY
Manhattan, Kansas

2021

Approved by:

Major Professor
Douglas S. McGregor

Copyright

Abstract

The Micro-Layered Fast-Neutron Detector (MLFD) is a novel fast-neutron detection technology that has been developed from concept stage to proven demonstrability in a laboratory environment. The MLFD boasts a high fast-neutron detection efficiency of 9.2% at 43 mm length-of-detector, a near-100% gamma-ray rejection capability without requiring pulse shape discrimination or any additional electronics or techniques, and suppression of Ĉerenkov radiation generation inherently by design. These features have been achieved by careful material selection in suitable geometrical fashion. Polymethyl methacrylate (PMMA) was used as a neutron converter (by proton recoil) and light guide, and zinc sulfide as an inorganic scintillator, in an alternating layer configuration such as to maximize scintillation photon collection from neutron interactions while minimizing Ĉerenkov generation. A photodetector attaches to the side of the MLFD, which can either be a photomultiplier tube (PMT) or a silicon photomultiplier (SiPM), depending on the application desired. The orientation of the photodetector on the side (parallel to the longest length of the MLFD) also reduces probability of forward-propagational Ĉerenkov photons from being collected. The detection efficiency can also be scaled by simply increasing the number of layers, i.e., the length of the detector. The vastly different decay pulse times for protons (700 ns to 10,000 ns) and electrons (12 ns) leads to a very distinct neutron and gamma-ray event separation, leading to a PSD ratio of 4.56. Furthermore, replacing the PMT with SiPMs reduces the Ĉerenkov radiation developed in the PMT photocathode window, thereby eliminating the need for pulse shape discrimination altogether, and only requires a low LLD to reject almost all gamma radiation.

Although originally designed for use at the TREAT facility of Idaho National Laboratory, the MLFD has exhibited performance that makes it versatile for extended application in SNM searches. The MLFDs were coupled to an array of SiPMs as an imager to locate the direction of a neutron source in a mixed radiation environment, and was successfully able to predict the location within 30 seconds in a 5cm radius. The imaging system can be configured to have all necessary electronics on-board, making it light-weight, portable and compact. The MLFD can be batch-fabricated with ease and in a simple four-step process using commonly-found laboratory equipment.

Table of Contents

List of Figures

List of Tables

Acknowledgement

The work presented in this dissertation was conceived and accomplished in the Semiconductor And Radiological Technologies Laboratory, Kansas State University. The work was also supported by collaborations with the Electronics Design Laboratory, Semiconductor Materials Analysis Laboratory, KSU TRIGA Mk II Research Reactor, Nanomaterial Characterization Laboratory, Geology Department, and Chemistry Department.

Although I claim this work to be mine, it would not have existed without unrelenting motivation from my father, Rajat Ghosh, and enduring strength from my mother, Anindita Ghosh. Much like the atom, their contribution cannot be "seen" but is omnipresent. My grandfather, Shona dadu, keeps watching over me. My Pishi always finds different ways of supporting me. Much assistance has also come from Shamik Sadhu, who has always been there, even from thousands of kilometers away.

The guidance I received throughout the course of the graduate program has been extraordinary in a myriad of ways—from Dr. Douglas McGregor, Dr. Jeremy Roberts, Dr. William Dunn, Dr. Hitesh Bindra, Dr. Brett DePaola and Dr. Christer Aakeröy. I thank them immensely for their time and efforts. I would also like to thank Dr. Apurba Kar, Dr. Kingshuk Bose, Dr. Mark Harrison, Dr. Catherine Riddle, Dr. Paul Barton, Dr. Ryan Fronk, Dr. Michael Reichenberger, Dr. Steven Bellinger, Dr. Ben Montag, Dr. Taylor Ochs, Dr. Smreeti Dahariya, Dr. Maria Pinilla, Dr. Diego Laramore, Dr. Wenkai Fu, Sarah Stevenson, Anisha Bhattacharya, Nicole Virgili, Dan Nichols, Sanchit Sharma, Robyn Hutchins, Jacob Terrell, Daniel Watson, Tim Sobering, Patrick Doyle, and many others for all their support.

Dedication

This dissertation is dedicated to my Ma and my Baba.

Chapter 1 - Introduction

1.1 Research Motivation

Nuclear energy is a clean, safe, reliable and competitive source of energy. It is the only source of energy that can replace a significant part of the fossil fuels (coal, oil and gas) which pollute the atmosphere massively and contribute to the greenhouse effect. Operating a nuclear reactor requires the continuous monitoring of safety. However, unexpected events can occur, such as a loss of coolant, or sudden reactor overpower. Therefore, it is important to determine the safety limits of operation and fuel failure thresholds. These parameters can be measured by monitoring the real-time behavior of fuel elements when abnormally stressed. As an example, instrumentation for monitoring fuel motion was constructed at the Transient Reactor Test (TREAT) facility at Idaho National Laboratory in 1963. The TREAT instrumentation provides stress testing of nuclear fuels during which quick, high energy neutron pulses are produced to simulate accident-like conditions [1]. Arrays of fast neutron detectors are placed in collimated slots to observe fuel motion during such transients. They provide time and spatial resolution of fuel displacements during reactor power transient experiments, as well as before and after the transient.

1.1.1 Challenges in Accident Tolerance Testing of Reactor Fuels

The 2011 Fukushima Daiichi disaster, which prompted the shutdown of Japan and Germany's nuclear power plants, sparked interest in resuming nuclear fuel testing at the TREAT facility at the Idaho National Laboratory (INL). In November 2017, the U.S. Department of Energy restarted transient testing for the development of advanced, safer, and more efficient fuels. The TREAT instrumentation includes the "hodoscope" for tracking fuel motion, which consists of 334 steel-collimated channels coupled to 'Hornyak button' neutron detectors for detecting fast-neutron pulses [2]. Stress-testing requires statistical precision of fast-neutron count rates, which increases with true-positive detector events. Hence maximizing fast-neutron detection efficiency, while also minimizing gamma-ray background from being misidentified as neutrons, becomes imperative. The Hornyak button, however, suffers from low detection efficiency, Ĉerenkov radiation contaminating the signal, and non-linearity of detector response at large transients. Thus, there has

been a need to improve the neutron detection system for increased precision in fuel motion imaging.

1.1.2 Challenges in Special Nuclear Materials Searches

Similar to fuel motion imaging, active interrogation requires discrimination of neutrons from gamma-rays. Presently, organic scintillators are generally used for fast neutron detection. Although pulse shape discrimination can be used to distinguish between fast neutron and gamma-ray events, in applications which have intense gamma-ray fields, the discrimination becomes less effective for organic scintillators due to neutron signal corruption at higher gamma-ray fluxes [3], thus limiting measurement of the neutron spectra. Furthermore, additional techniques and electronics to discriminate between particles can complicate the overall detector and add weight to portable systems.

1.1.3 Development of the Micro-Layered Fast Neutron Detector

To address these issues, there was a need for a simple detection system that is capable of providing accurate and reliable data. The Micro-Layered Fast-Neutron Detector (MLFD) was devised to address the shortcomings of both fuel imaging and active interrogation applications. The novelty of the MLFD lies in its geometry and material selection: it uses zinc sulfide as the scintillation medium, which has a relatively high light yield for protons but a low conversion efficiency for fast electrons, thereby providing an inherent preference for neutrons over gamma rays in a mixed radiation environment. However, the use of ZnS has been limited to thin-film devices only due its light self-absorption. The layer geometry of the MLFD overcomes this limitation and allows the incorporation of a large volume of scintillator without compromising on light transparency. The MLFD consists of alternating layers of a neutron converter material such as polymethyl methacrylate, and a scintillation material (ZnS). The neutron converter layer translates a portion of the neutron energy to a recoiled proton via the (n,p) scattering reaction, while the scintillation layer molecules emit radiation in the form of visible light when excited by a proton. A photodetector, such as a photomultiplier tube or silicon photomultiplier, is placed perpendicular along the layers instead of at the end, enabling maximized collection of scintillation light. For fuel imaging at TREAT, the direction of the neutrons is known, and the photodetector is

placed parallel to this direction, which lowers the probability of light collected from Ĉerenkov radiation generated in the neutron converter material. Remarkably, the MLFD was found to be highly insensitive to gamma rays, without requiring any discrimination techniques such as pulse shape discrimination, especially when coupled to silicon photomultipliers. This finding led to an expansion of its application in SNM searches. As will be discussed in detail in the following chapters, the MLFD was shown to also have a high fast-neutron detection efficiency that is tunable to the application by varying the number of layers in the MLFD.

1.2 Contributions to the Scintillator Community

The MLFD was initially designed with the intention of employing it to image nuclear fuel motion in reactor accident conditions. However, on displaying versatile qualities, the scintillator was explored further and has been developed to contribute to other fields, most notably in Special Nuclear Materials searches. This process of research has led to the following contributions to the scientific community and to technology, in order of impact:

a. Invention of a novel device that has inherent gamma-ray insensitivity while detecting fast neutrons without requiring any additional particle-discriminating equipment or techniques.
b. Silver-doped zinc sulfide, although a high light-yield scintillator, has not been used widely and mostly delegated to use as low-efficiency thin, single-layered detection medium owing to its opaqueness to its own light. With the MLFD, a unique geometrical design overcomes the opacity problem, and introduces a novel design to use ZnS as a large-volume scintillator.
c. A PSD ratio of 4.56 was achieved for fast-neutron and gamma-ray separation, which is the highest-known ratio reported for any scintillator, to the best of the author's knowledge.
d. The ZnS:Ag decay time and mode for protons were determined for the first time, and agrees with literature values for ZnS:Ag decay time and mode for alpha particles, which are also heavy, charged particles.
e. The fast-neutron detection efficiency of the MLFD is scalable with increasing layers, a feature that makes the device tunable to the application.

These technological achievements have been detailed in this dissertation, with the following section being a guide to the contents of the rest of the dissertation.

1.3 Dissertation Organization

Efforts into building a device capable of mitigating the shortcomings of currently available technology in fuel motion imaging and active interrogation have been presented in this dissertation, spanning six chapters. Provided in Chapter 2 are an introductory background of radiation detection physics, material science, and present technologies and their shortcomings that have prompted a need for the MLFD. Discussed in Chapter 3 are the detector designs for addressing challenges to present technology, which ultimately lead to the realization of the MLFD. Also included in the chapter are current methods of fabricating the MLFD, and summarizes previous trials in devising the MLFD and alternative designs. Following fabrication, shown in Chapter 4 is how the detector was instrumented with associated electronics to read data for performance analysis and testing. In Chapter 5, the characterization of the detector is discussed to understand its capabilities and limitations. Reviewed in Chapter 6 are the detector performance, and analyzes its results to evaluate its suitability for the proposed applications. Finally, concluded in Chapter 7 are implications of the results, summarizes the main findings, and provides guidance for future steps with the MLFD. This dissertation includes work that has been reported in five peer-reviewed journal publications and four conference proceedings, including one poster presentation. Additionally, this dissertation is supported with references to reliable work reported by independent, non-conflicting organizations to verify the contents of the present work. Figures that are referenced have been reproduced by extracting data from the original work given in the reference.

Chapter 2 - Background

The following sections in this chapter will provide the reader with adequate background regarding the physics and processes that form the basis of the Micro-Layered Fast-Neutron Detector. Topics of discussion include neutrons and gamma rays and their interaction with media, working principle of scintillators, associated electronics, and previous work done in related areas.

2.1 Radiation and its Interaction with Matter

Radiation is the emission or transversal of energy as waves or particles. Principally categorized into ionizing and non-ionizing radiation, the former stands of interest due to its ability to ionize atoms and molecules, and break chemical bonds. Ionizing radiation include charged particles such as alpha particles, beta particles and fission fragments, and neutral particles such as neutrons, gamma rays and x rays [4]. Neutrons are subatomic particles with a mass of 1.008 u (atomic mass unit), slightly larger than that of a proton (1.007 u). The neutron is stable inside the nucleus, but a free neutron is unstable, and beta-decays into a proton, electron, and an antineutrino with a half-life of about 15 minutes [5].

Table 2-1 Classification of neutrons according to energy [6].

Neutron energy	Energy range
0.0–0.025 eV	Cold neutrons
0.025 eV	Thermal neutrons
0.025–0.4 eV	Epithermal neutrons
0.4–0.5 eV	Cadmium neutrons
0.5–1 eV	EpiCadmium neutrons
1–10 eV	Slow neutrons
10–300 eV	Resonance neutrons
300 eV–1 MeV	Intermediate neutrons
1–20 MeV	Fast neutrons
> 20 MeV	Ultrafast neutrons

Based on the energy, neutrons can be classified into several types constituting an energy distribution that is adapted to the Maxwellian distribution for thermal motion. Listed in Table 2-1

are neutron types distinguished by their range of energies. This classification is important for selecting the detection mechanism, which is highly dependent on the neutron energy. Fast neutrons have energy between 1 and 20 MeV and can be produced from several sources. Nuclear fission produces neutrons that have a mean energy of 2 MeV, such as those generated at TREAT. Spontaneous fission sources, like ^{252}Cf, produce a similar Maxwell-Boltzmann distribution from 0 to about 10 MeV. Nuclear fusion is also another source; deuterium–tritium fusion produces neutrons with an energy of 14.1 MeV. Gamma radiation is naturally produced from neutron stars, supernova explosions and beyond the event horizon in black holes, and, less dramatically, from nuclear explosions and lightning.

Alpha particles, electrons and protons are charged particles, and therefore continuously lose energy via Coulombic interactions with electrons in the medium they pass through. Gamma rays and neutrons are both uncharged particles, and hence not affected by the Coulomb force when passing through matter. Gamma rays can interact with electrons directly, but neutrons generally only interact with an atomic nucleus, rendering their detection more complicated, such as via transferring their energy to charged particles or by neutron capture [7].

2.1.1 Spontaneous Fission

Unstable nuclei of heavy elements can split into two nuclei of lighter elements that are similar in mass, and liberate a large amount of energy. Lighter elements are unable to overcome the large potential barrier in distorting the nucleus from its original near-spherical shape, and hence do not undergo spontaneous fission.

Most commonly, ^{252}Cf is capable of spontaneously fissioning, with a 96.9% probability of undergoing alpha decay, and a 3.1% probability of spontaneous fission. It's half-life, if only spontaneous fission were considered the only decay process, would be 85.5 years. However, since its probability of alpha decay is much higher (and whose half-life is about 2.73 years), the effective half-life of ^{252}Cf is 2.64 years. Per fission, about 3.7 neutrons are emitted with an average energy of 2.3 MeV. The average alpha particle energy is 6.12 MeV. Prompt fission gamma rays are also emitted in the fission process. While the neutron emission rate from ^{252}Cf is about 2.4×10^{12} neutrons s^{-1} g^{-1}, the gamma-ray emission rate is 1.3×10^{13} γ s^{-1} g^{-1}. The neutron energy (*f(E)*) follows the Watt fission spectrum [8]:

$$f(E) \propto e^{-\frac{E}{1.025}} \sinh\left(\sqrt{2.926E}\right) \tag{2.1}$$

The prompt fission gamma-ray spectrum was given by:

$$N(E) = \begin{cases} 38.13(E - 0.085)e^{1.648E} & E < 0.3\ MeV \\ 26.8e^{-2.30E} & 0.3 < E < 1.0\ MeV \\ 8.0e^{-1.1E} & 1.0 < E < 8.0\ MeV \end{cases} \tag{2.2}$$

where *N(E)* is the number of gamma rays at energy *E*.

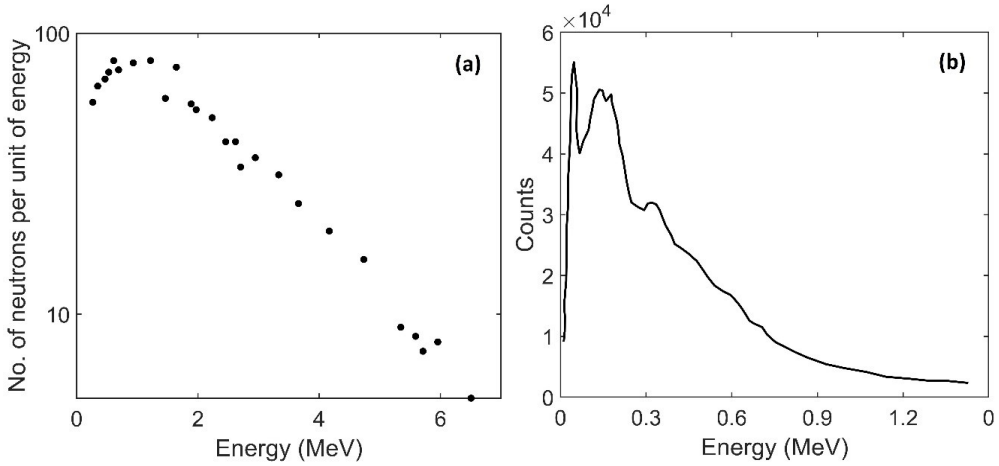

Figure 2-1. ^{252}Cf (a) neutron [9] and (b) gamma-ray spectra [10].

2.1.2 Fast-Neutron Detection

Neutrons, depending on their energy, can be detected by three primary methods: scattering, absorption and activation. The relative probabilities of these methods change drastically with neutron energy. Fast neutrons, having high energies, can transfer an appreciable amount of energy to the nuclei they are interacting with. Such an interaction is called elastic recoil scattering, or a (n,p) reaction, the 'n' denoting the neutron, while the 'p' denotes the secondary particles for such collisions—recoil protons. During each collision, the fast neutron loses energy, and is moderated, or slowed down, while the 'lost' energy is transferred to the proton. The process of scattering is desirable over other methods in detection of fast neutrons when information such as the original energy of the neutron, its direction of travel, and the time of emission is important to know.

2.1.3 Gamma-Ray Detection

Gamma rays can interact with matter in a variety of ways, three of which are significant for radiation measurements. The first, named photoelectric absorption, is the ejection of a photoelectron on absorbing the photon by the target atom. The original photon disappears completely. This interaction can only take place with the atom as a whole, not with free electrons. The photoelectric interaction is the dominant mode of interaction for gamma rays and x rays of low energy, and for target materials of high atomic number (Z). The second, Compton scattering, takes places between the gamma-ray photon and an electron. In this interaction, the incident photon is deflected through an angle θ, thereby transferring a portion of its energy to the electron at rest. All angles of scattering are possible, hence the energy transferred to the recoil electron can vary from zero to a large fraction of the original photon energy. The probability of Compton scattering depends on the density of electrons as available scattering targets, and thus increases with Z. Finally, if the gamma-ray energy exceeds twice the rest-mass energy of an electron (1.02 MeV), a third process, named pair production, is possible. This interaction takes place in the Coulomb field of a nucleus, and the gamma-ray photon disappears to produce an electron-positron pair. Figure 2-2 represents the probabilities of the three processes.

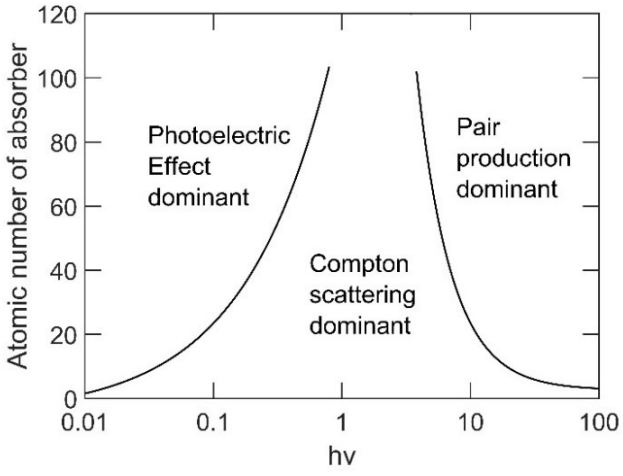

Figure 2-2 Interaction of gamma-rays of different energies with materials can take place by different processes [7].

2.1.4 Ĉerenkov Radiation

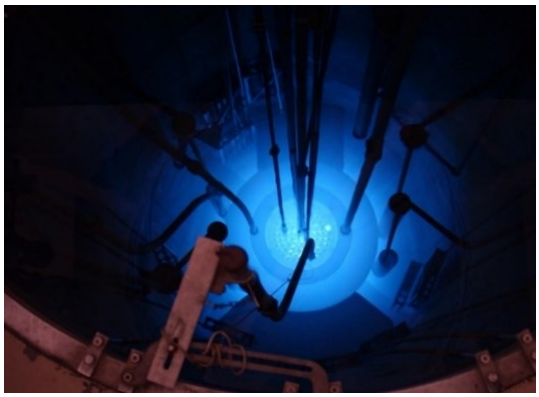

Figure 2-3. The blue glow in K-State's TRIGA Mk II reactor is due to Ĉerenkov radiation, reproduced from www.ksu.edu.

When a charged particle, such as an electron, passes through a dielectric material at a speed greater than the phase velocity of light in the medium, Ĉerenkov radiation is emitted. The threshold energies (E_e) for electrons travelling in different media is given by:

$$E_e = m_0c^2\sqrt{\frac{n^2}{n^2-1}} \tag{2.3}$$

where m_0c^2 is the rest mass equivalent, and n is the refractive index of the medium. Therefore, the minimum energy of gamma rays to produce recoil electrons that ultimately produce Ĉerenkov radiation is given by:

$$E_\gamma = \frac{T_e + \sqrt{T_e^2 + 2T_e m_0c^2}}{2} \tag{2.4}$$

$$T_e = m_0c^2\left[\sqrt{\frac{n^2}{n^2-1}} - 1\right] \tag{2.5}$$

where T_e is the kinetic energy required to produce Ĉerenkov radiation.

Ĉerenkov radiation arises from asymmetric polarization of the molecules of the material in front and at the rear of the particle, leading to a varying electric dipole momentum. The molecules promptly return to their stable state by the emission of photons. This phenomenon is analogous to its more popular sonic counterpart, i.e., the sonic boom.

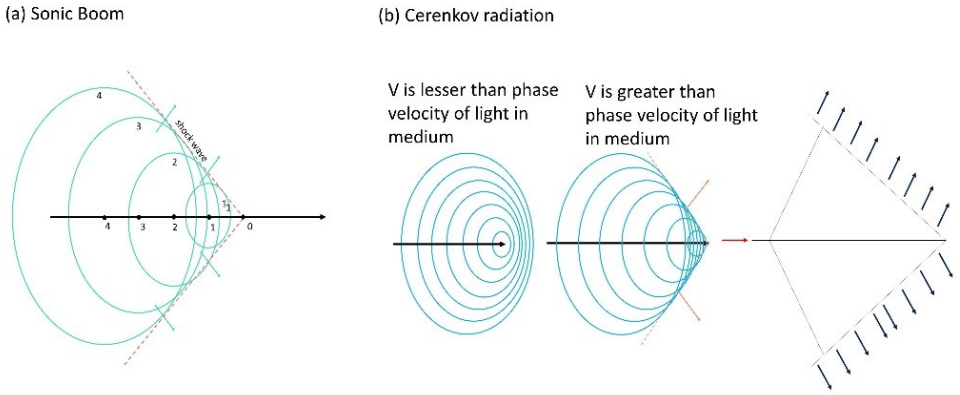

Figure 2-4. Mechanism of Ĉerenkov radiation generation is analogous to that of the sonic boom.

The shock wave in case of the electrically charged particles is in the form of photons, the frequency spectrum of which is continuous. The shorter wavelengths are more intense, hence Ĉerenkov radiation is observed to be a brilliant blue. Ĉerenkov detectors use the axis of the cone to determine particle direction, and the light yield determines the energy of the particle. However, Ĉerenkov radiation can be a nuisance if it is generated by background radiation, especially in an environment where the background 'particles' are significant in number, and this can lead to contamination of the final signal produces, misclassification and misidentification of particles, and ultimately lead to inaccurate detection results.

2.2 Principles of Scintillation Detection and Material Properties

The first type of radiation detector invented was a scintillating screen—barium platinocyanide—devised by Wilhelm C. Röntgen in 1895 while he discovered x rays [11]. The screen had become illuminated in a completely dark room on being irradiated with x rays. Thus the first radiation detector was produced, which was a material that emits light when excited by ionizing radiation. The light is produced by radiation interacting with either the atomic or molecular structure, which excites electrons to a higher energy state. To return to its ground state,

the electron releases energy in the form of photons. Ideally, for a material to be a worthy scintillator, it should possess the following properties:

1. It should be able to convert the energy of the ionizing radiation into detectable light with a high light yield.

2. The light emission must be spontaneous (fluorescence) rather than delayed light emission (phosphorescence).

3. It must be transparent to the wavelength of its own emitted light.

4. The emitted wavelength should be able to be efficiently detected by light-collection devices such as photomultiplier tubes (PMTs) and silicon photomultipliers (SiPMs).

The aforementioned properties help the user to determine the material of choice according to the end use, in addition to other qualities that may be required. Scintillation materials are classified into two main types based on the physical differences in their light production mechanism [4]: organic and inorganic. While organic compounds produce scintillation photons from molecular bonds and states, inorganic compounds require a periodic lattice for atomic states.

2.2.1 Inorganic Scintillators

Upon absorbing radiation, electron-hole pairs are generated. While holes in the valence band can move freely throughout the crystal, the electrons in the conduction band are excited from the valence band up to the conduction bands. The excited electrons quickly lose energy in the form of photons to de-excite to the lowest conduction band edge. However, if the inorganic crystal is doped with activator impurities, additional energy levels can be produced in the band gap (the forbidden region between valence and conduction bands). In this case, the excited electrons can drop to the lowest conduction band edge or the upper activator site energy state. Upon dropping to the activator ground state, light photons are released that have lower energy than the crystal band gap [4]. It is important to note that the process of fluorescence is almost instantaneous upon absorbing radiation, while delayed transitions from forbidden energy states result in phosphorescence, a phenomenon in which the re-emission of photons takes place well after the original ionizing event.

The emission spectrum, dictated by the band-gap energy of the scintillator and activator energy levels, is generally spread over a continuous range of energies due to vibrational states [4]. The excitation energy being different from the emission energy causes their respective spectra to be different; this property is called the Stokes shift.

Activation

In the inorganic crystal, only a small fraction of atoms—emission centers of luminescence centers—emit photons. These 'inhomogeneities' in the crystal lattice can be introduced by the addition of a small amount of dopants to 'activate' the crystal. The activator atom energy states within the band gap determine the wavelength of emission.

2.2.2 Nuclear Properties

Fast-neutron detection based on recoil scattering requires low-atomic mass (A) materials in order to transfer the maximum amount of energy. Hydrogenous materials are thus best suited to construct fast-neutron scintillators. Such hydrogenous materials can be used as the neutron converter in conjunction with other scintillating materials that produce light from recoil protons, or, the hydrogenous material itself can be scintillation, in the form of an organic scintillator. However, organic scintillators generally have lower light yield than inorganic scintillators. To select the best material for fast-neutron detection, a quantitative parameter called the neutron cross section is utilized. The neutron cross-section value determines the probability of interaction per unit path length. The elastic scattering cross-section for various elements are shown in Figure 2-5. The energy transferred to the recoil proton can also be determined using the following equation:

$$\frac{T}{E} = \frac{4A}{(1+A)^2}\omega^2 \tag{2.6}$$

where T is the energy transferred to the proton, E is the neutron energy, A is the mass number of the material, and ω is the cosine of the scattering angle of the recoil neutron. The neutron energy at maximum energy transfer to the proton would equal zero.

Using equation (2.6), Hydrogen (A=1), having similar mass as that of a neutron, would allow 100% transfer of neutron energy, and is thus the most efficient neutron converter. Once the neutron energy has transferred onto protons (positively charged particles), they can be detected by Coulombic interactions with electrons. The charged particle slows down gradually through further interactions via scattering reactions.

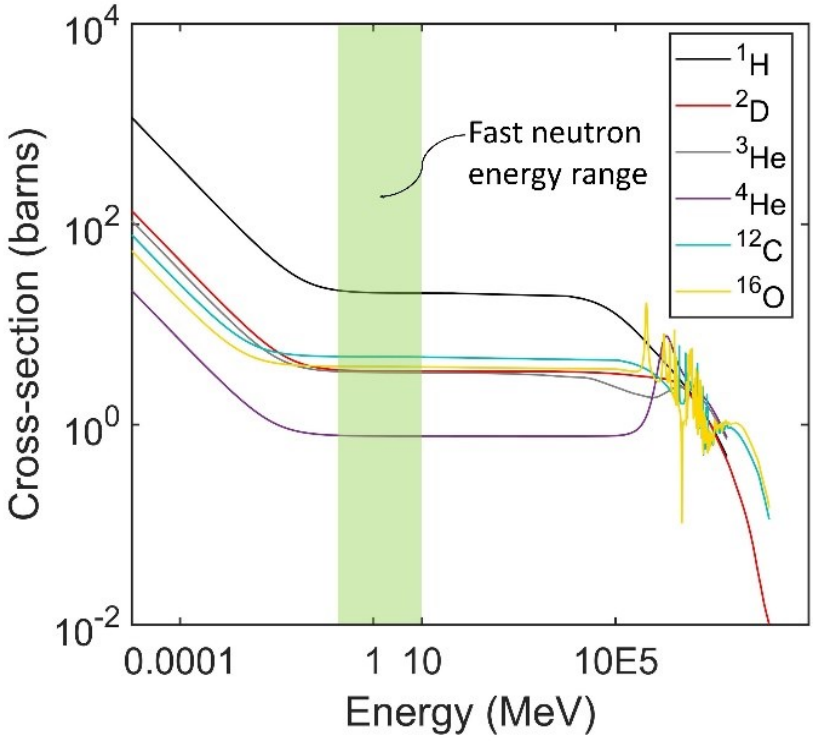

Figure 2-5. (n,p) scattering cross-sections for various elements [12].

Various plastics with high hydrogen content are not scintillators, thus require adjacent additional organic or inorganic scintillating materials. The secondary particles obtained from neutron scattering, such as protons, interact with the inorganic crystal molecules to produce scintillation photons. The choices of scintillation and recoil proton-generating materials are crucial for optimum detector performance.

Neutron converter material

Material properties such as hydrogen concentration, radiation hardness, and optical transparency are important considerations while selecting a neutron converter material.

Hydrogen Concentration

Organic materials, i.e., plastics have a high concentration of hydrogen, and hence are commonly used in scintillators for fast-neutron detection. Plastics also contain carbon, and occasionally other elements such as oxygen and sulfur. While a 100% transfer of energy is possible in hydrogen, the maximum amount of energy that can be transferred in carbon, according to equation (2.6), is about 28%, and reduces lower for oxygen, etc. The quantity 'hydrogen/carbon ratio', which is the ratio of the number of hydrogen to carbon atoms per molecule, provides a metric for compounds with higher hydrogen concentration. As the ratio of hydrogen to carbon atoms increases for a given molecule the energy deposited per scatter will also increase.

Radiation Hardness

Radiation hardness describes the extent to which materials are resistant to physical, structural and functional damages by radiation, particularly from neutrons and gamma rays. Fast neutrons can alter the atomic arrangement and crystalline structure. In plastics, aromatic rings and a high crosslink density is preferred because long aliphatic chains and low crosslink density can become easily rigid and brittle upon neutron and gamma-ray irradiation. The predominant radiation-induced effect is cross-linking of chains in organic compounds. Bonds can be easily broken and rearranged. Plastics containing chlorine initially blister and soften and fill with HCl, and thereafter harden due to cross-linking. Changes in chemical properties like polymerization and de-polymerization, oxidative degeneration and gas evolution can lead to changes in physical properties such as viscosity, solubility, conductivity, hardness and tensile strength. Teflon, polymethyl methacrylate (PMMA), and butyl rubber are most susceptible to becoming softer and weaker [13]. Irradiation of inorganic compounds can result in traps, color centers and defects (F-, V- and U- centers), however the effect of radiation on inorganic materials are far less significant than on organic materials. Oxide-based scintillators such as LYSO:Ce are highly resistant to gamma-ray radiation damage. Lu-based crystals have shown phosphorescence and radio-luminescence from proton irradiation [14]. The visible luminescence of zinc sulfide (ZnS) is insensitive to electron damage [15].

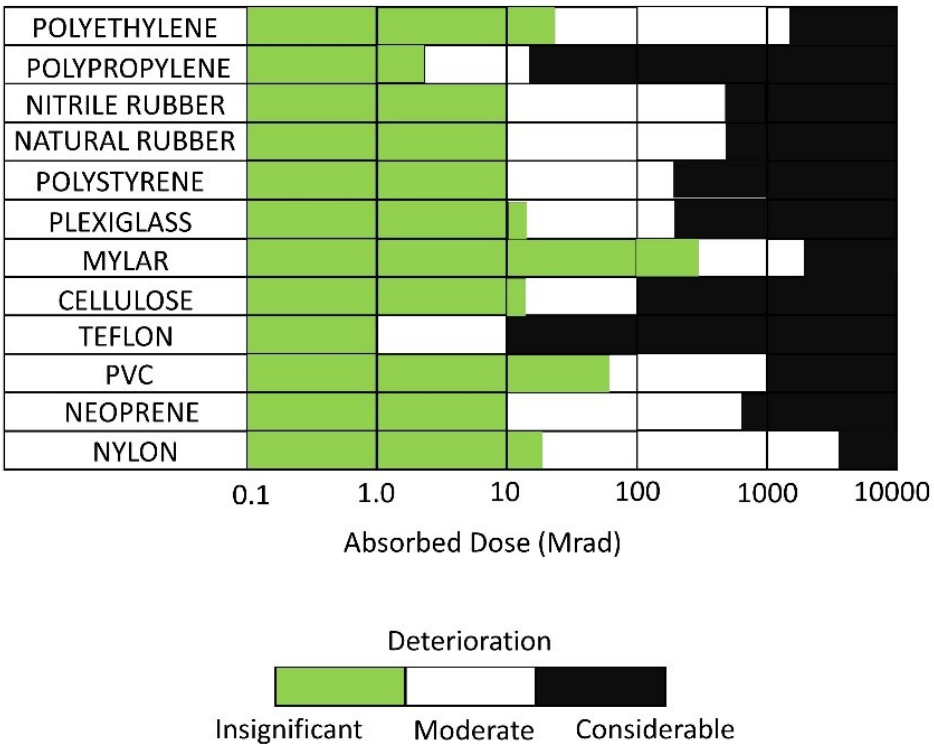

Figure 2-6. Effect of radiation damage for various polymers [13].

Optical transmission in Scintillation Medium

The detector crystal should be transparent to the emission wavelength in order for the photons to reach the light-collection device. If the crystal is opaque, however, such as ZnS, then their usage is generally delegated to thin-film detectors with low efficiency.

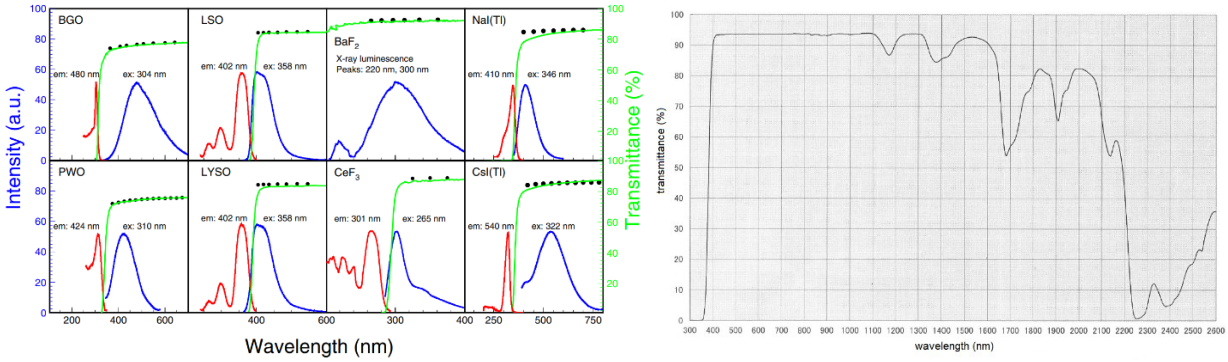

Figure 2-7. Optical transmittance as a function of wavelength for heavy crystal scintillators (left), and for light guides such as PMMA (right), reproduced with permission from IEEE and Astra Products [16].

Scintillation Material

Light Yield

The light yield is the number of scintillation photons produced per energy unit absorbed in the crystal. It is desirable for a scintillator to have a high light yield in order to achieve better resolution [4]. Generally, inorganic scintillators have higher light yields than their organic counterparts. The crystal lattice type and grain size can play an important role in the light yield of a scintillator. For example, larger crystal sizes of ZnS causes light trapping and internal reflection, leading to greater absorption of light. Grinding the powder to smaller sizes also reduces lattice vacancies, which function as traps [32]. Often, the light yield is non-linear for increasing energy deposition in the scintillator, and substantially differing in yield for different particles, resulting in difficulty in energy calibration. However, for detectors that are operated merely as counters, and not as spectrometers, non-linearity is not a limiting factor in selecting a scintillator as compared to the other factors discussed in this section.

Response to Light-Collection Device

The emission spectrum of the scintillator should be well-matched to that of the light-collection device. Oftentimes, if there is a mismatch, wavelength shifters are added to the crystal, that absorb photons of a shorter wavelength, and emit longer wavelength photons for matching.

Table 2-2. Light yields of various [a]inorganic materials and [b]organic materials [4].

Material Sub-Category	Example	Light Yield	Bi-alkali PMT response
Alkali Metal Halide[a]	NaI:Tl	43,000	1
Alkali earth Halide[a]	CaF_2:Eu	24,000	0.5
Transition Metal[a]	ZnS:Ag	50,000	1.3
Post-Transition Metal[a]	$Bi_4Ge_3O_{12}$ (BGO)	8,200	0.13
Lanthanide[a]	$CeBr_3$	68,000	1.65
Ceramic[a]	Li glass: Ce	4,650	0.12
Organic Crystalline[b]	Anthracene	17,200	-
Organic Liquid[b]	Eljen 305	13,760	-

2.2.3 Photodetectors

Radiation detection technology has greatly improved since the time that Hans Geiger painstakingly counted flashes of light under a microscope. Geiger measured alpha particle interactions in zinc sulfide (ZnS) [70]. Today, detecting photons has been made much less arduous by photomultiplier tube (PMT), which are electron vacuum tubes that produce secondary electron emission, and by silicon photomultipliers (SiPM), which are based on the excitation of conduction electrons in a semiconductor.

Photomultiplier Tubes

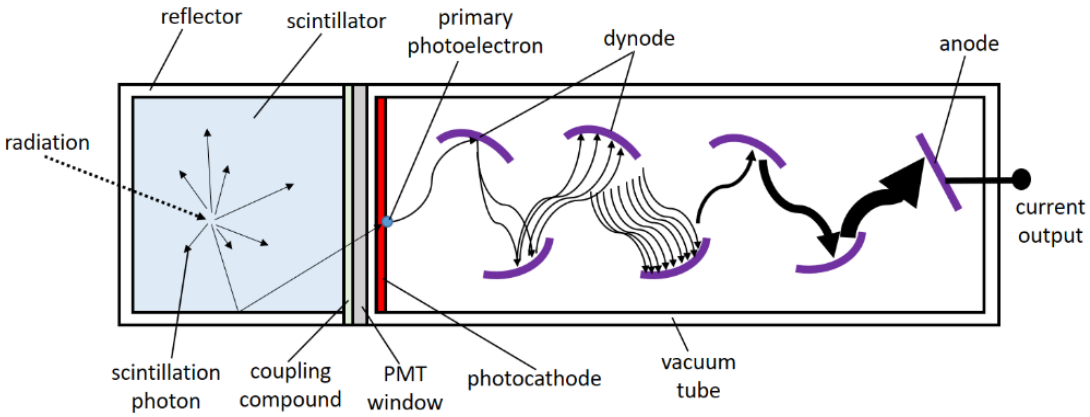

Figure 2-8. Design of and mechanism of radiation detection in a PMT [4].

The PMT is generally coupled to a scintillator crystal using a coupling compound. The photocathode window serves to absorb photons from the scintillating material. The coating on the window, on encountering photons, emit electrons by the photoelectric effect. Some of these electrons can diffuse through the coating and enter the vacuum tube. If a voltage is applied to the PMT, the electric field can impart speed to and guide the electrons to an adjacent electrode called a dynode. Hence, the electrons striking the dynode can lead to more electrons being liberated, which in turn are sped and guided by the electric field to the next dynode, liberating even more electrons. This process continues for a given number of dynodes. The PMT can thus turn photons into a large electronic signal, whose charge (Q) can be measured as:

$$Q = eqN_0G^M \tag{2.7}$$

where q is the charge of an electron, N_0 is the initial number of photoelectrons released at the photocathode, G is the number of electrons release by a dynode per incident electron (gain), and M is the total number of dynodes. The electrical signal produced is usually converted into a voltage pulse. An important feature of the PMT photocathode is its quantum efficiency (QE), defined as the number of electrons released from the photocathode per photon incident on it for a particular photon wavelength.

To reduce light losses from internal reflection at the scintillator/PMT interface, a coupling compound is usually inserted between the scintillator and PMT window, whose index of refraction closely matches that of the PMT window. Optical glue is the most common candidate, due to its ease of use. The PMT's sensitivity must match the emission spectrum of the scintillator. Dark noise in a PMT can originate from leakage current on the PMT surface (under low voltage conditions), thermionic emission of electrons (at common operating voltages), and regenerative effects (at high voltages). Background radiation as well as prolonged exposure to ambient light while under bias can also contribute to dark current. It is desirable to minimize dark current. PMTs are favorable because of their high gain and low dark current. The photocathode window is generally made of borosilicate glass or fused silica. Radiation interacting with the glass enclosure of PMTs can produce Ĉerenkov photons that can add to the signal produced from radiation interacting within the detector.

Semiconductor Photodetectors

Photodiodes are formed by a silicon p-n junction that creates a depletion region free of mobile charge carriers. Upon absorbing a photon, an electron-hole pair is generated in the silicon. If a reverse bias is applied to the photodiode, the electric field across the depletion region accelerates the holes towards the cathode and the electrons towards the anode, resulting in a net flow of current. If an adequately high electric field is generated in the depletion region, impact ionization occurs, i.e., the charge carriers can be accelerated to create secondary charge pairs. A single absorbed photon can lead to a continuous ionization cascade throughout the volume of the photodiode, causing the silicon to break down and become conductive, in a process called the

Geiger discharge. A large gain can be produced by operating a photodiode in the Geiger mode, and devices employing this method are known as Single Photon Avalanche Diodes (SPADs). To quench the current flow, a series resistor can be used to lower the reverse voltage in the diode to below its breakdown voltage, stopping the avalanche. Thereafter, the diode recharges to the bias voltage, and is once again available to detect more photons. This poses a problem: if more than one photon is absorbed in the diode at the same time, it will generate a signal as if only one photon produced it.

To overcome this loss of information, a dense array of tiny, independent SPADs each with a series resistor (referred to as a microcell) are combined into a silicon photomultiplier (SiPM). The Geiger avalanche is confined to the particular microcell it was generated in; during this process, all other microcells operate independently and are fully charged to detect photons. Each microcell is optically and electrically isolated from one another, leading to a region of dead space surrounding each microcell. Larger microcells lead to a higher active area and gain. The charge generated from an event can be expressed by:

$$Q = N_{fired} G e \tag{2.8}$$

where N_{fired} is the number of 'fired', or triggered microcells, and G is the gain as given by:

$$G = \frac{C \cdot \Delta V}{e} \tag{2.9}$$

where C is the microcell capacitance, ΔV is the overvoltage. SiPMs are generally operated at a bias that is 10-25% above its breakdown voltage. The difference between the operational bias and the breakdown voltage is its overvoltage.

Dark current in SiPMs can originate from overvoltage, temperature and active area. An added problem in SiPMs that can lead to noise is optical crosstalk between microcells, caused by accelerated charge carriers in high fields emitting photons that can trigger a secondary avalanche in a nearby microcell. Therefore, a single photon may generate signals equivalent to 2, 3 or more photons.

SiPMs have several advantage over PMTs: unlike bulky PMTs, SiPMs are small and compact. PMTs require high voltages of operation (~800V) while SiPMs require very low bias voltage (~30V). SiPMs can also achieve very high gains as compared to PMTs. SiPMs are capable of detection at the single photon level, which is typically not achieved using PMTs. SiPMs are also not affected by magnetic fields as are PMTs. Using an array of multiple SiPMs, however, can lead to excessive noise.

2.2.4 Photon Optics

Scintillation Light Reflector

It is common practice to encapsulate the scintillator crystal in a reflector in order to increase the probability of scintillation photons to reach the light collector. Reflectors are broadly classified into two types: specular and diffuse (or Lambertian). A specular reflector reflects the incident ray at the same angle to the surface normal as the incident ray, but on the opposite side of the surface normal. A mirror is an example of a specular reflector. An ideal diffuse reflector is one whose luminance is isotropic, i.e., a ray striking the Lambertian surface will reflect in such a manner that its apparent brightness remains the same regardless his angle of view. The luminous intensity of a Lambertian reflector follows Lambert's cosine law, given by:

$$I_\theta = I_0 cos\theta \ W\ cm^{-2} sr^{-1} \tag{2.10}$$

where I_θ is the intensity of the emitted light about an angle θ between the incident ray and the direction of interest, and I_0 is the intensity of the incident light. The choice of reflector type is dependent upon which one results in the least variance in light collection.

Light Guides

There are some cases in which regardless of whether the crystal is opaque or transparent, light guides like optical fibers connect the crystal to the light-collection device. This happens when the shape of the crystal is not well-suited to the light-collection device, or if the environment dictates that the light-collection device be at a different location than the crystal. Photodetectors

can suffer radiation damage, hence in high-radiation flux environments they might be required to be placed outside the radiation field, thus requiring a light guide to accept the photons from the crystal. Using external light guides obviously attenuates the beam intensity, and can also generate undesirable Ĉerenkov radiation.

Light Collection Efficiency

The ratio of the number of photons accepted at the photocathode to the total number of photons emitted by the light source is the light collection efficiency (LCE) of the detection system. The LCE depends on the geometry of the crystal, the nature of the reflector, how well the crystal is coupled to the PMT, and on the optical transparency of the crystal. If a crystal is coupled to a PMT, and the charge collected at the anode (Q) is known, then the LCE can be calculated:

$$Q = m \cdot LCE \cdot QE \cdot n \cdot R^n \cdot e \tag{2.11}$$

where m is the number of light photons produced in the crystal, n is the number of dynodes in the PMT, R is the dynode multiplication factor (R^n is the gain), and e is the electronic charge [17].

2.2.5 Pulse characteristics

A radiation particle interacts in the scintillating material to excite electron-hole pairs, of which a fraction of electrons falls into luminescent centers. Thereafter, the electron decays to release a photon. Scintillation pulses can be characterized by two time components: the fast (prompt) and slow (delayed) decay component, as given by:

$$N(t) = w_1\left(e^{-\frac{t}{t_{1f}}} - e^{-\frac{t}{t_{1r}}}\right) + w_2\left(e^{-\frac{t}{t_{2f}}} - e^{-\frac{t}{t_{2r}}}\right) \tag{2.12}$$

where $N(t)$ is the time-dependent pulse, w_1 and w_2 are the proportional light yield contributions of the fast and slow components, respectively, and t_1 and t_2 are the fast and slow decay times, respectively. The subscripts r and f denote rise and fall times of the pulse. Generally, the rise times are extremely short (< few ns), hence equation (2.12) reduces to:

$$N(t) = w_1 e^{-\frac{t}{t_{1f}}} + w_2 e^{-\frac{t}{t_{2f}}} \tag{2.13}$$

Table 2-3. Rise and decay times of some inorganic scintillators [18].

Composition	Decay times				Rise times
	t_{1f} (ns)	w_1(%)	t_{2f} (ns)	w_2 (%)	t_r (ps)
GAGG:Ce	317	9	89	91	497
GAGG:Ce:Mg	188	34	60	66	72
LuAG:Ce	1784	66	97	34	923
LuAG:Ce:Mg	667	13	49	87	230
YAG:Ce	445	51	97	49	1560
YAG:Ce:Mg	134	33	51	67	137
LuAG:Pr	924	50	22	50	254

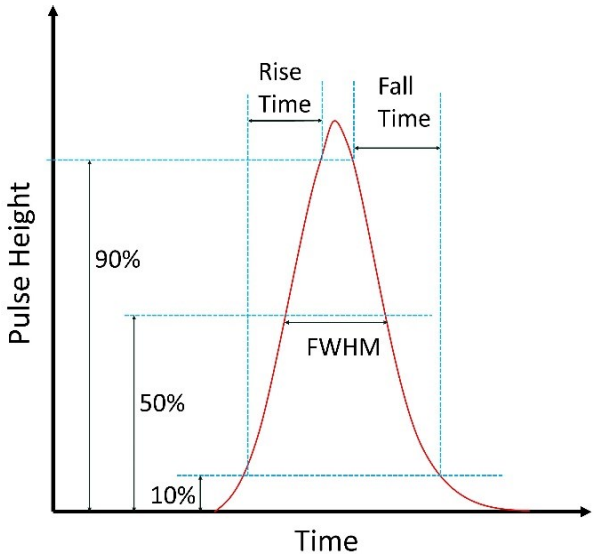

Figure 2-9. Output pulse response from a PMT [4].

In a PMT, there is a 'transit time' between a delta-function light pulse striking the photocathode and the peak amplitude of the output current. The transit time includes the time for electrons to diffuse from the photocathode to the vacuum interface, to reach the first dynode, and to traverse the multiple dynodes. The 'rise time' in a PMT is the time taken by the output pulse to increase from 10% maximum to 90% maximum. This includes the charge collection time

measured between the last dynode and the anode. Similarly, the 'fall time' in a PMT is the time taken by the trailing edge of the output pulse to fall from 90% maximum to 10% maximum. When working with relatively slow inorganic scintillators such as NaI:Tl, the time response of the PMT is negligible compared to the decay time of the scintillator. However, if the crystal has fast decay times, the PMT can cause gain distortions and nonlinear behavior.

2.2.6 NIM Electronics and Spectroscopy

A detector can produce a pulse from a radiation particle interacting in it. A need arose in the 1960's for modular electronic standardization because of the lack of connection between detector electronics and data-obtaining systems. The Nuclear Instrument Module (NIM) was developed to guide the design of instruments that measure radiation and are interchangeable physically and electrically for the study of nuclear physics and engineering. NIM helps connect the electronic modules (amplifiers, Single Channel Analyzers, etc.) to the frame of a NIM bin via connectors and cables. Table 2-4 contains a list of NIM equipment that was used in this project.

Table 2-4. NIM equipment and their functions.

Equipment	Function
High-Voltage Power Supply (HVPS)	Provides a positive or negative voltage for operating the detector
DC power supply	Delivers a constant DC voltage to its load
Preamplifier	Provides an optimized coupling between the detector output and the counting system following the preamplifier, minimize noise, signal shaping, impedance matching to reduce attenuation of signal
Amplifier	Amplifies signal
Oscilloscope	Displays and records voltage pulses
Counter/Timer	Counts pulses, and sets time durations for counting pulses
Multichannel Analyzer (MCA)	Records and stores pulses according to their height, displays a histogram of pulse heights

Digitizer	Receives analog information, and records it digitally; used to study timing characteristics of a pulse

Pulse Height Spectrum

Spectroscopy is the science of quantifying radionuclides by analyzing a histogram of energies produced by a detector. Each pulse emerging from a radiation interaction in the detector is binned according to its pulse height, forming the histogram. This pulse height spectrum (PHS) can vary in its features depending not only on the amount of energy deposited, but on the geometry of the detector, effect of multiple scattering, and various other factors. For example, a proton-recoil scintillator (containing only hydrogen and carbon) irradiated by monoenergetic neutrons should produce, ideally, a step-function pulse height spectrum. However, statistical fluctuations arising from fluctuations in the number of excited free electrons, fraction of charges that decay by fluorescence, and final number of photons reaching the light collecting device results in a Gaussian softening of the high energy edge of the step function. Carbon scattering and multiple proton scattering can also distort the spectrum. If the detector geometry has dimensions smaller than the range of protons in it, the entire energy of the proton may not deposit in the detector, once again altering the spectrum. At high neutron energies, threshold reactions such as $^{12}C(n,\alpha)^{9}Be$ can occur, releasing energetic heavy ions that falsely add to the total neutron detection efficiency and further distorting the spectrum [4]. It is important to be aware of such effects in the analysis of the pulse height spectrum for the accurate inference of radionuclide identification.

2.2.7 Pulse-Shape Discrimination

If the detector is irradiated with more than one nuclide, or if threshold reactions within the detector cause false counts from secondary particles, the PHS can be contaminated with counts originating from different radionuclides. It is necessary to determine which count or pulse originated from which source in order to accurately measure the detection efficiency, or to identify the source of irradiation.

Pulse Height Discrimination

The lower channels in a PHS are usually dominated by counts from background radiation and electronic noise from the detector. A Lower Level Discriminator (LLD) is usually set at the lower channels to reject any pulses below the LLD. This method of removing potential background noise from the PHS by using an LLD is called pulse height discrimination. The principle of this method is based on the premise that "noise" only contributes to small pulses, therefore this method is a form of discrimination by pulse heights, or energy. Although setting an LLD helps eliminate background noise, it unwittingly also eliminates 'real' events, i.e., radiation interactions of interest but which deposited only a small amount of energy comparable to background noise. Consequently, the efficiency is reduced. Furthermore, interactions from different particles or threshold reactions can lead to high energy deposition, thus rendering pulse height discrimination ineffective in discriminating between those events.

Pulse Shape Discrimination

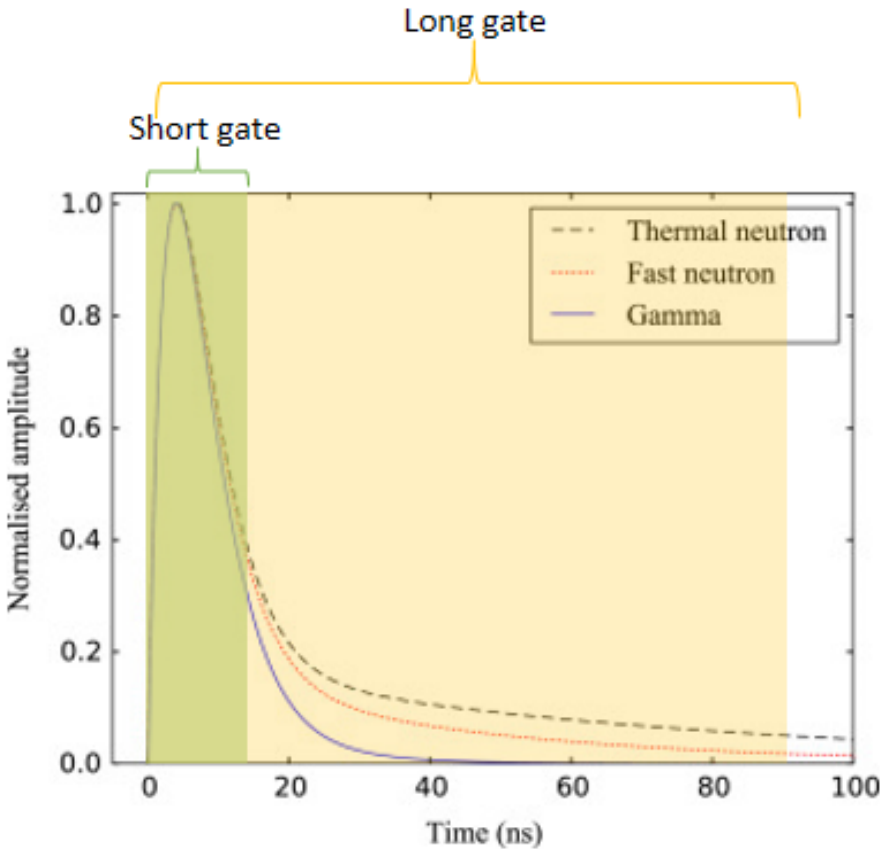

Figure 2-10. Decay times of events from a fast neutron, thermal neutron and a gamma ray interacting in a ^{6}Li-loaded plastic scintillator [19].

When events of similar energy, but different source of origin, need to be separated, the pulse shape is analyzed instead of the pulse height. The decay times of pulses produced in a scintillator from heavy ions and gamma rays are generally different, even if their pulse height is the same (Figure 2-10). Gamma-ray events have a prompt decay time, while neutrons generally have a delayed decay time in scintillators.

Charge integration method is a common technique for pulse shape discrimination (PSD) analysis, due to the method's simplicity and the straightforward hardware required. The relative amounts of charge from the prompt and delayed fluorescence is used to determine a PSD ratio, which separates neutrons from gamma rays. For each event, the current pulse is integrated over two time intervals, and a PSD ratio is determined. The amount of scintillation light reaching the PMT is computed as charge under the current pulse, the total being proportional to the amount of energy deposited in the detector. The ratio takes advantage of the larger amount of delayed light emission (slow component) from a recoil proton than that of the recoil electron. The difference in values of the PSD ratio, given by equation (2.14), separates the neutron and gamma-ray events,

$$PSD\ Ratio = \frac{Tail\ of\ signal}{Full\ signal} = \frac{Q_{Long\ Gate} - Q_{Short\ Gate}}{Q_{Long\ Gate}} \tag{2.14}$$

where $Q_{\text{Short Gate}}$ is the charge integrated during the short gate time period, generally representing the fast component of the light output, and $Q_{\text{Long Gate}}$ is the charge integrated during the long gate time period (Figure 2-10), representing the total scintillation light output.

Performance Metric

Fast neutron detectors are often required in situations where a significant background of gamma radiation exists. The ability of the detector-PSD system to clearly separate the particles determines its usefulness in that situation. To provide a quantitative determinant of the detection system's capacity to separate particles, as well as to compare different types of detectors to assess their applicability, a standard Figure-of-Merit (FoM) is calculated. The FoM is also used to optimize the values for short and long gates to select the most appropriate combination. The FoM is a post-process calculation,

$$FoM = \frac{S}{\delta_{gamma} + \delta_{neutron}} \tag{2.15}$$

where S is the distance between the centroids of the gamma-ray and neutron peaks, and δ is the full-width-at-half-maximum (FWHM) of the gamma-ray and neutron peaks.

The statistics used to model the charge integration method are based on the Poisson distribution, which can be conveniently reduced to a Gaussian distribution. For a Gaussian distribution, the FWHM is:

$$\delta = 2\sqrt{2ln2}\sigma \tag{2.16}$$

where σ is the standard deviation. From equation (2.15), the higher the FoM, better the discrimination between different particles. To set a benchmark for acceptable PSD, a reasonable definition for well-separated distribution dictates that the FoM should be above 1.27 [20].

Other methods of PSD include (1) the pulse gradient analysis; which compares the peak amplitude and sample amplitude at a later time, (2) the zero-crossing method; which uses time between the start of the pulse and the zero-crossing point in the filtered bipolar signal, and (3) the discrete wavelet transform, utilizing frequency domain features of the pulse. The charge integration technique is most commonly used due to its simplicity and highly accurate discrimination between neutrons and gamma-rays at high energies.

2.2.8 Mathematical Tools for Detector Characterization

To characterize a detector, one would need quantifiable values to assess its performance. As discussed earlier, a counter/timer records the number of events recorded by a detector within a specified time frame.

$$g = \frac{G}{t} = gross\ count\ rate \tag{2.17}$$

$$b = \frac{B}{t} = background\ count\ rate \tag{2.18}$$

$$net\ count\ rate = g - b \tag{2.19}$$

where G = number of counts recorded by the counter in time t with the source and detector present, and B = number of counts recorded by the counter in time t without the source, including counts from background radiation as well as electronic noise.

It is imperative to calculate the errors in count rates to determine if the data reported can be certified trustworthy. Given the same amount of measurement time for G and B, the net count rate error is given by:

$$\sigma_n = \frac{\sqrt{G + B}}{t} \tag{2.20}$$

The detection efficiency is used to assess the ability of the detector to detect a certain type of radiation. There are two categories of detection efficiency that can be determined, i.e., the absolute and intrinsic efficiency. The absolute efficiency is defined by:

$$\varepsilon_a = {}^{N}/_{N_s} \tag{2.21}$$

where ε_a is absolute efficiency, *N* is the number of neutron counts recorded by the detector, and *Ns* is the number of neutrons emitted by the source.

However, ε_a depends on the geometry and orientation of the detector and source, and would thus be difficult to compare efficiencies of detectors with different geometries and different orientations to the source. The geometry of the source and the detector affects measurements because the medium between the source and the detector may scatter and absorb particles, and,

more significantly, the shape of the detector and the distance between them would determine what fraction of the particles would be able to enter the detector. Therefore, a second quantity, intrinsic efficiency, is defined as:

$$\varepsilon_i = {}^{N}/_{N_D} \tag{2.22}$$

where ε_i is the intrinsic efficiency, N is the same as used in calculating absolute efficiency, and N_D is the number of neutrons incident on the detector.

The use of ε_i works to reduce the dependence of geometry and orientation by defining N_D as:

$$N_d = N_s * \Omega \tag{2.23}$$

where Ω is the solid angle subtended by the detector to the source of radiation, defined by:

$$\Omega = \frac{\begin{array}{c}Number\ of\ particles\ per\ second\ emitted\ inside\ the \\ space\ defined\ by\ the\ contours\ of\ the \\ source\ and\ the\ detector\ aperture\end{array}}{Number\ of\ particles\ per\ second\ emitted\ by\ the\ source} \tag{2.24}$$

$$\Omega = \frac{\int_{A_s}\int_{A_d}\left(\frac{S_0 dA_s}{4\pi r^2}\right) dA_d(\hat{n}\cdot\frac{\hat{r}}{r})}{S_0 A_s} \tag{2.25}$$

Thus, the intrinsic efficiency provides a uniform basis of comparison of different detector performances.

2.3 Applications

The need to detect fast neutrons can arise in various fields such as reactor instrumentation, space physics, fundamental particle searches, material science, special nuclear material searches and active interrogation techniques, to name a few. The material selection, type of detector required depends heavily on the application. Discussed below are few applications where fast neutron detectors play a key role.

2.3.1 Fuel Motion Imaging

Idaho National Laboratory recently restarted the Transient REActor Test (TREAT) facility for the development of safer and more efficient reactor fuels. To help regulators determine fuel-failure thresholds, effects of high-power excursions, criticality accidents (Chernobyl) and consequences of loss-of-coolant accidents (Fukushima Daichii) [21], the TREAT instrumentation provides stress-testing of nuclear fuels during which quick, high-energy neutron pulses are generated that induce fuel motion to simulate mild to severe accident conditions [1]. The behavior of the fuel with cladding and reactor core when abnormally stressed is of interest to developers of accident-tolerant fuels.

Measurement of fuel displacement during a transient can be conducted using standard instrumentation such as monitors for pressure, temperature, and coolant flow. Transparent coolants (gas and water) also allowed for optically photographing test capsules through a window [22]. However, with the advent of the liquid metal fast breeder reactor, test capsules became opaque. Thus, the opacity of the test capsule, and the limitations of the standard instrumentation led to the choice of using a fission particle detection system.

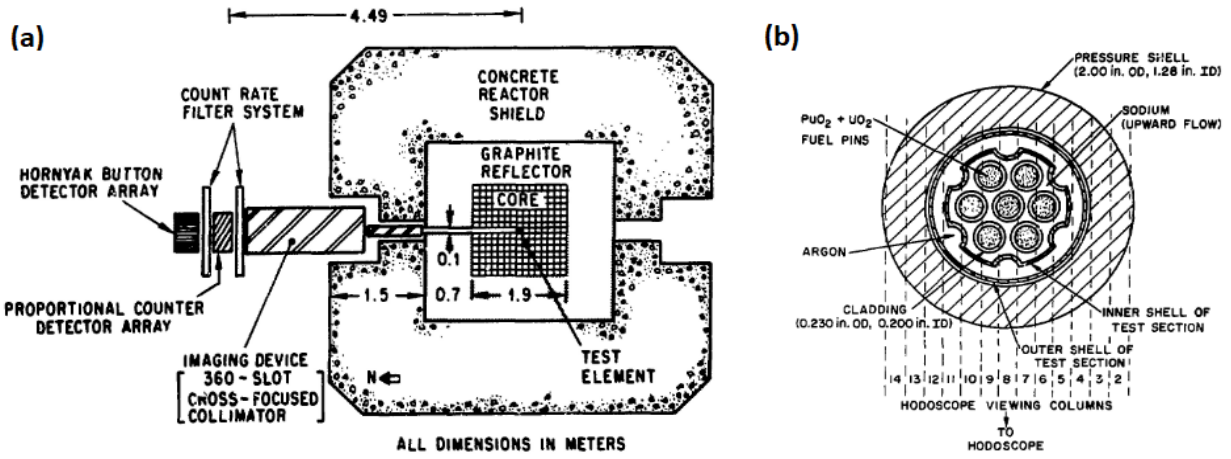

Figure 2-11. (a) Schematic arrangement of the hodoscope and test assembly at TREAT, (b) cross-section of test container showing "viewing slots" of the hodoscope, reproduced with permission from OSTI [22].

Fuel Displacement Imaging

The reactor neutrons induce fission in the fuel, producing fission neutrons, gamma rays in the test fuel, and other forms of lesser penetrating radiation, such as alpha and beta particles. Only penetrating radiation, such as gamma rays and neutrons, is detectable given the extensive quantity of material surrounding the test fuel. However, the gamma-ray emission times are longer than the transients, hence they would not provide useful information about fuel motion during the transient. Furthermore, gamma-rays also constitute a significant portion of the background from capture radiation in the test assembly, overwhelming the response from the fuel. Therefore, the detection of fast neutrons become the preferred method of imaging the fuel displacement during a transient. The presence of a collimator aids in line-of-sight viewing of the test fuel pins, the "pixel" of an image being dependent on the collimator aperture, which is 0.25 mm × 8 mm at TREAT [2]. The reactor fuel used is ^{235}U, and each thermal fission produces about 2.4 neutrons. 70% of these neutrons are above 1 MeV. Although it is desirable to select fission neutrons directed from a segment of fissile material, any fast neutron above 0.1 MeV is indistinguishable from a fission neutron. Fast neutrons from the core can scatter, and if their residual energy is over the threshold, they can be detected, adding to a background of noise. The high-density collimation material is effective at reducing these background radiations before reaching the hodoscope.

The TREAT Hodoscope

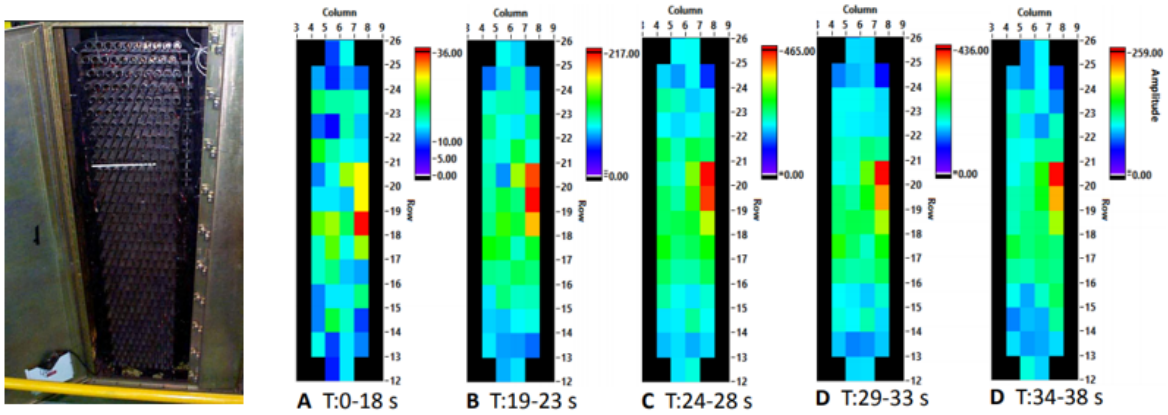

Figure 2-12. Array of fast neutron detectors (left) produce count rate intensity maps of fuel displacement at various transient times, reproduced with permission from OSTI [23].

The TREAT hodoscope was built to evaluates core changes from stress-testing transient experiments by detecting movement of fuel. The hodoscope has an inner concrete collimator and an outer steel collimator, followed by thick lead shielding, finally leading to an array of fast-neutron detectors. There are 334 slots formed from 10 columns and 36 rows (Figure 2-12). The slots were previously equipped with fast-neutron detectors called the Hornyak buttons, each connected to their individual photomultiplier tube to provide information on real-time variations and spatial resolution of fuel motion during transient experiments [2]. Upon restarting TREAT in 2017, about 100 of the Hornyak buttons were deemed functional, and therefore, there was a mounting effort in refurbishing the existing ones or to search for alternatives that alleviated some of the problems faced by the Hornyak buttons.

A variety of fuel motion phenomena have been observed by the TREAT hodoscope, including pin bending, axial and radial expansion, pre-failure motion within cladding, internal fuel motion within annular fuel, fuel breach into coolant channels, sweepout by coolant, eructation, slumping, blockages, breach of flow tube, and compaction. Detectors in the hodoscope array respond to changes in fission density. The data from the detectors, generally in the form of normalized count rates, may be displayed in such a way as to provide a quantitative view of the course of fuel motion. Shown in Figure 2-13 is a hodograph that relates count rates to fuel density.

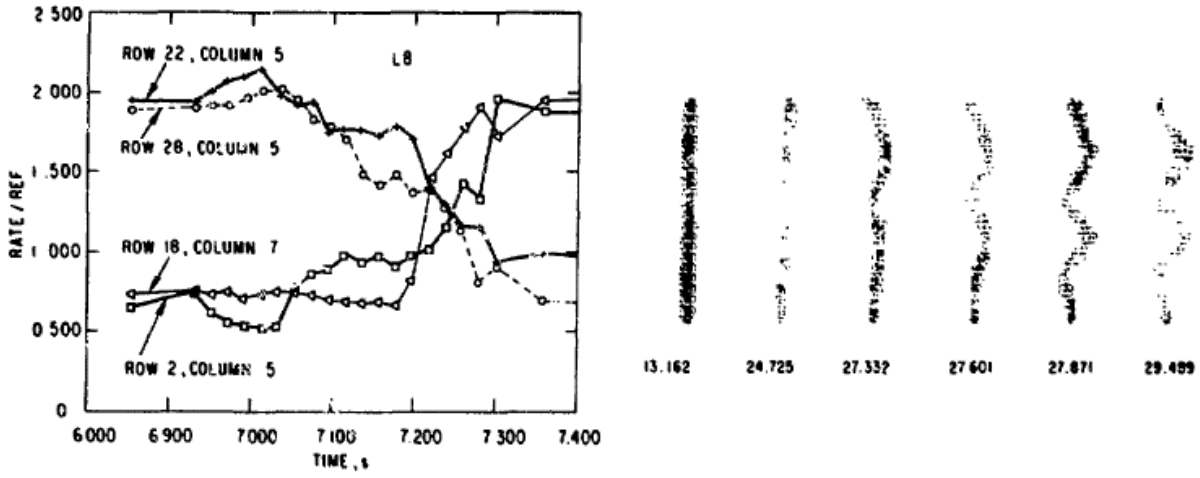

Figure 2-13. Hodographs from [22] showing two-dimensional shaking corresponding to a helical spiral in three dimensions. On the left is a plot of count rate as a function of time during the transient, indicating melting of cladding. On the left is an intensity-modulated hodograph showing fuel pin undergoing bending. Reproduced with permission from OSTI [22].

Interestingly, TREAT is not the only facility utilizing a hodoscope. Scintillating hodoscopes were used by archaeologists and scientists at the Pyramids of Giza to view their internal structures and tombs without breaking down the outer structure or using other invasive methods [24].

2.3.2 Illicit Materials Search Techniques

Active interrogation entails irradiating an object of concern with neutrons or photons and measuring secondary radiation resulting from their nuclear reaction to gain information about the contents of the object. The 'object' in question can be Special Nuclear Materials (SNM), or non-nuclear materials such as hazardous chemicals and explosives. Active interrogation is presently a highly active area for research, and in a fashion similar to the requirements for fuel motion imaging, requires neutron events to be separated from gamma-ray events, in order to be able to identify secondary nuclear reactions, and therefore, the object content accurately. Due to the nature of the process, active interrogation creates a mixed radiation environment that contains elevated background radiation that masks the desired radionuclide signature. A commonly-used technique is to use a source of high-energy gamma rays to induce photofission in the object, leading to neutron emission [25]. Fast scintillators capable of distinguishing between neutrons and gamma-rays, most commonly by using PSD, are usually employed in active interrogation.

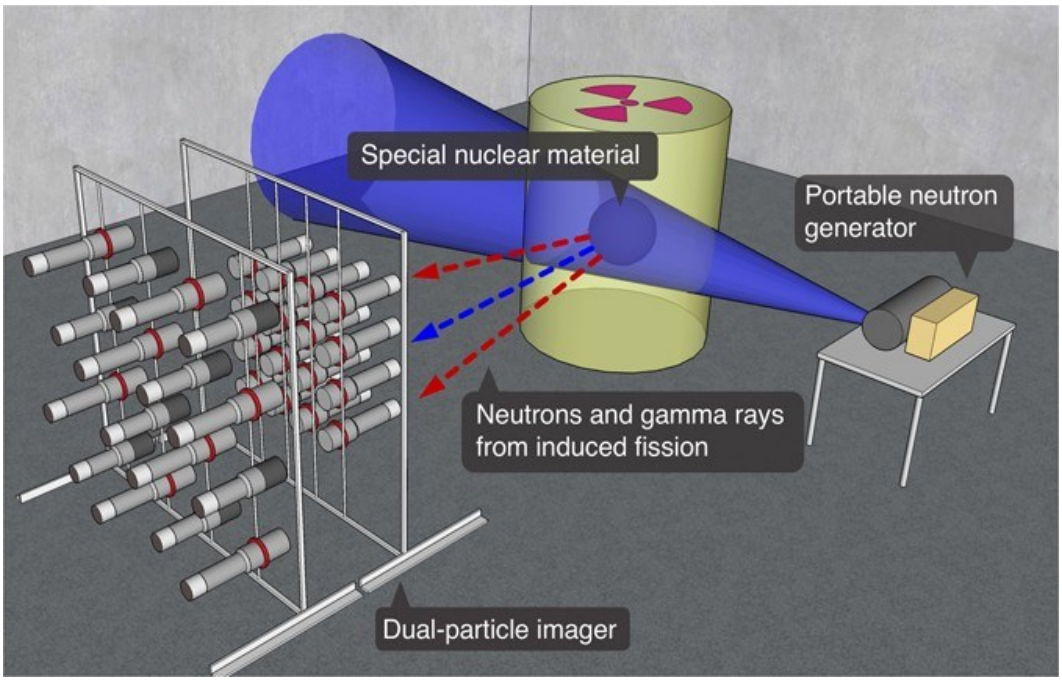

Figure 2-14. Schematic of an active interrogation system, reproduced with permission from Nature Publications.

2.4 Previous Work With Scintillators

The following sections contain information regarding the scintillators that were historically used at TREAT and the techniques commonly used in scintillators for particle discrimination.

2.4.1 The Hornyak Button

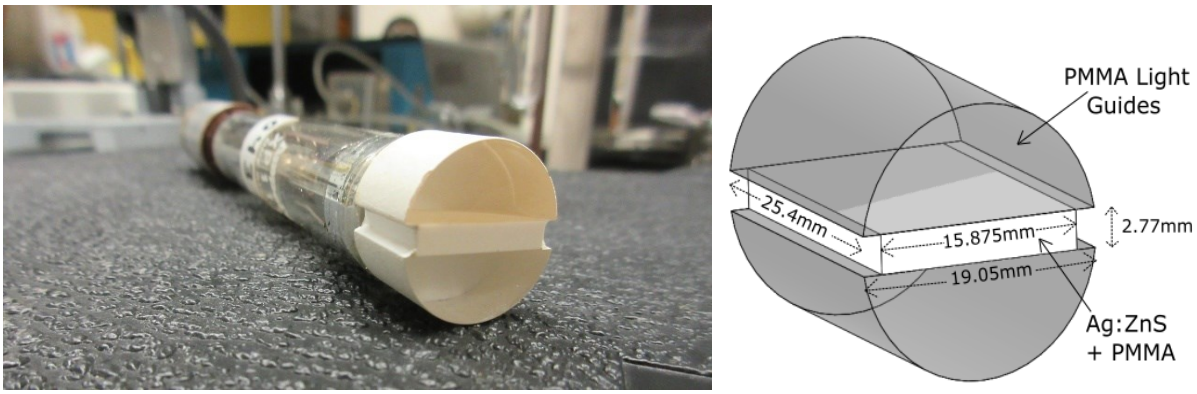

Figure 2-15. The Hornyak button as used in TREAT, connected to a PMT (left), Hornyak button design (right).

The original Hornyak button was introduced in 1952 [71]. Because of its functionality, a type of Hornyak button was identified for use at the TREAT facility with the goal of detecting fast neutrons in a strong gamma-ray background environment. The TREAT Hornyak button design (Figure 2-16) has a scintillation volume containing a mixture of 5% by weight [26] silver-activated zinc sulfide (ZnS:Ag) and polymethyl methacrylate (PMMA) sandwiched between two semi-circular PMMA light guides. One face of the Hornyak button is coated with reflective material while the other face is coupled to a photomultiplier tube (PMT). The total scintillation volume in a 25.4 mm-long Hornyak button is 16.7 mm^3. A pulse can be generated if a fast neutron elastically scatters within the scintillation volume that produces an energetic recoil proton. If the proton then excites scintillation molecules, the released scintillation photons may reach the photocathode window of an adjacent PMT, which may also cause the ejection of a photoelectron into the vacuum envelope.

Challenges with the Hornyak Button

The Hornyak buttons have intrinsic detection efficiencies of 0.4% for neutrons with energies above 0.1 MeV; however, several complications plague the authenticity of the neutron counts registered. For example, background gamma radiation and high-energy gamma rays generated in the collimator steel from neutron capture reactions can interact with a Hornyak button and deposit a distribution of energies, based on the type of gamma-ray interaction, leading to pulses that can be misclassified as neutron counts. In fact, the gamma-ray interactions in the light guides can generate more Ĉerenkov photons than scintillation photons. Although pulse shape discrimination can be used to distinguish between neutron- and gamma-ray events, this introduces additional electronics that can complicate the detection system. Even with PSD, the electrons generated from the interactions can generate Ĉerenkov radiation in the light guides and the PMT photocathode glass, which not only contributes significantly to undesirable background, but also leads to non-linear detector response at higher power levels (refurbished Hornyak buttons were still suffering from this drawback [27]). In fact, the Hornyak button + PMT system has shown to cause gain shift and space charge effects in the PMT, which also results in non-linear detector response. Inaccurate count rates at transients would eventually lead to incorrect mapping of fuel displacement. The fast-neutron detection efficiency of the Hornyak buttons have also been limited

by the “dead” scintillation volume in the center slab, as ZnS + PMMA homogeneous mixtures cause complete light-self absorption at 180 mil.

Beyond 25 mg/cm^2, silver-activated zinc sulfide (ZnS:Ag) absorbs its own light, leading to further loss of events occurring within the scintillation volume. Decay time-based pulse-shaping discrimination techniques, and filters had been developed to overcome light loss, Ĉerenkov background, gamma-ray background [28] and non-linearity [2], but they complicated the detection system.

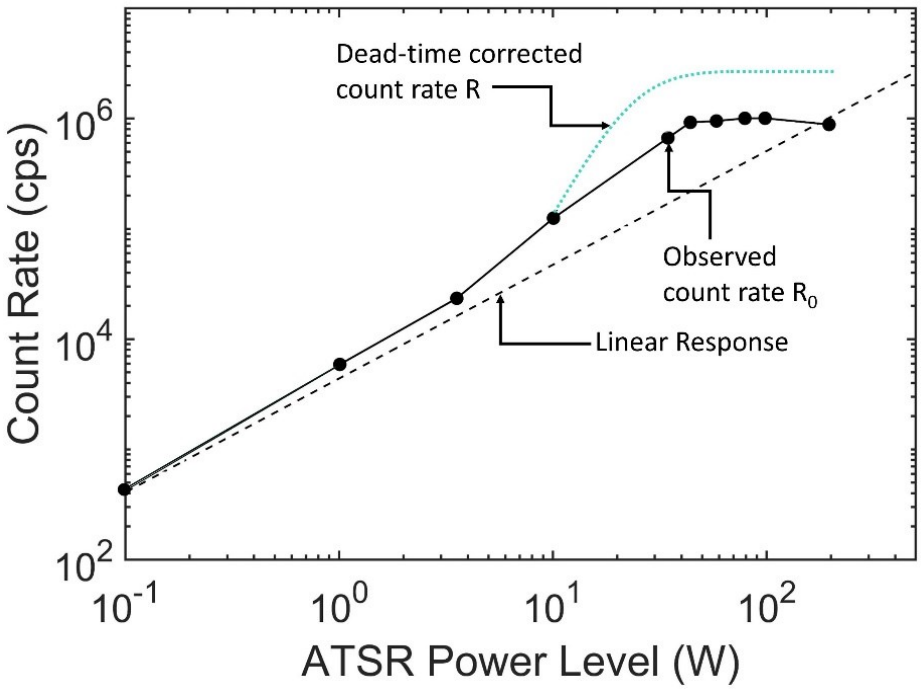

Figure 2-16. Non-linear detector response at high power levels [2].

2.4.2 Neutron/Gamma-Ray Separation

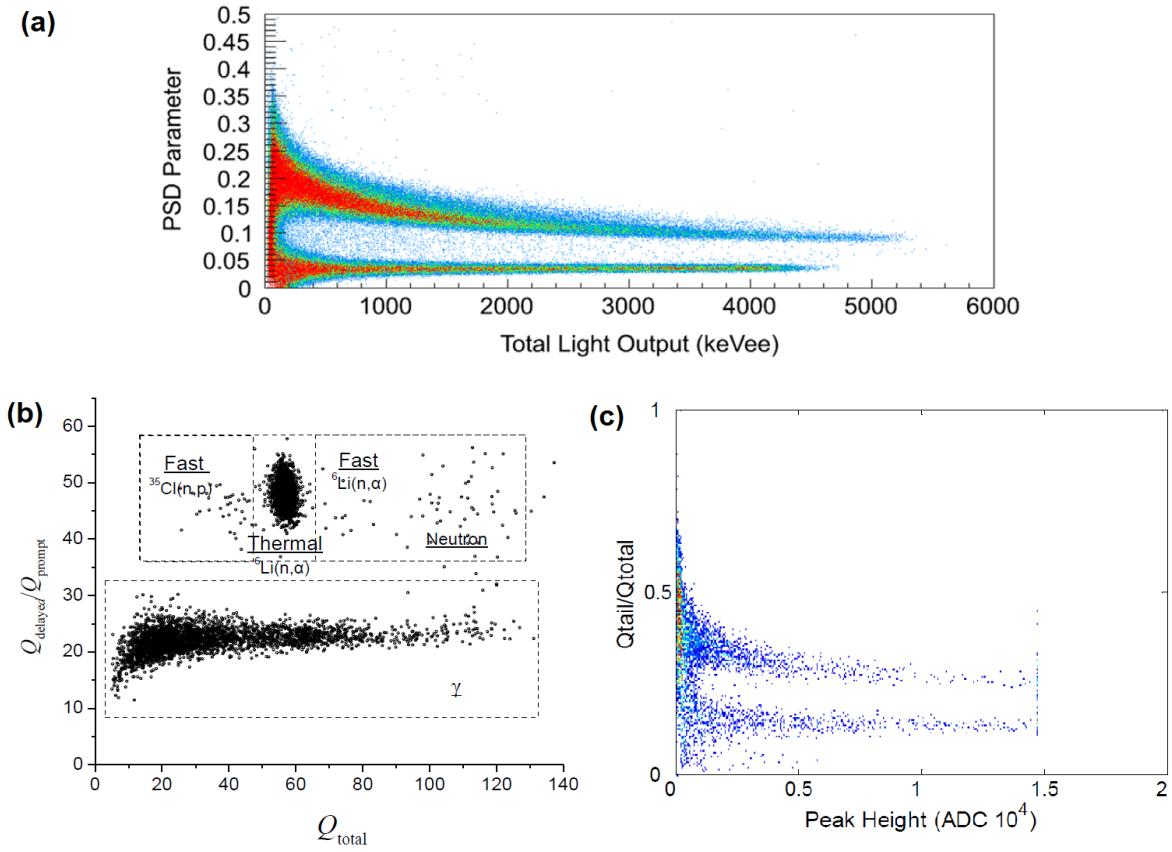

Figure 2-17. PSD Ratio plots of ^{252}Cf irradiation of (a) EJ-301 [29], (b) CLYC [30], and (c) PVT [31], reproduced with permission from Elsevier and Springer [29], [30], [31].

Plastic, liquid and inorganic scintillators have been well characterized in terms of neutron/gamma-ray separation using PSD. EJ-301, a liquid scintillator, has shown an FoM of 2.4 in separating neutrons and gamma rays (Figure 2-17(a)) [29]. The inorganic scintillator $Cs_2LiYCl_6:Ce^3$+(CLYC) has shown a FoM of 2.6 with a separation of fast neutrons, thermal neutrons, and gamma-rays (Figure 2-17(b)) [30]. The plastic scintillator polyvinyltoluene (PVT) has shown a maximum FoM of 1.77 (Figure 2-17(c)) [31]. At very high gamma-ray flux background, the charge integration technique has shown to become inefficient due to pulse-pile up overwhelming the digitizer (Figure 2-18).

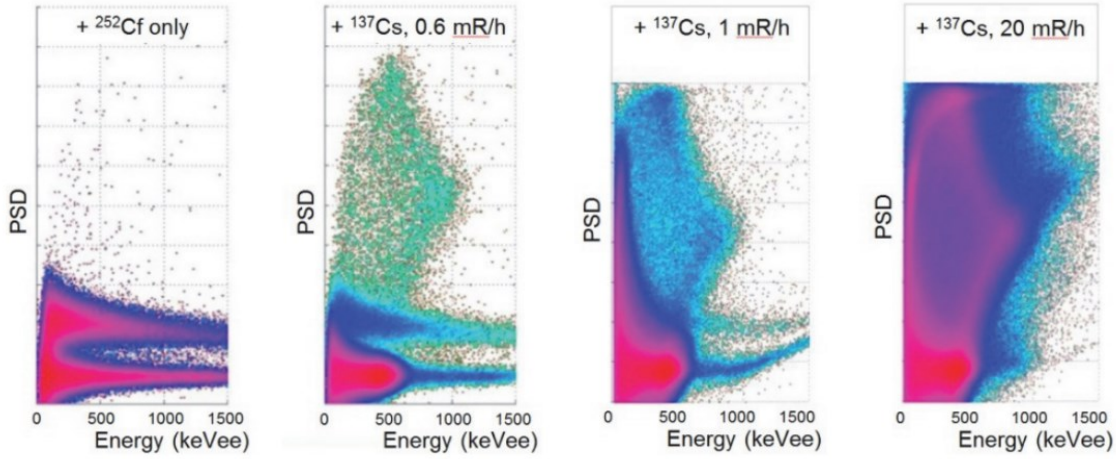

Figure 2-18. Degradation in neutron/gamma-ray separation from a ^{252}Cf source with increasing gamma-ray flux backgrounds [3], reproduced with permission from OSTI [3].

Keeping in mind the shortcomings of the current needs in reactor safety and active interrogation, and the potential of various scintillator materials and detection techniques, efforts were undertaken to provide technological solutions by best utilizing material properties and detection techniques mentioned in this chapter.

Chapter 3 - Design of the MLFD

The MLFD was designed with the aim of increasing neutron detection efficiency, reducing gamma-ray sensitivity and Ĉerenkov radiation, and selecting material and geometry to best reflect these aims. Other designs that were considered while optimizing the features of the MLFD have also been discussed in this chapter. Finally, the well-established procedure to fabricate the MLFD has been discussed in detail.

3.1 Designing the MLFD

Both inorganic and organic scintillators are used for fast neutron detectors. Inorganic scintillators can be located adjacent to a recoil medium, such as a hydrogenous material, and fluoresces from the interactions of recoil ions entering the scintillator. Organic scintillators are usually deployed as a combined recoil-fluorescence detector, in which proton (or carbon) recoils from fast neutrons in the organic compound subsequently fluoresce the scintillator. Presently, organic scintillators are generally used over inorganic scintillators for fast neutron detection. Although pulse height discrimination can be used to distinguish between fast neutron and gamma-ray events, the distinction can be greatly enhanced by using organic scintillators designed for pulse shape analysis. However, in applications which have intense gamma-ray fields, the discrimination becomes less effective for organic scintillators due to neutron signal corruption at higher gamma-ray fluxes [3], thus limiting measurement of the neutron spectra. Additionally, inorganic scintillators generally have higher light yield than organic scintillators. The MLFD was designed combining the positive traits of organic compounds for neutron conversion and inorganic scintillators for scintillation.

3.1.1 Material Selection, Geometry and Orientation

The neutron-converter material is typically selected based on its hydrogen concentration and radiation-hardness. Paraffin, PMMA, and cellulose acetate have high hydrogen/carbon ratios (2, 1.3, and 1.1 respectively). However, PMMA has greater optical transparency than paraffin, is radiation-hard unlike cellulose acetate [33], and exhibits the least autofluorescence among all plastics [34], making it the most desirable candidate. Hydrogen and carbon are both poor absorbers

of gamma rays. According to Astra Products, the supplier of the Clarex^{TM} PMMA disks used in the MLFD, the PMMA exhibits lower autofluorescence compared to standard PMMA due to the pure monomer used as the base ingredient. Low autofluorescence is a desirable property for scintillation systems, as it makes data more reliable in terms of the origin of the scintillation light.

As was described in section 2.2.2, a scintillator is chosen based on a high light yield, optical transparency, and suitable emission wavelength to match that of the photodetector. Furthermore, special properties may be desired based on the specific application. In addition to the previously-discussed properties, the background at TREAT required the detector to be insensitive to gamma rays—an important determining factor for the type of scintillator considered.

The Case for Zinc Sulfide (ZnS)

ZnS is a polycrystalline scintillation material with a wide band gap (approximately 3.91 eV for hexagonal and 3.54 eV for cubic form). ZnS can be activated with copper, silver, manganese, etc. Manganese decreases luminous intensity for ZnS at 450 nm, but increases it at 600 nm, which is not a wavelength that is well-matched with PMTs. Copper produces a plateau wavelength up to about 550 nm, which is also not well-suited to PMTs [35]. Nickel causes luminescence quenching by acting as electron trapping centers resulting in non-radiative recombination [36]. Activating ZnS with Ag enhances luminescence at 450 nm, which increases with dopant concentration up to 2% by weight of Ag nanoparticles [37].

ZnS:Ag also introduces additional neutron-induced proton flux by a threshold (n, p) reaction with ^{32}S (approximately 32% of the counting rate observed from a ZnS–Lucite mixture [32]), thereby further increasing fast neutron detection rate. In fact, this reaction predominates when the discriminator bias is set beyond 2 MeV [2]. However, polycrystalline ZnS:Ag is opaque to its own luminescence for thicknesses greater than 25 mg/cm^2 [38] due to internal reflections and light absorption, thereby making it difficult to develop a detector from a large single crystal of ZnS:Ag.

To circumvent this limitation, the ZnS:Ag can be oriented in optically-independent alternating sections. The sections can be separated by slices of PMMA, acting as both a neutron converter as well as light guide. An alternating layered design would facilitate the inclusion of a

larger total amount of scintillating material while simultaneously reducing the probability of light self-absorption by limiting the individual layer thickness. In the past, layered devices have been investigated to achieve a higher gamma-ray discrimination ratio and increase the interaction rate of neutrons [39], but their efficiency has been limited mostly due to the opacity of the scintillation layers [40]. By fabricating microscale layers of ZnS:Ag, the design can overcome the shortcomings of this promising scintillator.

Lastly, specific to the requirements at TREAT, a critical reason for considering ZnS:Ag is based on the large difference in the specific energy loss (dE/dx) of protons (or other heavy ions) and electrons in the scintillator material. If the particle size is chosen to be comparable to the range of the protons (35 μm for a 2 MeV proton) but much less than that of the recoil electrons (1.46 cm for a 2 MeV electron), the scintillation pulses due to the former will be larger than the electron scintillation pulses, thereby reducing the detector response for gamma-rays. Thus, ZnS:Ag has a relatively high light yield for heavy, charged particles (50,000 photons/MeV) but a low conversion efficiency for fast electrons [41], thereby allowing for discrimination of heavily-ionizing particles in an intense gamma-ray background. ZnS:Ag grains of 25 μm average diameter (Figure 3-1) were used to provide inherent insensitivity to gamma rays.

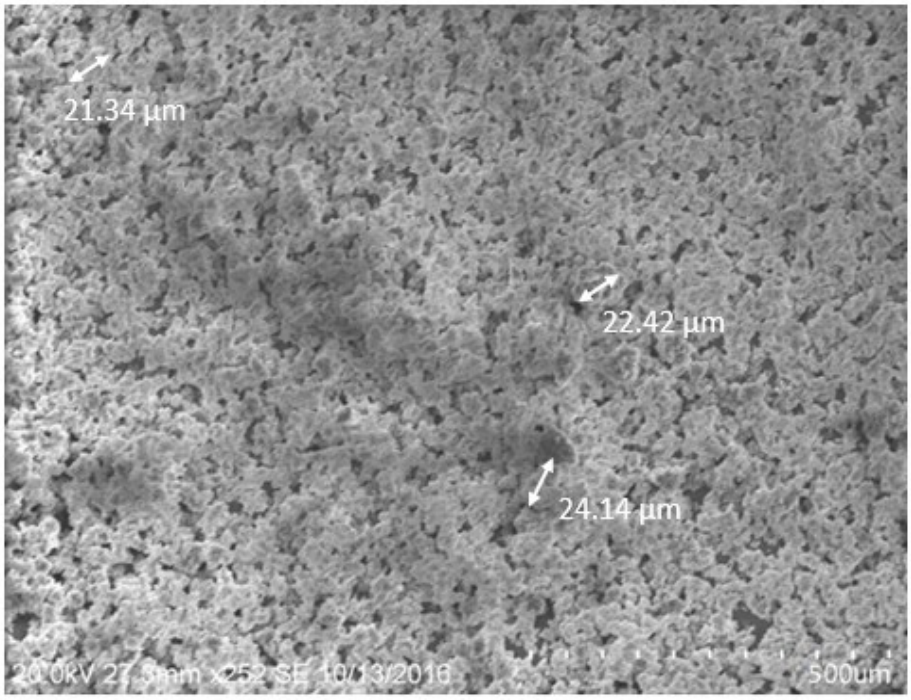

Figure 3-1. SEM image of ZnS:Ag grains as obtained from Eljen.

Ĉerenkov Removal

Various techniques have been employed to reduce Ĉerenkov radiation by filtering or subtracting the noise from the scintillation signal, or by reducing its generation, but these techniques lead to increased complexity in the detection system [42]. The most efficient optical filtering reported removes 82% of the Ĉerenkov signal, but resulted in losing 56% of the scintillation light as well [43]. Unlike the Hornyak button, the layered design would require no extraneous light guides; hence removing that contribution to Ĉerenkov generation. Orienting the light collection device on the side face of the detector (Figure 3-2) instead of collecting light from the end (as in the case of the Hornyak button) can also greatly reduce Ĉerenkov contamination. \Because Ĉerenkov radiation is still generated in the PMMA layers, which propagates in the direction of the interacting charged particle, a portion of forward-propagating Ĉerenkov photons is rendered undetectable by the light-detector. The minimal Ĉerenkov background that may be generated in the PMMA layers can be removed by simple pulse-height discrimination. Additional methods of Ĉerenkov removal are not required. The detection mechanism in an MLFD is illustrated in Figure 3-4.

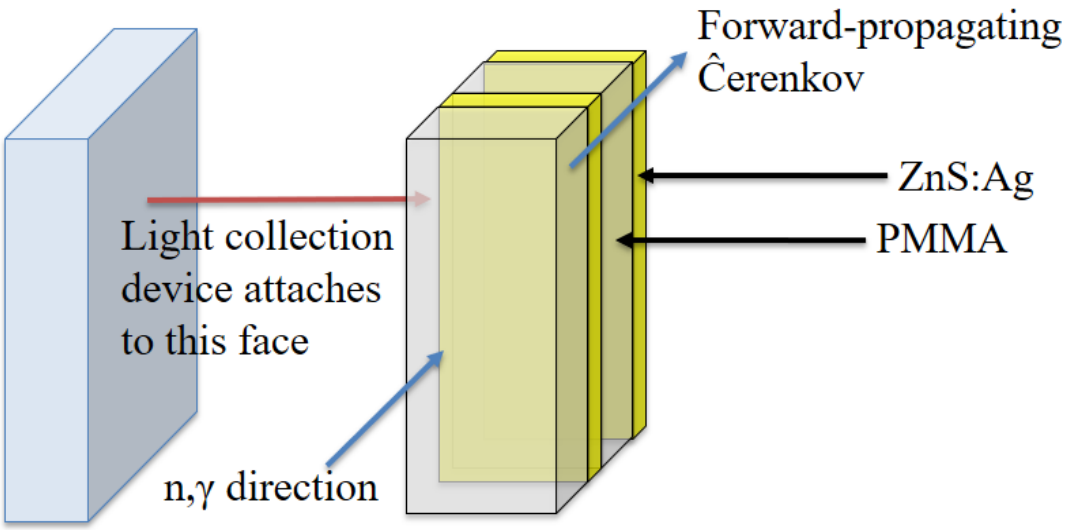

Figure 3-2. Design and orientation of the MLFD.

A two-part homogeneous epoxy ($C_{21}H_{25}ClO_5$) was used to bind the layers together. It had an optical transparency of 97% at 450 nm. The presence of the epoxy in the ZnS:Ag layer reduces the advantage of forward-propagating protons in the ZnS:Ag layer and therefore lowers their

probability of interaction. The homogeneous mixture of epoxy and ZnS:Ag consequently also causes lower interaction of forward-propagating Ĉerenkov and gamma rays, a desirable quality.

Finally, it is beneficial to enclose scintillators in Lambertian reflectors to reduce variance in light collection. Teflon tape and $Mg(OH)_2$ paint are commonly used Lambertian reflectors. Various ratios of $Mg(OH)_2$ with resin, and Teflon tape were compared for their reflectance using a UV-Vis spectrometer. All samples had the same thickness of 0.5 mm. The Teflon tape was observed to exhibit the highest reflectance at 450 nm (Figure 3-3). $BaSO_4$ was used as the reference to compare the sample reflectors.

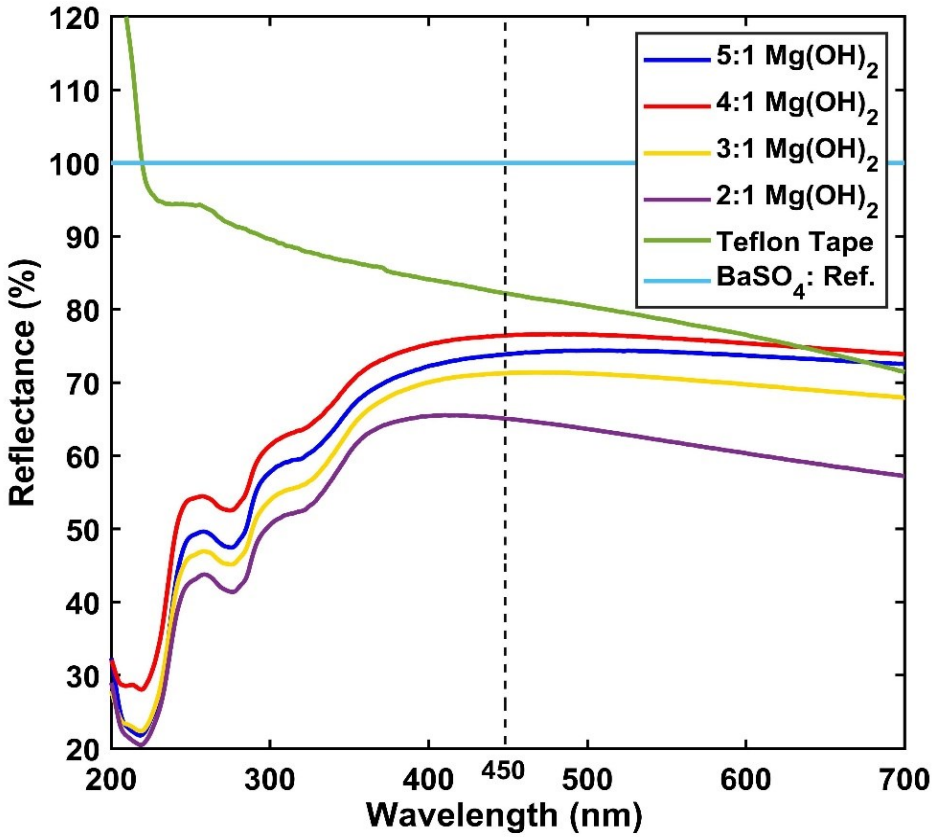

Figure 3-3. Reflectance of Lambertian reflectors.

Thus, the concept of the "Micro-Layered Fast Neutron Detector", or MLFD, was conceived, and it became imperative to optimize the geometry and dimensions for detector performance.

Angular distribution of Ĉerenkov photons

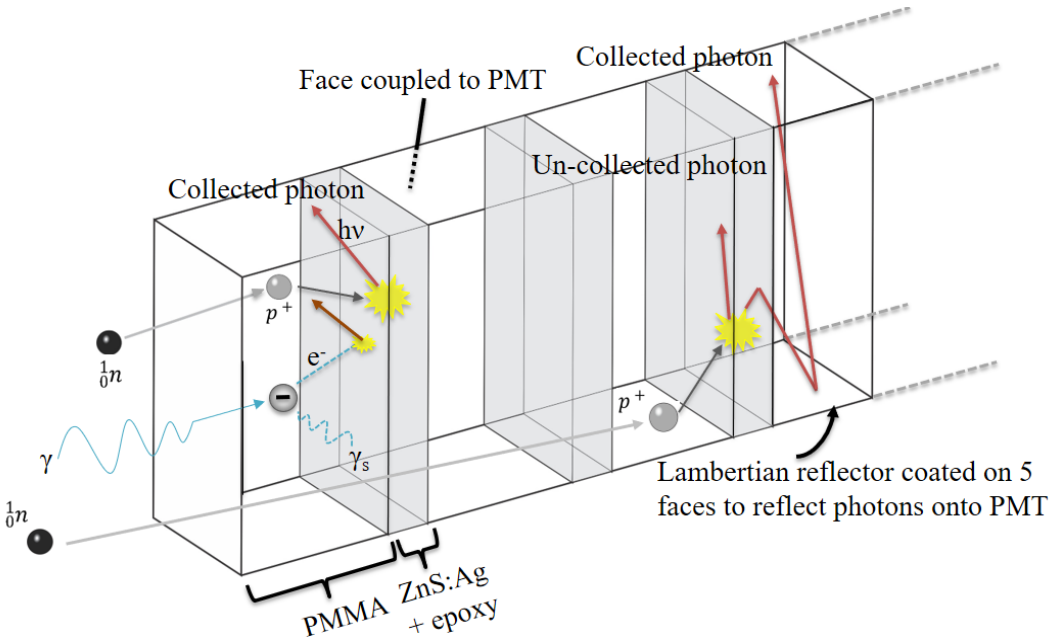

Figure 3-4. Mechanism of detection in MLFD.

At TREAT, the direction of neutrons and gamma rays are known—a collimated beam perpendicular to the 8 × 3 mm face of the MLFD (see Figure 3-4). If the energy of a gamma ray (E_γ) is greater than 320 keV, as determined by equation (2.4) for PMMA (refractive index n = 1.49), and the gamma photon undergoes Compton scattering, then at certain angles of the recoil electron emission Ĉerenkov emission can take place.

To detect the scintillation photons emitted by the scintillator, a photosensor such as a PMT or SiPM is coupled to the scintillator. The best photodetector orientation can be determined by optimizing the collection of two processes: the isotropic scintillation and anisotropic Cerenkov radiation. To determine the direction of Cerenkov propagation, the Klein-Nishina cross-section gives the angular distribution probability of Compton scattered photons and their corresponding recoil electrons. If the recoil electron has velocity greater than the speed of light in PMMA, the probability distribution of the Cerenkov cone angles can be derived.

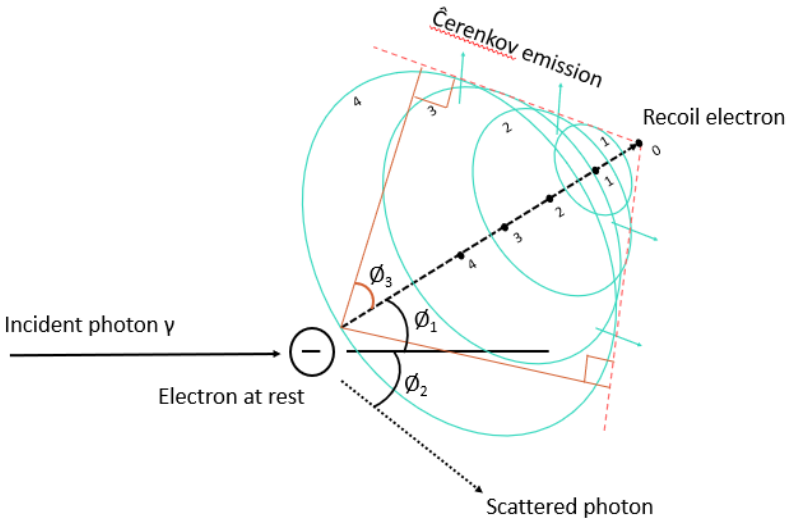

Figure 3-5. Compton scattering of gamma-ray photons above threshold energies (for Ĉerenkov radiation) and eventually generating Ĉerenkov radiation.

In a Compton scattering event, the recoil electron scattering angle ($Ø_1$) and the scattered photon angle ($Ø_2$), as shown in Figure 3-5, are related as:

$$\cot Ø_1 = \left(1 + \frac{E_y}{mc^2}\right) \tan \frac{Ø_2}{2} \tag{3.1}$$

where mc^2 is the rest mass energy of an electron.

The differential scattering cross section per electron for incoherent scattering was given by Klein and Nishina as [4]:

$$\frac{d\sigma_{KN}(E_\gamma, Ø_2)}{d\Omega_s} = \frac{1}{2} r_e^2 \frac{E'}{E_y} \left[1 + \left(\frac{E'}{E_y}\right)^2 - \frac{E'}{E_y} \sin^2 Ø_2\right] \tag{3.2}$$

where r_e is the classical electron radius with a value of 2.8179×10^{-13} cm, $d\Omega_s$ is the total differential solid angle. E'/E_y is given by:

$$\frac{E'}{E_y} = \frac{\frac{mc^2}{E_y}}{\frac{mc^2}{E} + 1 - \cos \emptyset_2} \tag{3.3}$$

The solid angle changes with angle as:

$$\frac{d\Omega_s}{d\emptyset_2} = 2\pi \sin \emptyset_2 \tag{3.4}$$

The angular distribution probability of photon scattering is obtained by multiplying equations (3.2) and (3.4):

$$\frac{d\sigma_{KN}(E_\gamma, \emptyset_2)}{d\emptyset_2} = \frac{1}{2} r_e^2 \frac{E'}{E_y} \pi \sin \emptyset_2 \left[1 + \left(\frac{E'}{E_y}\right)^2 - \frac{E'}{E_y} \sin^2 \emptyset_2\right] \tag{3.5}$$

To obtain the probability of angular distribution of the recoil electrons, equation (3.1) was substituted for sin $\emptyset_2$ in equation (3.5) by using trigonometric identities, given by equation (3.8):

$$\tan \frac{\emptyset_2}{2} = \sqrt{\frac{1 - \cos \emptyset_2}{1 + \cos \emptyset_2}} = \frac{\cot \emptyset_1}{1 + \frac{E_y}{mc^2}} = x \tag{3.6}$$

$$\rightarrow \sin \emptyset_2 = \sqrt{1 - \left(\frac{1 - x^2}{1 + x^2}\right)^2} \tag{3.7}$$

$$\frac{d\sigma_{KN}(E_\gamma, \emptyset_1)}{d\emptyset_1} = \frac{1}{2} r_e^2 \frac{E'}{E_y} \pi \sqrt{1 - \left(\frac{1 - x^2}{1 + x^2}\right)^2} \left[1 + \left(\frac{E'}{E_y}\right)^2 - \frac{E'}{E_y}\left(1 - \left(\frac{1 - x^2}{1 + x^2}\right)^2\right)\right] \tag{3.8}$$

The Ĉerenkov cone angle will therefore also have the same probability of distribution as equation (3.8), with the angular distribution obtained from the recoil electron velocity, which in turn is dependent on the energy of the original photon and scattered photon angles. The Ĉerenkov cone angle:

$$\cos \emptyset_3 = \frac{1}{\beta n} \tag{3.9}$$

where n is the index of refraction, and β is the speed of the recoil electron divided by the speed of light.

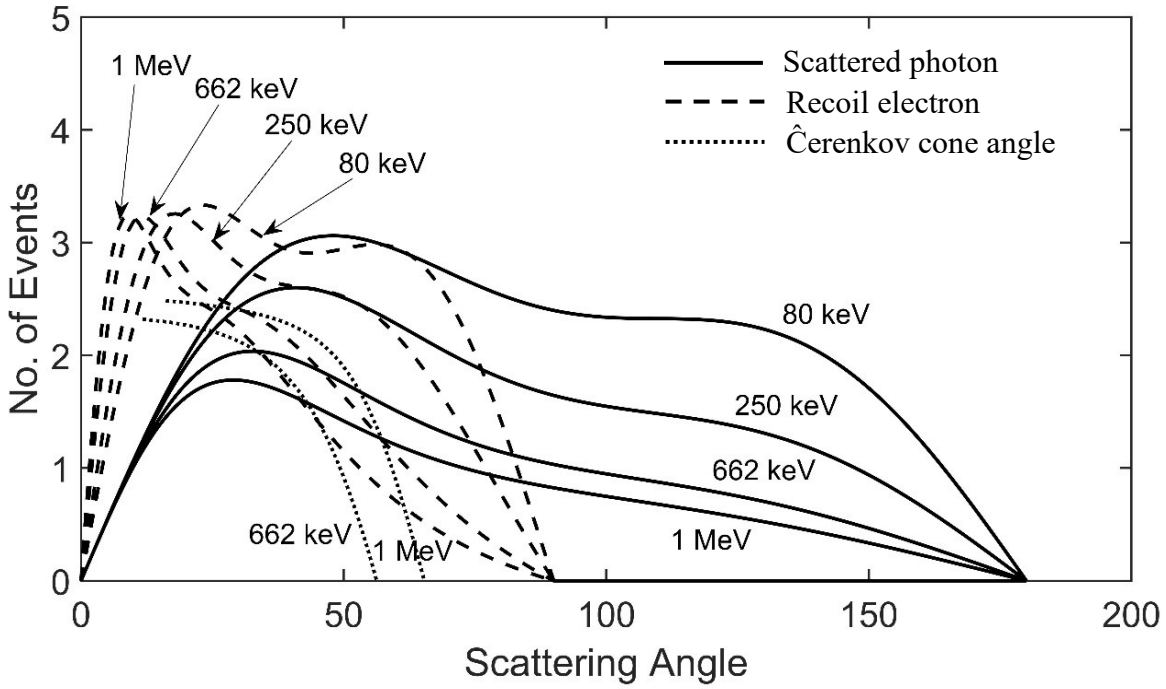

Figure 3-6. Angular distribution probabilities for scattered photons, recoil electrons, and Ĉerenkov emission.

Photodetector orientation

In Figure 3-6, the Ĉerenkov emission angle distribution for the 80 keV is absent because a minimum recoil electron energy of 178 keV is required to generate Ĉerenkov radiation. For the 250 keV gamma ray, the probability of Ĉerenkov angular distribution is negligibly low. Therefore,

lower energy gamma rays do not contribute to appreciable Ĉerenkov emission. The Ĉerenkov radiation from higher energy gamma rays was found to be forward-propagational.

The orientation of the photodetector can be selected by determining the dominant direction of the Ĉerenkov propagation angles. The photodetector can be attached either to the end or to the side of the MLFD. To quantify the effect of photodetector orientation, first, a solid slab of PMMA and ZnS mixture was modeled with the photodetector coupled to the side or end, with respect to the direction of n/γ beam (Figure 3-7). A solid slab was modeled instead of the layered design to study the effect of photodetector orientation on Ĉerenkov photon collection without the additional effect that the layers would have. This would make the comparison between the end and side orientations non-uniform because the layered configuration is "anisotropic"—it is geometrically different from a side or end-view. Using the probability distribution of Ĉerenkov cone angles, for a 662 keV gamma ray, the side orientation exhibited 6% Ĉerenkov photon collection while the end orientation exhibited 8%. Comparatively, the side orientation had 36% collection of scintillation photons while end orientation had 23%. This proves that the side orientation is beneficial in reducing forward-propagating Ĉerenkov but enhances scintillation photon collection which is isotropic. Finally, the layered MLFD was shown to have a scintillation photon collection of 60% and 6.6% for Ĉerenkov photons. The percentage values have been normalized to the total number of Ĉerenkov photons generated in the volume, which for both orientations were modeled for 662 keV gamma rays.

Although the solid slab model has been used to determine the best photodetector orientation for the MLFD for reasons mentioned in the previous paragraph, the Hornyak Button center slab is akin to this solid slab model. However, the Hornyak Button half-moons would contribute to Ĉerenkov photon generation as well, which would lead to higher total Ĉerenkov photon collection.

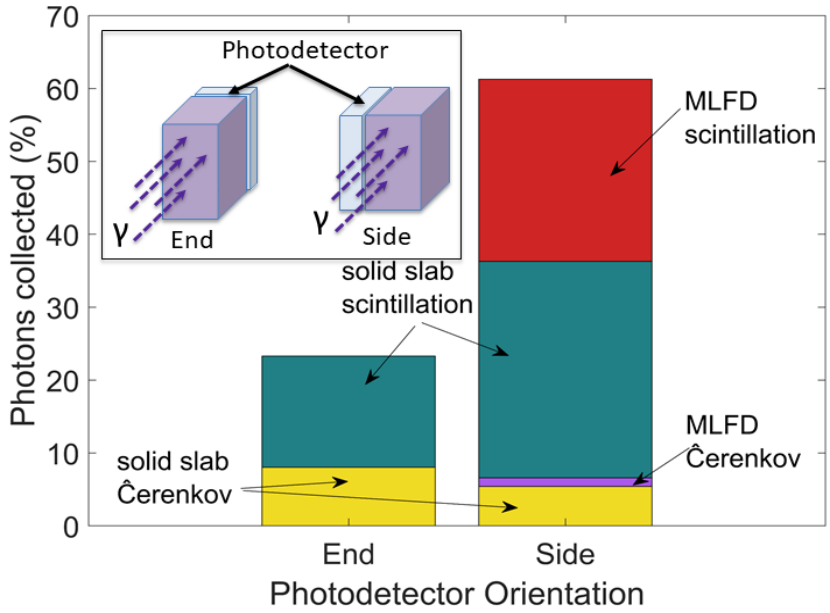

Figure 3-7. Photodetector orientation effect on the Ĉerenkov and scintillation photon collection for a 662 keV gamma ray.

A few reasonable assumptions are made in these calculations; firstly, the gamma rays strike perpendicular to the face of the MLFD, and secondly, the attenuation of the Ĉerenkov radiation in the MLFD is neglected. The Ĉerenkov photons refract through the layers following Snell's law. Total internal reflection sets in at 39.34º in traversing from the ZnS layer to the PMMA layer, so at angles greater than that, only events at the edges of the MLFD might lead to the Ĉerenkov photons either escaping the scintillators or collected at the photodetector. If the total Ĉerenkov angle is greater than 39.34º, it would get "trapped" and absorbed in the ZnS layer, but if the event occurred near the edges of the MLFD, the Ĉerenkov photons can either escape the MLFD or reach the photodetector. Recoil electrons have higher probability of a narrow scatter angle, especially for higher-energy gamma rays (Figure 3-6). The Ĉerenkov photons are emitted in the shape of a three-dimensional cone, and propagate in the forward direction with higher probability. Therefore, the MLFD benefits from placing the photodetector on the side, with only lower probability of Ĉerenkov photons reaching the photodetector.

Ĉerenkov Light Yield

For Compton photon scattering angles greater than 90º, the majority of the original photon energy is lost to the Compton recoil electrons. Also, for increasing gamma-ray energies, the

Compton photon scattering angles are increasingly forward-directional (Figure 3-6). Hence, increasing gamma-ray energies impart lower energies to the Compton-scattered recoil electron. To compare the total Ĉerenkov light yield, as well as the subsequent number of Ĉerenkov photons collected in the Hornyak button (end-oriented) and MLFD (side-oriented), the Frank-Tamm equation is used, which determines the number of emitted Ĉerenkov photons per unit track for a given wavelength range:

$$\frac{d^2N}{dxd\lambda} = \frac{2\pi a z^2}{\lambda^2} \cdot \sin^2 \emptyset_3 \tag{3.10}$$

where N is the number of emitted photons, x is the track length, λ is the wavelength interval, and a and z are parameters specific to the material being used. Assuming the material to be PMMA, and the wavelength interval to be between 400 nm and 600 nm (determined by the sensitive interval of the PMT), the equation reduces to:

$$N = 40x \sin^2 \emptyset_3 \tag{3.11}$$

where x is the length traversed by the particle, expressed in mm.

Electron energy loss over the range of interest is less than 1% for the length of the detectors in question, hence electron energy loss, and associated changes in Ĉerenkov radiation, have been neglected in the model. The dimensions of the detectors are much smaller than the total pathlength of the energetic electrons of interest, therefore it was assumed that the average path of the electron was straight. The volumes of the Hornyak button scintillation region and the MLFD were normalized to allow for appropriate comparisons between the two detectors, therefore the Hornyak Button was of length 12.7 mm while the MLFD was 23.5 mm. In addition, two homogenized variants were also modeled. A homogenized variant includes randomly-distributed ZnS grains in a solid volume of PMMA. One variant had the same ZnS volume percentage as the Hornyak Button (1.5%), while the other was the same as the MLFD (6%). The homogenized variant is similar to the scintillation volume of the Hornyak Button, except it does not have any PMMA light guides,

and the light is collected from the sides. Gamma-rays of energy following the ^{252}Cf spectrum were used to irradiate the two detector models such that the 15.9 x 2.8 mm face of the Hornyak button and the 8 x 3 mm face of the MLFD were subjected to the gamma radiation, perpendicularly on the face. A cutoff of 178 keV was applied for the recoil electrons, to be eligible to emit Cerenkov radiation in PMMA (eq. 2.3). The recoil electrons are mostly born in the scintillation volume in the Hornyak button, but they can also result from gamma-ray scattering in the PMMA half-moons, which have been accounted for in the model. MCNP was used to model the detector geometry and gamma-ray scattering, while PTRAC was used to determine the energy and x, y, z coordinates of the gamma-ray scattering interactions. Only Compton scattering interactions were considered. The Klein-Nishina cross sections (Fig 3.6) are already included in MCNP, used to obtain the angular distribution of the Compton-scattered recoil electrons, from which the Cerenkov photons can be tracked. A MATLAB code extracts the coordinates and electron velocity to generate the Cerenkov photons, according to the Frank-Tamm equation (eq. 3.11). The photon can be absorbed in the medium, or re-emitted at a Lambertian surface, or terminated at the collecting surface. The photon track length determines the total number of Cerenkov photons generated, and the optical processes, i.e., optical scattering, internal reflections and remission at Lambertian surfaces, determine the total Cerenkov photons collected at the photodetector surface.

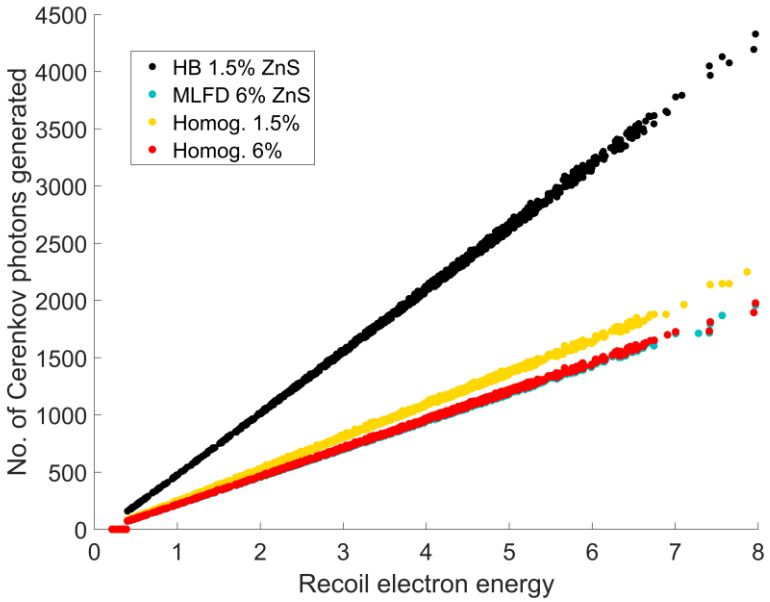

Figure 3.8. The number of Cerenkov photons generated as a function of recoil electron energy for the four different models.

The number of Cerenkov photons generated depends on the recoil electron energy and therefore the Cerenkov cone angle, and also on the distance traveled by the electron in the medium (Figure 3.8). The number of recoil electrons produced due to the gamma-ray scattering interactions that are eligible to produce Cerenkov radiation in the HB and the MLFD are in the ratio 1.84:1. The HB has a larger total volume of PMMA than any of the other three models and therefore has a greater number of Cerenkov photons produced. The Homogenized variant containing 1.5% ZnS produces slightly greater number of Cerenkov photons than the MLFD due to the greater amount of PMMA present. In Figure 3.9, an infinite medium of PMMA and ZnS are considered separately, and the Cerenkov photons produced in each are considered. PMMA results in greater number of photons produced than ZnS for the same electron energy. The greater number of Cerenkov photons in the PMMA explains why the homogenized variant with the greater volume of PMMA has higher Cerenkov photons generated in it than the homogenized variant with the lesser volume of PMMA. The homogenized variant with 6% ZnS and the MLFD have almost identical number of Cerenkov photons generated due to the same volume of each material.

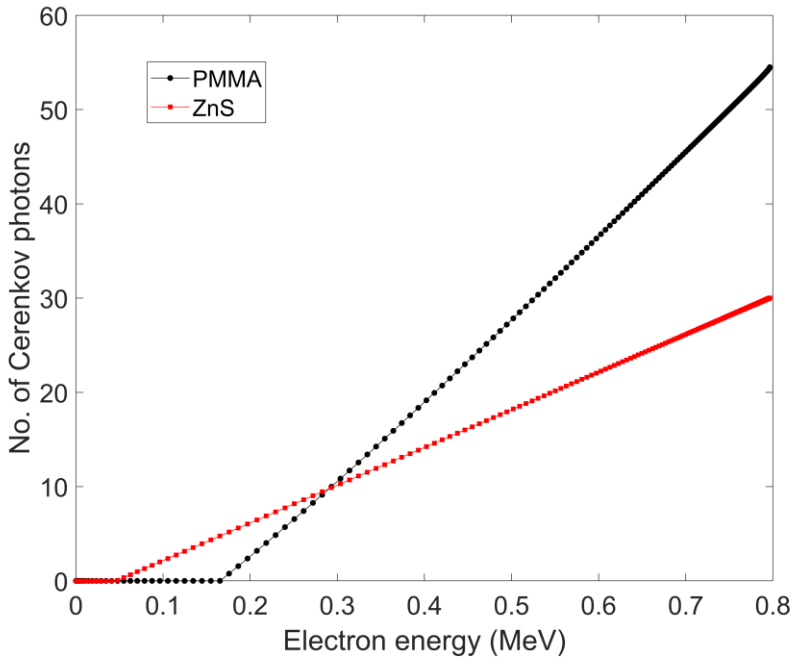

Figure 3.9. The number of Cerenkov photons produced in PMMA and ZnS as a function of electron energy.

Not all Cerenkov photons generated are collected, due to the various optical processes involved in collection. The number of Cerenkov photons collected by the light guide depends on the

arrangement and grain placement of the different materials in the detectors. The number of Cerenkov photons collected in the case of the HB is much greater, once again due to the greater total volume of the transparent PMMA. The trends of the four models are the same as Figure 3.8, except the homogenized variant 6% collected slightly lesser number of photons than the MLFD for the same original gamma energy.

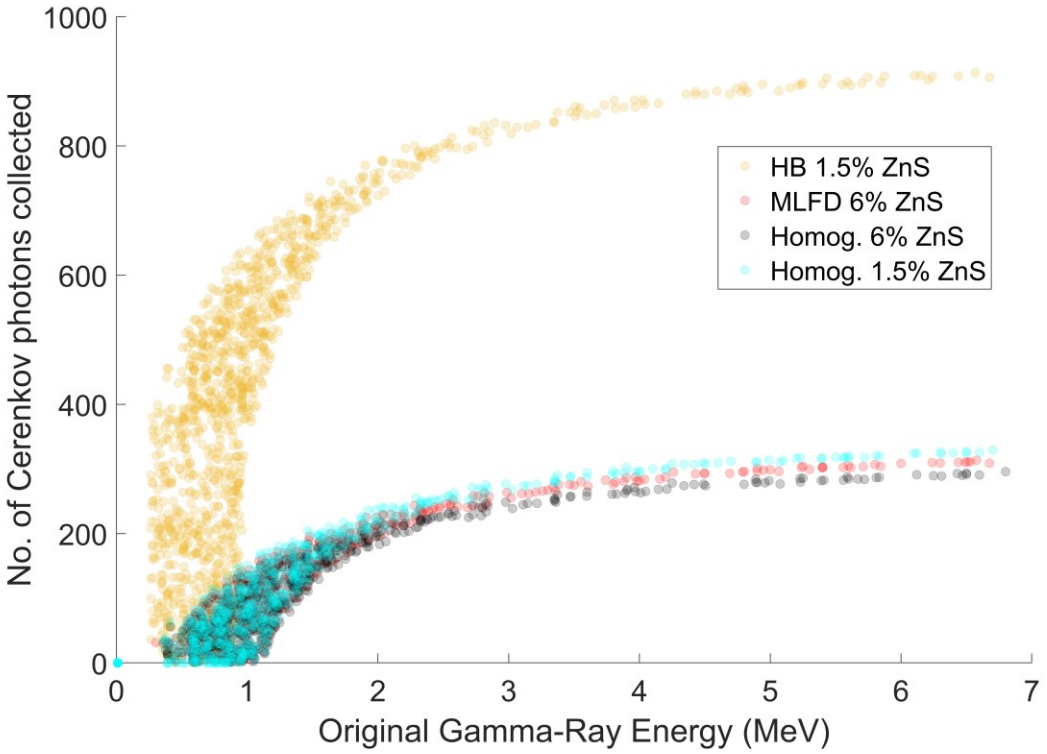

Figure 3.10. Number of Ĉerenkov photons collected by the photodetector as a function of original gamma-ray energy. The black circles represent the HB while the red pentagrams are the MLFD.

The total number of photons collected depends a multitude of factors: the recoil electron energy and therefore gamma-ray energy, optical attenuation and reflection, and detector geometry. Gamma-rays with different original energies can result in an equal number of photons being collected. Conversely, gamma-rays with equal energies can deposit different amounts of Cerenkov photons, due to the two-step process: gamma-ray scattering dictated by Klein-Nishina cross-sections, and Cerenkov generation dictated by Frank-Tamm relations. Unlike scintillation process, the number of Cerenkov photons collected is particle-direction dependent, thus the variation in Cerenkov photons collected with original gamma-ray energy is an amalgamation of the separate processes described above. Overall, the side-oriented MLFD collects lesser Cerenkov photons than

the end-oriented HB, due to lesser PMMA volume, greater amount of ZnS, and the photodetector orientation.

3.1.2 Summary of Geant4 Modeling of the MLFD

Detector geometries, sources and orientation have previously been modeled in Geant4 version 10.2 with patch 02 [44]. The TREAT environment was replicated in the model to retain an accurate description of the neutron and background fluxes. Since gamma rays originate from multiple sources, 5 prompt fission gamma rays per fission neutron, and 9 neutron-activated gamma rays from capture per fission neutron were modeled. The neutron energies followed a ^{235}U thermal fission spectrum, and was considered monodirectional due to the collimator they emerge from.

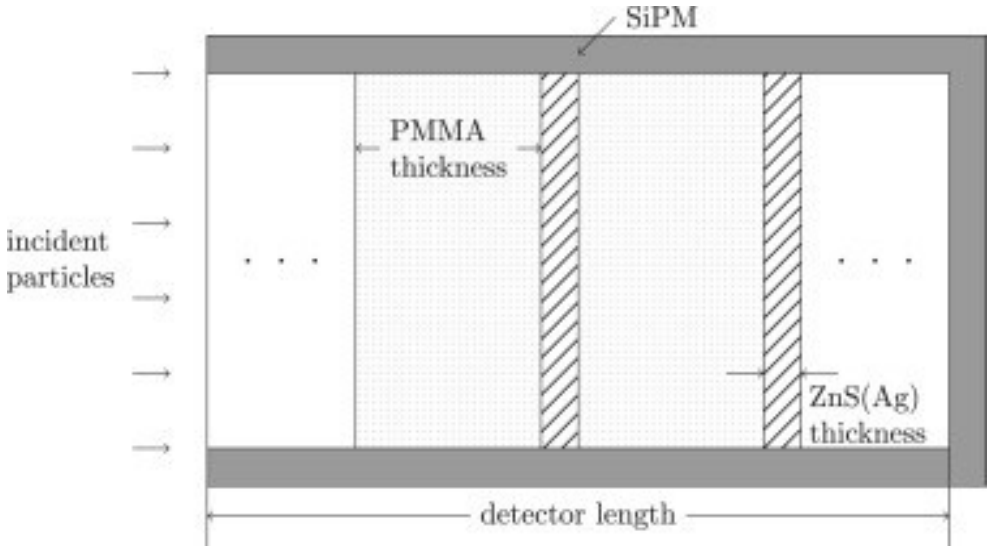

Figure 3-11. Geant4 model of the layered design, reproduced with permission from Elsevier [26].

The layered design was modelled as having a rectangular cross-section of 3 mm × 8 mm, keeping in mind the collimator width and length at TREAT. The PMMA and ZnS:Ag layer thicknesses were varied for optimization, as was the total number of layers. The light was collected from the sides, as shown in Figure 3-11. A 2.54-cm long Hornyak button was also simulated for comparison and validation of the model.

The thicknesses of the PMMA and the ZnS(Ag) layers were important to consider in achieving the optimum performance of the detector. While a thick PMMA layer would increase chances of proton generation and light collection, a large percentage of the recoil protons would

get absorbed in thick layers. According to SRIM (Figure 3-12), the projected range of a 2-MeV proton in PMMA is about 65 m. A parametric study was performed to find the optimal thicknesses of the PMMA and ZnS(Ag) layers for a 5-cm long layered device. The simulations showed that optimum thicknesses are 0.18 mm for the PMMA layer, and 12 μm for the ZnS:Ag layer [26].

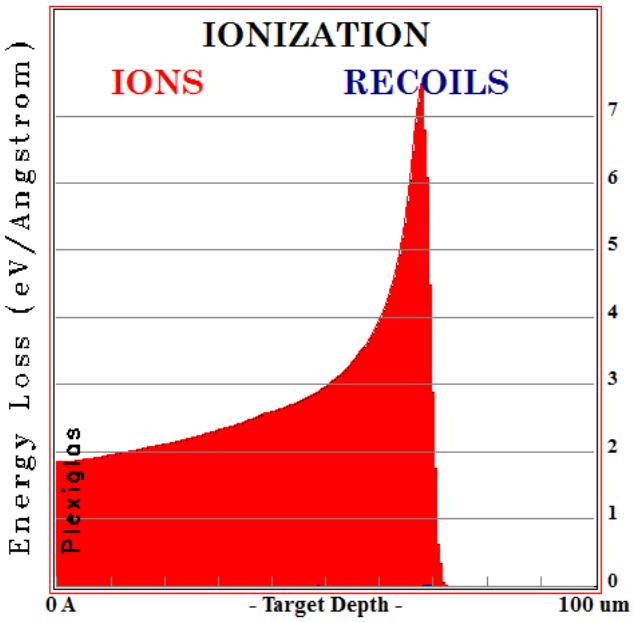

Figure 3-12. SRIM simulation of the Bragg curve for 2 MeV protons in PMMA.

A optical photon spectrum was generated from irradiating a Hornyak button and a 5 cm-long MLFD with neutrons having energies following the ^{235}U Watt fission spectra (as well as fission gamma rays), as shown in Figure 3-13. In the MLFD, Ĉerenkov events was shown to be minimal and can be easily rejected by using pulse height discrimination. The ability of the MLFD to reject gamma radiation was measured by the "*n/γ ratio*", as described by the following equation:

$$n/\gamma \ ratio = \frac{Intrinsic\ fast\ neutron\ detection\ efficiency}{Intrinsic\ gamma\ ray\ detection\ efficiency} \tag{3.12}$$

A *n/γ ratio* of 100 with respect to the background gamma rays is a desirable functional capability of advanced fast-neutron detectors for the hodoscope [45]. The LLD was set to 180 optical photons to have a *n/γ ratio* of 100. The bump in the neutron spectrum at the initial optical photon channels is a feature of the MLFD geometry. The neutron detection efficiency increased

as a function of the detector length at optimized layer thicknesses, and saturated at about 6% for lengths larger than 20 cm. Of course, the length can be limited by the size or number of light collection devices, space allocated for the detection system, and the total cost [26]. A 2.54 cm long Hornyak button has a total scintillation volume of 16.7 mm^3 (including dead region). By compartmentalizing the ZnS:Ag into independent layers, a 2.54 cm long MLFD could contain a useful scintillation volume of 30.5 mm^3.

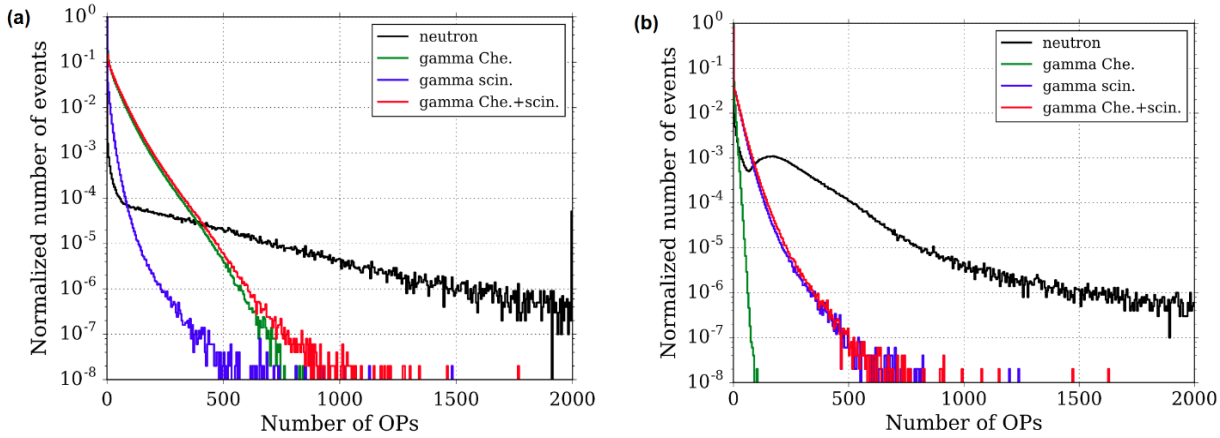

Figure 3-13. Pulse height distributions for (a) 2.54 cm Hornyak button, and (b) 5 cm MLFD with optimized layer thicknesses. OP is optical photons, reproduced with permission from Elsevier [26].

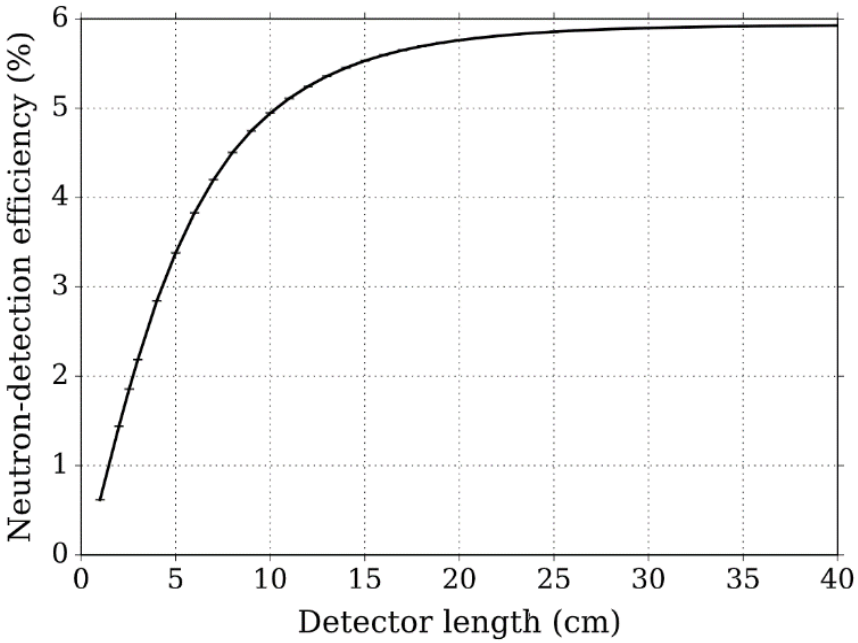

Figure 3-14. The neutron detection efficiency of an MLFD as a function of the detector length, reproduced with permission from Elsevier [26].

For in-lab testing at KSU, an isotropic ^{252}Cf source was modeled, with the neutron and gamma energy spectra represented by equations (2.1) and (2.2). The ^{252}Cf source was enclosed in a steel casket, which absorbed the alpha particles that were emitted. Per fission event, 3.75 neutrons and 8 gamma rays were emitted [46]. The source was placed 10 cm away from the MLFD for point source approximations to be valid. The PHS (Figure 3-15) shows the combined counts from neutron, gamma-ray and Ĉerenkov radiation events, in order to compare experimental results. It is interesting to note the differences in spectra when the MLFD is irradiated by ^{252}Cf versus the MLFD in the TREAT environment. The initial channels (optical photons) are similar for both cases, but in the higher channels (i.e., greater energy deposition), the Hornyak button seems to have slightly higher counts than the MLFD when it is irradiated with an isotropic ^{252}Cf, while the counts are the same for both Hornyak button and the MLFD in the TREAT environment.

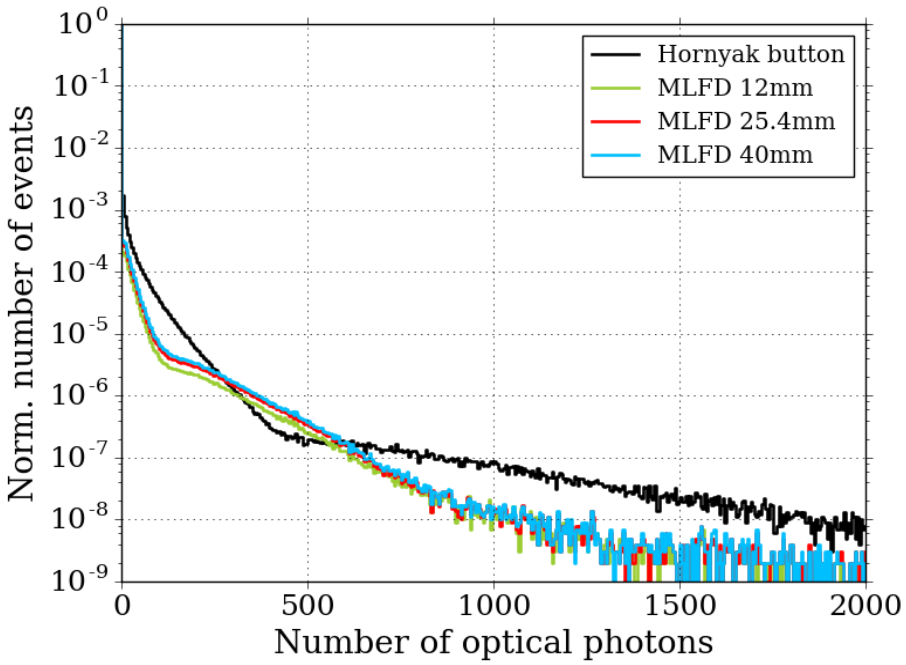

Figure 3-15. Pulse height distributions for the Hornyak button and several lengths of the MLFD when irradiated with a ^{252}Cf source at KSU [47].

SNM Searches

The layered design was originally conceived with the knowledge of the direction of the neutrons. The layered configuration increases the useful scintillation volume, therefore allowing a large amount of scintillation photons to be detectable by a photosensor. Additionally, the forward-

propagational recoil protons have a high chance of encountering a ZnS:Ag molecule (and subsequently, depositing energy in the ZnS:Ag layer) in a layered configuration. However, if the neutron direction relative to the MLFD is variable, then the aforementioned advantages achieved due to the layered configuration may no longer serve their purpose. Therefore, it was imperative to investigate the proton energy deposition in the ZnS:Ag layer when the MLFD is irradiated from different directions, as is usually the case when the source is at an unknown location.

The MLFD and a ^{252}Cf neutron source was modelled using Monte Carlo Neutron Transport (see code in Appendix-#4). A 10.07-mm long MLFD was constructed, that comprised of alternating 200 µm-thick PMMA and 35 µm-thick ZnS:Ag layers (thicknesses along the z-axis), each having a rectangular cross-section of 3 mm × 8 mm (x- and y-axes, respectively). The number of layers of PMMA and ZnS:Ag were 43 and 42, respectively. An isotropic neutron source with energies obeying the ^{252}Cf Watt fission spectrum was placed 5 cm from the MLFD, and two different locations, as shown in Figure 3-16. ^{252}Cf was chosen as the source of neutrons as it was available for experimental validation.

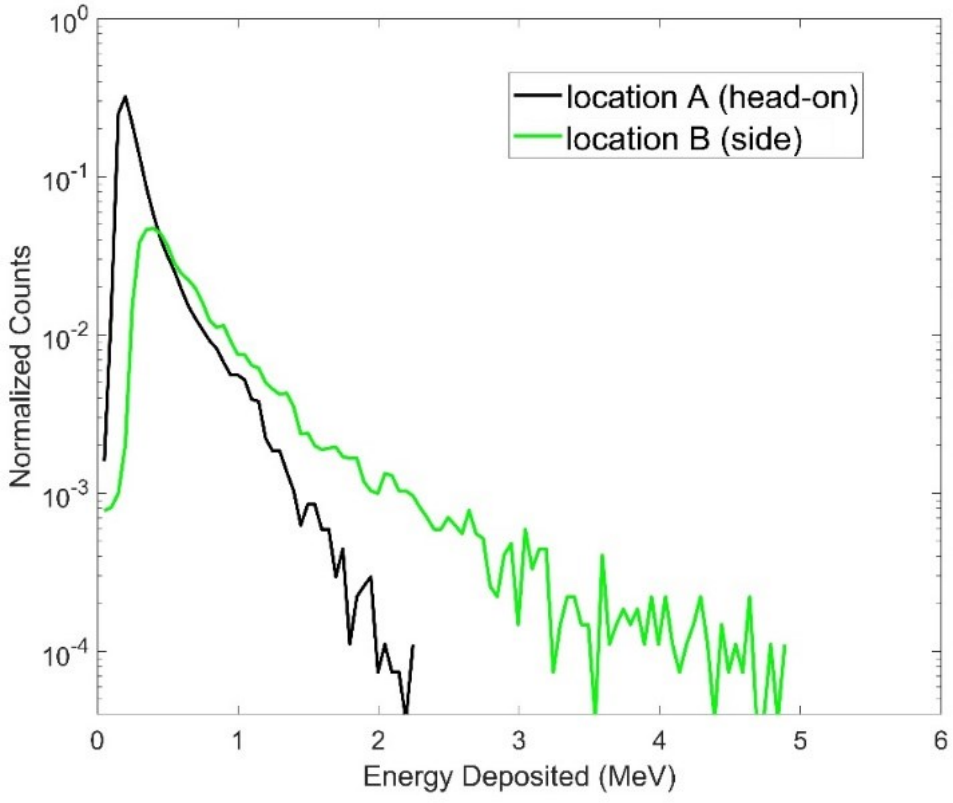

Figure 3-16. Theoretical proton energy deposition in the ZnS:Ag layers for different orientations of the source.

3.1.3 Geometric Optimization for Maximum Photon Collection

In the previous section, the PMMA and ZnS:Ag layer thicknesses were numerically optimized, based on the range of protons in PMMA, the opacity of ZnS:Ag to its own light, and the ZnS:Ag volume necessary to increase chances of scintillation. The MLFD geometry was originally conceived based on the requirements of fuel motion imaging. One of the aspects of the geometry specifically suited towards the TREAT facility was the cross-sectional form factor.

TREAT

The cross-sectional area for the MLFD simulated in Geant4 was chosen to be 3 mm × 8 mm based on the collimator slit aperture [2], and also considering the 6 mm × 6 mm cross-sectional area of silicon photomultipliers (which would need to replace the PMTs currently used in the hodoscope).

Active Interrogation

To investigate the capabilities of the MLFD in SNM searches, it was imperative to tailor the detector to the specific needs of this application. However, with the collimator aperture no longer dictating the detector cross-section, the focus was shifted to optimization of the cross-sectional geometry. Therefore, a Monte-Carlo code was written in MATLAB to model various different geometries and dimensions. Additionally, reflectors were also modelled on the exposed scintillator faces to determine their effect on light collection. Specular surfaces reflect light in specific directions (for example, mirrors), while diffuse surfaces reflect light in all directions (for example, a dry asphalt roadway). While a Lambertian reflector ensures light striking anywhere on its surface has equal probability in reaching a photodetector, a specular reflector can be beneficial in geometries where certain reflecting angles have higher probability in reaching a photodetector.

To investigate the effect of geometry on the fraction of scintillation photons reaching the photosensor, several different cross-sectional shapes of the MLFD were modeled: the previously used rectangle, a semi-circle, a parabola, and a triangle (Figure 3-17). All shapes had the same total area of 14 mm^2. A MATLAB code was written (Appendix-#3) to trace the optical photons in the four geometries according to the laws of optics as described in the following section [48].

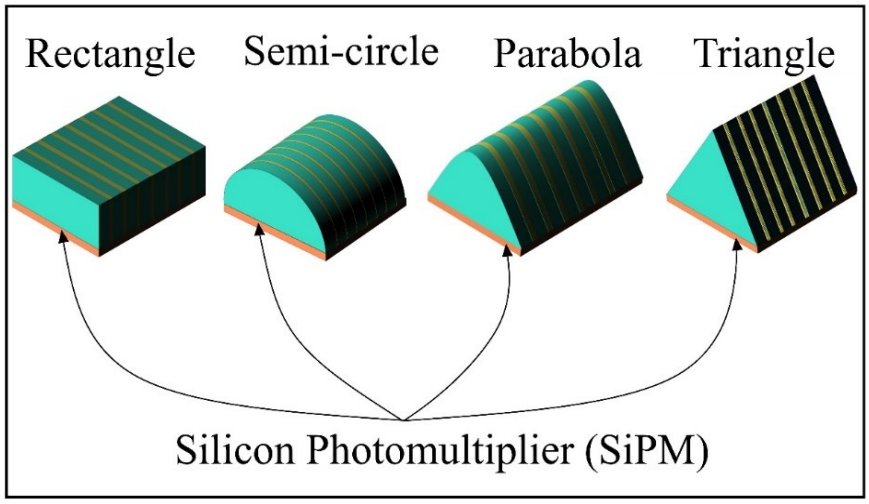

Figure 3-17. Four different cross-sectional shapes of the MLFD were modeled, each with three different cases of reflectors.

Monte-Carlo Transport of Optical Photons in MLFD Light Guides

When electrons or protons interact with the silver-doped ZnS atoms, scintillation photons are born in the ZnS:Ag layer but have higher chances of being "collected" by the SiPM if they enter the PMMA layer. Therefore, the model assumed a uniform distribution of photons in the PMMA layer. To avoid light losses at the surfaces, the MLFD model was wrapped in a reflector at the exposed faces. In fact, the effect of the reflector was also studied in three scenarios: the amount of photons reaching the photodetector without any reflector, with a Lambertian (diffuse) reflector, and with a specular (polished) reflector. Each photon path, of wavelength 450 nm, was modeled to be randomly distinct from the others as determined by the absorption probability in PMMA, and by the probabilities of transmission, reflection, and absorption at the PMMA-reflector (diffuse or specular) or PMMA-air (in the absence of any reflector) interface. The PMMA layer faces a light collecting surface, while the rest of its geometry is either exposed, or is covered in diffuse or specular reflector. The light-collecting surface was modeled after a 6 mm-long SenSL SiPM.

Photon tracing in PMMA

The processes of absorption and beam attenuation in PMMA were specified by the absorption coefficient a (0.03692 mm^{-1}) and the beam attenuation coefficient c (0.03695 mm^{-1}).

To decrease computational time in tracing photons, the code sampled from a biased cumulative distribution function: a photon is traced till it is scattered or reflected and then reduce its weight (intensity of photons) based on the absorption probability. Thereafter, the code resumes tracing the photon with its new weight. Finally, when the weight of the photon is reduced below a certain value specified by the code, the photon path is terminated and it is no longer traced. In such a case, the photon is not collected. If the photon is able to reach the detector plane before its weight is reduced below the threshold, after attenuation and/or re-emission from surfaces, it is collected.

The model assumes a two-dimensional space, so all photon interactions occur in the PMMA layer. In reality, a significant amount of photons would cross into the ZnS:Ag layers on either side of the PMMA, a portion of which would be absorbed in the ZnS:Ag, while others may re-enter another PMMA layer. However, since the PMMA thickness for all geometries remains the same, this effect would be similar in all geometries, and hence was not considered a factor in the model.

Initially, the photon source is considered to be an isotropic source, with an initial weight of w. The source is assigned an originating position of x_0, y_0 and z_0. The azimuthal scattering angle is given by:

$$\emptyset = 2\pi q \tag{3.13}$$

where q is a random number between 0 and 1.

The polar scattering angle is given by:

$$\mu_z = 1 - 2q \tag{3.14}$$

The photon is assigned initial x- and y- direction cosines (which are the x and y components of the unit vector that points in the direction of photon travel), given by the following two equations:

$$\mu_x = \sqrt{1 - \mu_z{}^2}\cos(\emptyset) \tag{3.15}$$

$$\mu_y = \sqrt{1 - \mu_z{}^2}\sin(\emptyset) \tag{3.16}$$

Photon Travel

The probability density function for the attenuation of light with respect to the optical distance travelled is:

$$p(l) = e^{-l} \tag{3.17}$$

The cumulative distribution function to equation (3.17) is:

$$P(l) = \int_0^l e^{-l'}\, dl' = 1 - e^{l} \tag{3.18}$$

P(l) is set to a random number between 0 and 1.

Solving for *l*:

$$l = -\ln\ (q \tag{3.19}$$

The geometric pathlength *s* of the photon in PMMA can be defined as:

$$s = \frac{l}{c} = -\frac{\ln\ (q}{c} \tag{3.20}$$

Given the direction cosines and the photon path length *s*, the photon can be advanced from its initial position to its next location by the following equations:

$$x = x_0 + \mu_x s \tag{3.21}$$

$$y = y_0 + \mu_y s \tag{3.22}$$

$$z = z_0 + \mu_z s \tag{3.23}$$

Photon Reflection, Absorption and Collection

The weight (intensity) of the photon is reduced as the photon travels in the PMMA, as dictated by the absorption coefficient. This is achieved mathematically by multiplying the photon weight by the absorption albedo. As the photons travels through the PMMA, depending on the geometry, the photon may strike either the light-collecting area, or a reflector (or the exposed scintillator surface). In the first case, the weight (intensity) of the photon, if above a certain specified threshold, is collected. In case the photon strikes a Lambertian surface (the reflectivity for which, assuming a perfectly reflecting surface, is unity), its weight is reduced by the diffuse scattering albedo, and the photon is given a new direction as dictated by the following equations:

$$\mu_z = -\sqrt{q} \tag{3.24}$$

$$\emptyset = 2\pi q \tag{3.25}$$

$$\mu_x = \sqrt{1 - {\mu_z}^2}\cos(\emptyset) \tag{3.26}$$

$$\mu_y = \sqrt{1 - {\mu_z}^2}\sin(\emptyset) \tag{3.27}$$

If the photon strikes a specular surface, as with a perfectly reflecting mirror, the reflected angle, with respect to the normal to the surface, is the same as the incident angle. If the scintillator

does not have a reflective layer, then according to Snell's law, the light is reflected if the incident angle is greater than the critical angle (for PMMA this is 41.2 °C) with its weight reduced by the single scattering albedo of PMMA. If it is not reflected, the photon path is terminated and does not get collected.

Shown in Figure 3-18 is 5 sources of photons emitting isotropically in a spherical layer of PMMA wrapped on its faces with an imperfect Lambertian reflector. The weighted ray from photon source 1 was reflected twice from the diffuse reflective surface, but its intensity (photon weight) reduced beyond a specified threshold, hence was not collected (considered absorbed in the medium). Photon source 2 reflected twice from the diffuse surface, and was able to reach the collecting surface while its weight was still above the acceptable minimum intensity threshold. Photon source 3 emitted a ray which was absorbed or transmitted but not reflected when it struck the Lambertian surface, and hence, was not collected. Photon sources 4 and 5 were born closer to the light collecting surface, and also were emitted in a direction that allowed direct collection of the photon without encountering any reflective surfaces. Photon sources 4 and 5 probably resulted in the highest intensity of light collection given that their location was the closest amongst the 5 sources to the light collecting surface.

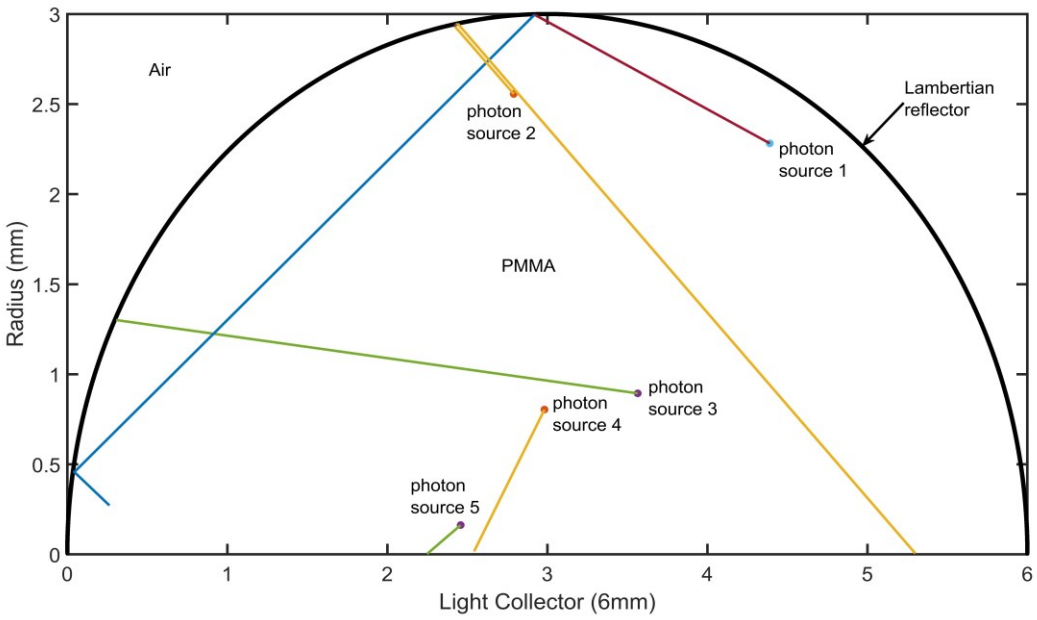

Figure 3-18. Ray tracing of photons in a spherical layer of PMMA with a Lambertian reflector.

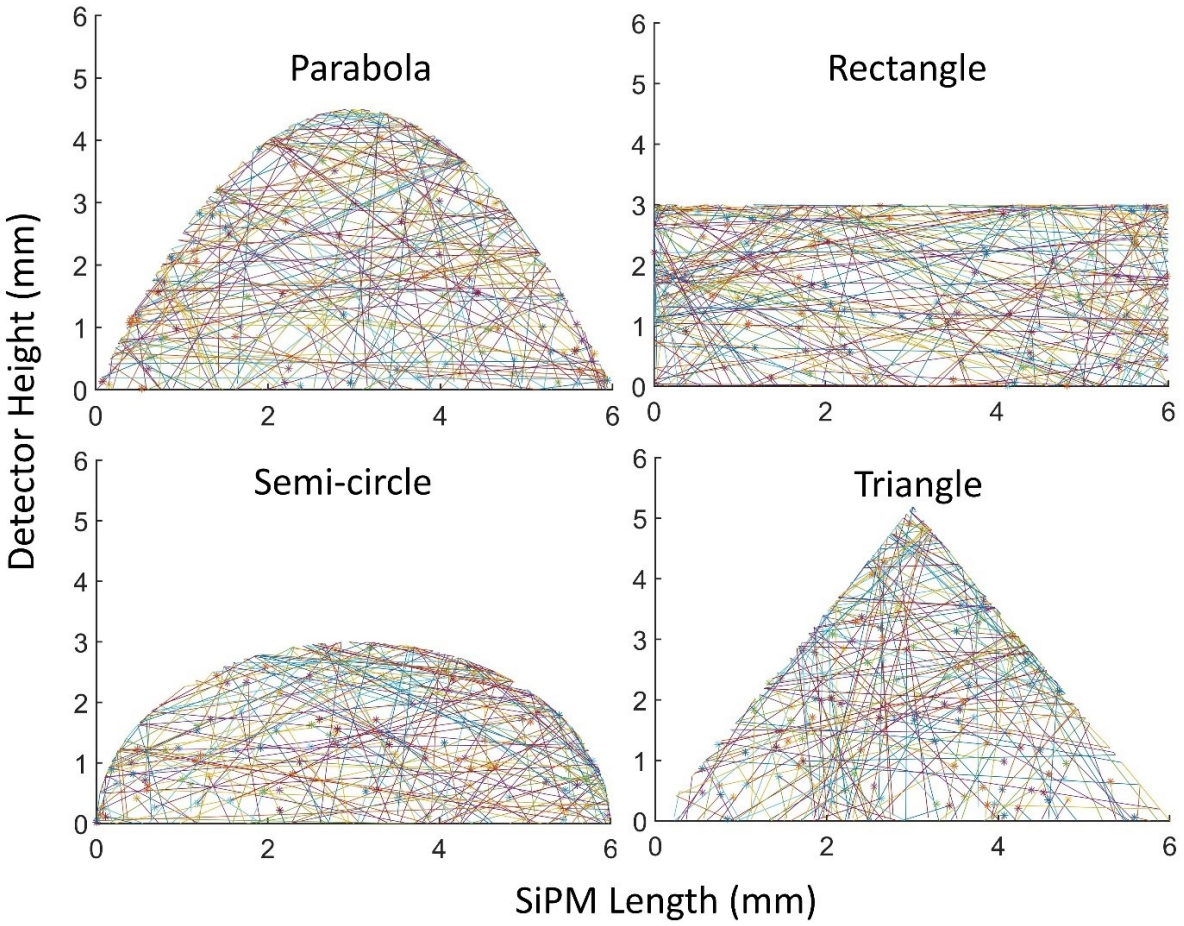

Figure 3-19. Ray tracing of optical photons in different geometries of PMMA with a Lambertian reflector, simulating only 100 photons for clear viewing. The photons are marked by a "*" while the scatters are traced by straight lines.

Optimization of Geometry

Shown in Figure 3-20 is the fraction of photons collected by the photosensor as compared to the total photons generated in the PMMA. The presence of a reflector, whether specular or diffuse, results in 7% greater fraction of photons intensity collected than without a reflector. For all geometries, a specular reflector results in only marginally better collection of photons than a Lambertian reflector. If the MLFD is wrapped in either type of reflector, the fraction of photons able to reach the photosensor is between 87% to 89.5% for different shapes. If the MLFD is not wrapped in a reflector, for different shapes, this fraction of photons reaching the photosensor is between 79% to 82%.

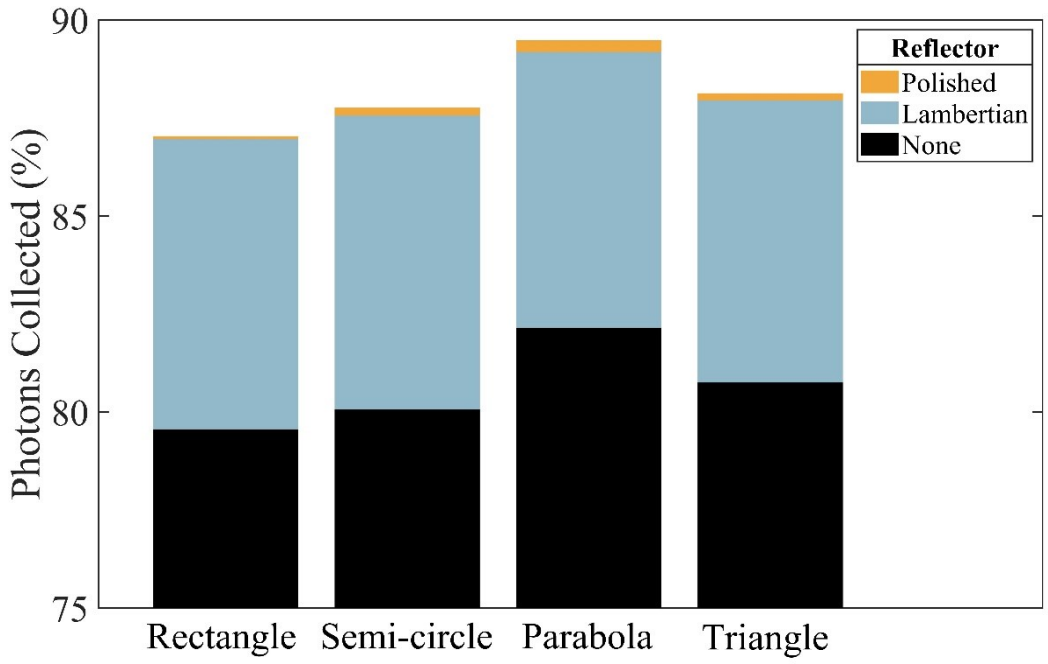

Figure 3-20. Simulated total photon intensity collected by the photosensor, expressed as a percentage of the initial total photon intensity at their origin, for four cross-sectional shapes.

The simulated results show that the parabolic shape results in the highest fraction of photons collected, and rectangle the least, with the difference being 2.22%. The fraction of photons collected is clearly impacted significantly by the presence of a reflector, however it is not significantly affected by either the type of reflector, or by the geometry. This is due to the small dimensions of the MLFD as compared to the photon attenuation coefficient in PMMA. It is important to note that additional non-geometric factors such as photocathode quantum efficiency and scintillator light yield also contribute to the final fraction of photons collected by the photodetector.

Chapter 4 - Fabrication and Instrumentation

4.1 Fabrication

MLFD fabrication is a 4-step process: preparing a mixture for the scintillation volume, stacking the layers, milling the MLFDs and assembling together milled pieces to form a larger length of detector, and finally wrapping the detector in Teflon tape on all faces except the one facing the light collection device.

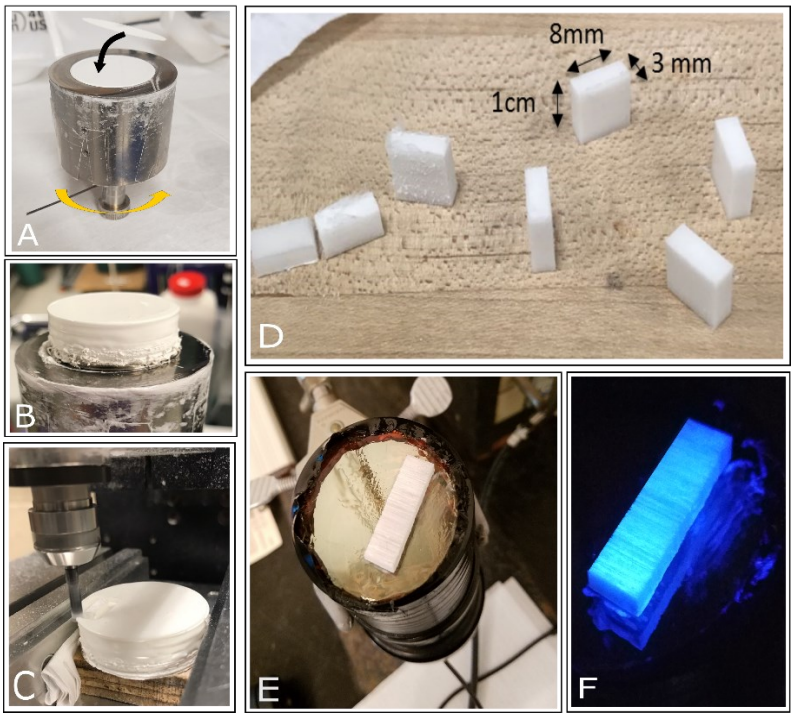

Figure 4-1. Process of fabricating the MLFD: (A) The piston arrangement helped achieve the ZnS:Ag micro-layers. The crank is turned in the direction shown by the solid black arrow while the yellow arrow represents stacking of alternating layers, (B) a 1-cm thick stack was composed of the alternating layers of PMMA and ZnS:Ag, (C) small rectangles were micro-milled out of the stack, (D) the pieces had very smooth edges, and any jagged ends can be smoothed, (E) the milled pieces were epoxied together to form a longer piece, shown here optically glued to a PMT photocathode window for testing, and (F) the same image under UV irradiation.

4.1.1 Preparing the scintillation volume

ZnS micro-particles doped with 0.01% by weight of Ag, obtained from Eljen Technology, was mixed with a two-part optically-transparent epoxy from Atom Adhesives. The ratio of epoxy resin to hardener to ZnS:Ag was 10:3:18. This ratio was determined by the recommended resin:

hardener ratio and by requiring to maximize the ZnS:Ag content. To maintain the same mass thickness of ZnS:Ag as present in 12 μm, the total layer thickness was increased to 35 μm, which included ZnS:Ag and the epoxy. The homogeneous mixture of ZnS:Ag and epoxy will hereupon be referred to as, simply, the ZnS:Ag layer, since the epoxy has no functional role in the detection process except to bind materials together.

4.1.2 Layer Stacking

Sheets of PMMA, obtained from Astra Products, were coated with the ZnS:Ag epoxy mixture and stacked alternatingly. To control the thickness of the ZnS, a polishing and levelling mount with a circular platform was used (Figure 4-2). As shown in Figure 4-2(b), a screw could be turned to vertically move the platform. A 360° protractor in degree markings was printed out and pasted on the back end of the level, and a handlebar was attached to the central screw, to indicate the angle of rotation. A vertical depth of 12 microns corresponded to 4.3° of rotation.

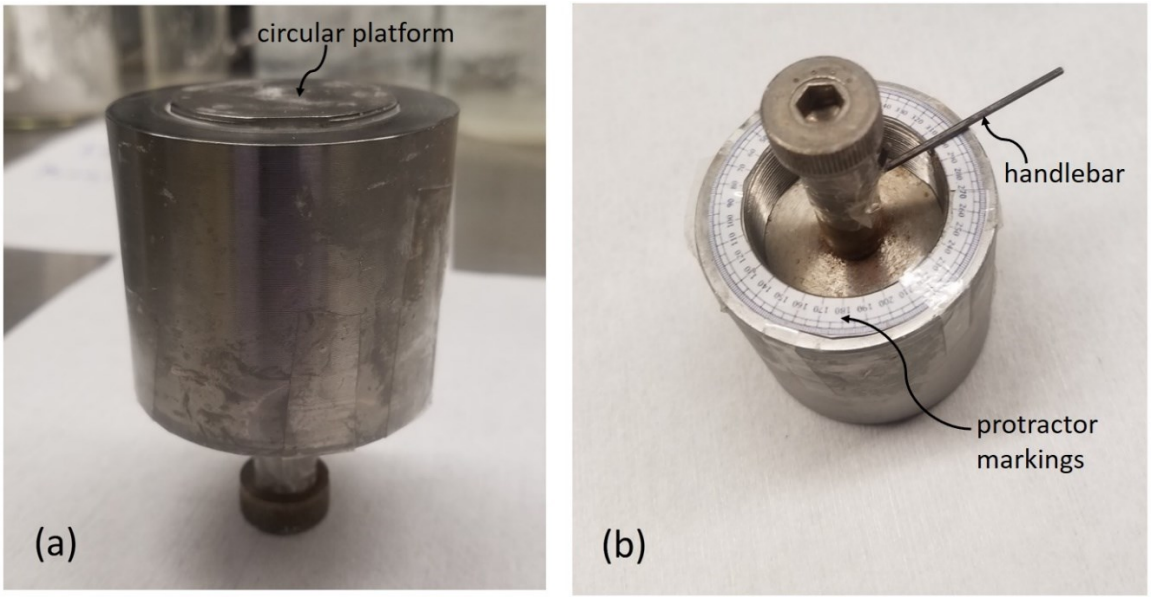

Figure 4-2. (a) Top and (b) back end of the polishing/levelling mount.

A ZnS:Ag layer-thickness of 35 μm was obtained by bringing the platform vertically downwards by turning the handlebar through 85°, which accounts for the 12.96° for the 35 μm layer, plus 72° for the 200 μm PMMA disk, as shown in Figure 4-1A. A second sheet of PMMA was then pasted over the ZnS:Ag layer, and lightly tapped to ensure no air bubbles were trapped in-between layers. This process was repeated until a stack of desired length was achieved, which

was then allowed to air-cure for 24 hours (Figure 4-1B). The stack used to be previously heat-cured as the process took only 1 hour, however, the heat (80°C) caused yellowing of the PMMA layers, reducing its optical transparency.

4.1.3 Micro-Milling and Assembly

Thereafter, a Minitech Machinery CNC micro-miller was used to cut small rectangles of cross-section 8 mm × 3 mm out of the stack (Figure 4-3). A square-ended, TiCN-coated, 4-flute, 1/8” mill diameter carbide end mill was used to cut the edges. A G-code was written to cut the pieces into the shapes required (Appendix-#1). Each 1-cm thick circular stack could produce about five individual rectangular pieces. These individual devices could be used either as one single detector (Figure 4-1D), or be epoxied together (Figure 4-1E) if longer lengths were required. Any rough edges were smoothed using sandpaper.

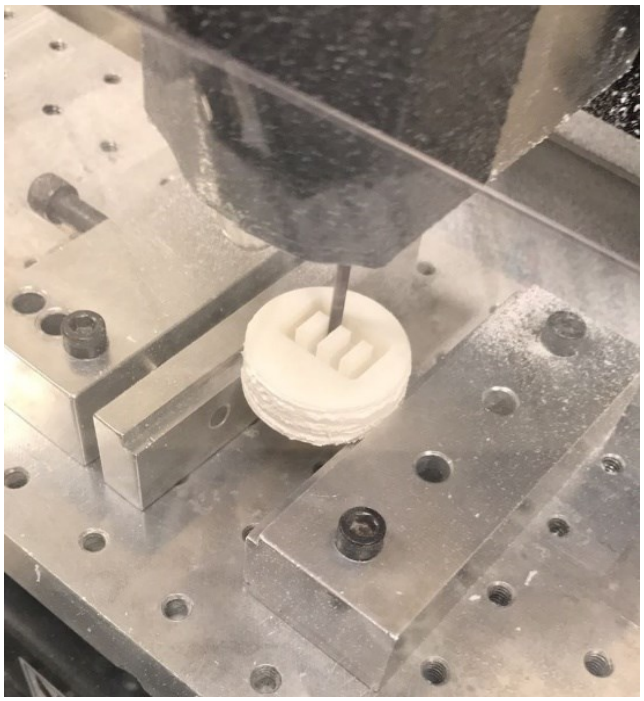

Figure 4-3. Small rectangles were cut out of the cured stack using a carbide end-mill.

4.1.4 Enclosing in Reflector

The MLFD is then wrapped in Teflon tape on all faces but one. Teflon tape is delicate, and must be wrapped carefully so as to not leave any air gaps between the detector the tape.

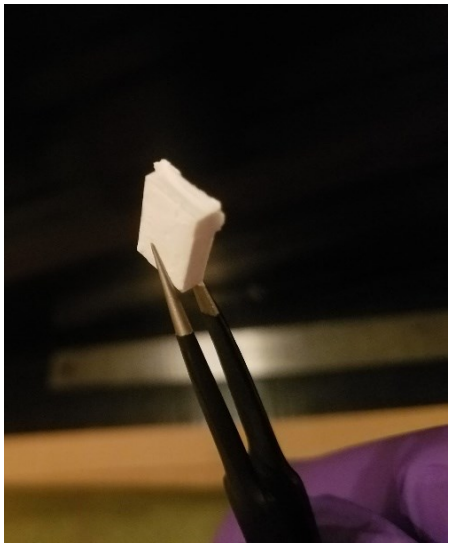

Figure 4-4. The Teflon tape must be wrapped carefully to not leave any air gaps or bumps.

4.2 Instrumentation

Simulation predictions and device engineering revealed the MLFD to have the most suitable design for a fast neutron detector in high gamma-ray backgrounds at TREAT. Instrumenting the device with the necessary electronics is a prerequisite to analyzing detector performance. The MLFD was coupled to a PMT for characterization and preliminary testing, and was thereafter coupled to a SiPM. Eventually, a prototype was built with an array of SiPMs.

4.2.1 Photomultiplier Tube

The MLFD was attached to the photocathode window of a bi-alkali Hamamatsu R6231 PMT using an optical couplant. The detector-source orientation was arranged in such a manner as to mimic the orientation at TREAT, with the exception of the PMT attached to the longest face of the MLFD rather than the end to facilitate greater photon collection from neutron events and lesser from Cerenkov radiation (Figure 4-5). The PMT was made of a borosilicate glass window. ^{10}B has a low cross-section for fast neutrons, but has a considerably high value for thermal neutrons (to produce 0.48 MeV gamma rays), which may result from interactions with shielding and other materials. Gamma rays also interact with the glass to produce Ĉerenkov radiation. The PMT window was 51 mm in diameter, so MLFDs longer than that would need larger PMTs, or SiPM arrays.

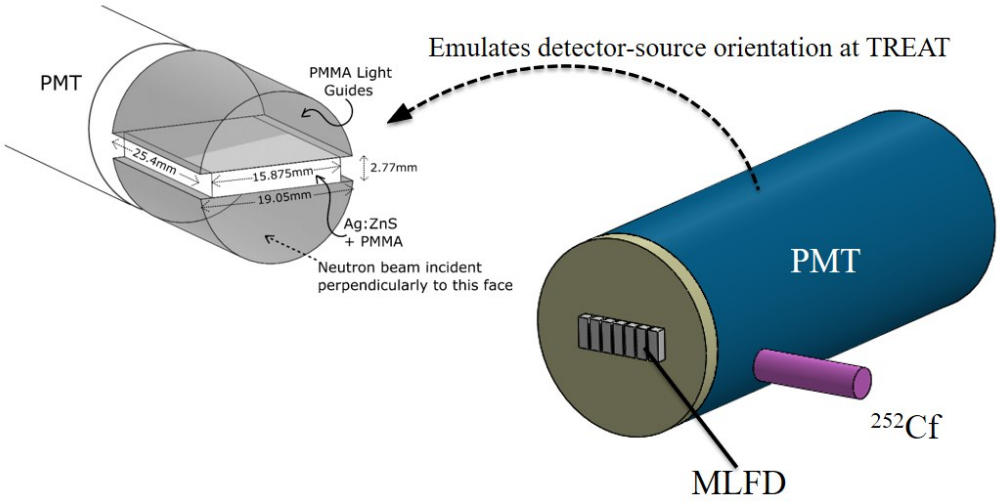

Figure 4-5. (a) The detector-source orientation in the experimental setup (left) imitated that of the Hornyak buttons' (right) in the TREAT hodoscope.

4.2.2 Silicon Photomultiplier

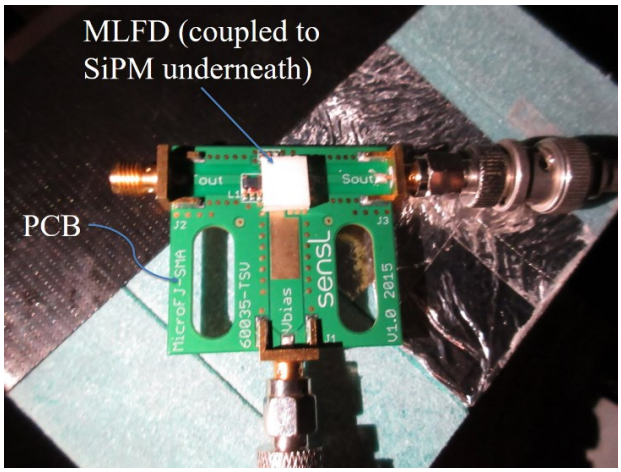

Figure 4-6. The MLFD was coupled to the SiPM (underneath the MLFD in figure) using optical grease.

For larger lengths of the MLFD, SiPMs were preferred. Also, SiPMs made the detection system more compact. A 10 mm-long MLFD was optically coupled to a 6 x 6 mm SenSL 60035 J-Series p-on-n SiPM mounted on a MicroFJ-SMA printed circuit board (PCB) that housed the sensor and the biasing circuitry, as shown in Figure 4-6. The Standard output (Sout) was read out to an oscilloscope, and the bias voltage was supplied via the Vbias. The SiPM had a breakdown voltage of 24.2 – 24.7 V, and was required to be operated between 1 – 6 V above the breakdown voltage. The SiPM had a high photodetection efficiency at the ZnS:Ag emission wavelength (450

nm) of 47%. A DC power supply capable of providing up to 30V and 15 mA was used to supply bias to the PCB (Figure 4-7). A coax-to-double-banana plug adapter was used for connecting a BNC cable to the power supply.

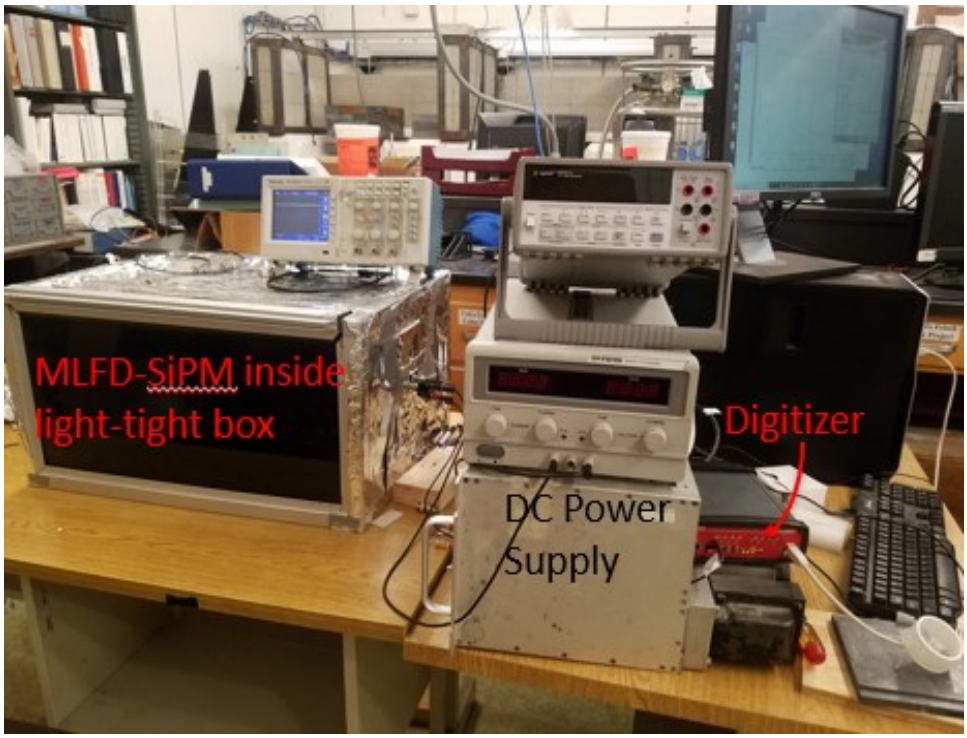

Figure 4-7. The MLFD-SiPM setup to extract waveforms exiting the SiPM-mounted PCB.

4.2.3 SiPM-array Imager

For SNM search applications, the MLFD was coupled to an array of four Broadcom SiPMs in a 2 × 2 square arrangement (Figure 4-8 and Figure 4-9). Four MLFD's were mounted on top of the SiPMs. Each sensor had an individual preamplifier and output. Depending on the relative count rates and the spectra from each sensor, the location of a neutron source can be located. An external power supply powered the board. The SMA outputs and are labeled by the channel corresponding to the sensor (Ch1 = sensor 1, etc.). The output was scaled to provide a 1 Volt signal for the nominal input signal. The monitor output for the SiPM bias was scaled 1:10; so a 3 VDC output is a 30 VDC SiPM bias. This output was intended to drive a light load and can be connected to a DMM. One switch was meant to turn on power to the board. A second switch turned on the SiPM bias. For layout and assembly purposes, the SiPM bias adjustment was placed on the bottom and is

accessible using a small screwdriver. The applied bias had a maximum at 33.9 V. The MLFDs were coupled to the SiPM arrays and covered with a light-tight black lid using anti-static tape.

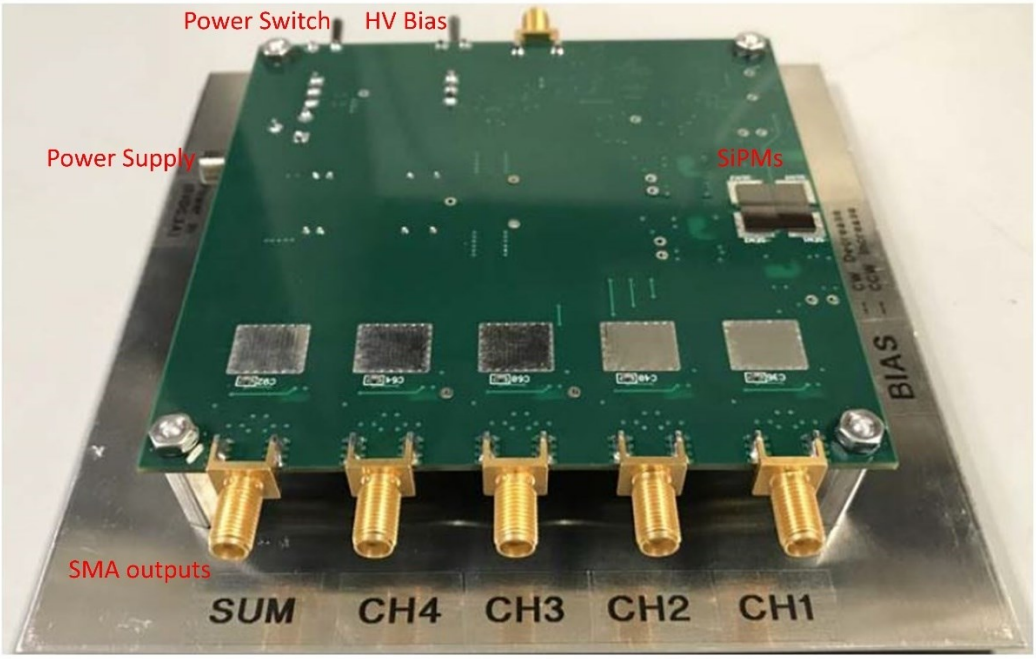

Figure 4-8. Printed Circuit Board housing the SiPM array and amplification circuitry.

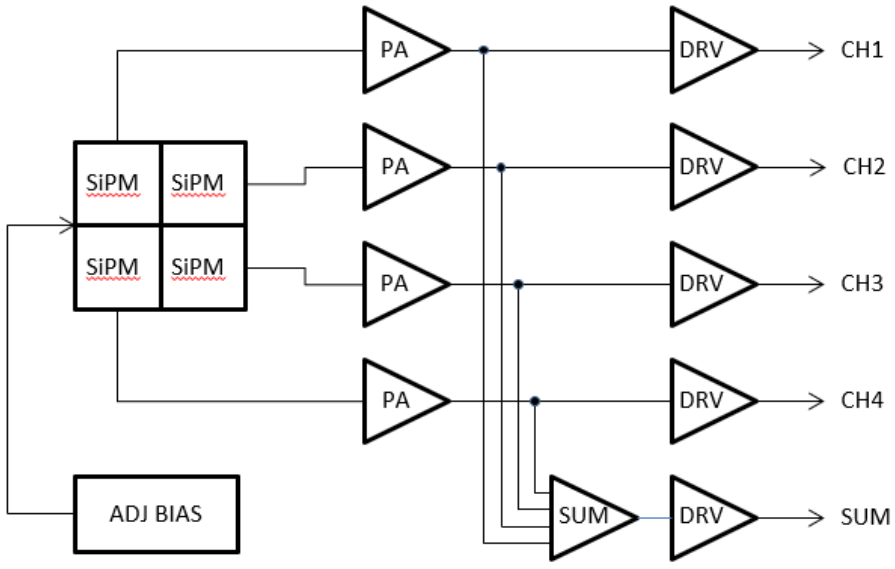

Figure 4-9. Schematic diagram of electronics in SiPM-array PCB

4.3 Alternative Designs, Techniques, and History of MLFD Fabrication

Before the aforementioned fabrication process was perfected, several techniques were employed to fabricate the MLFD. Listed in this section are these techniques, as well as several versions of a fast neutron detector that were theorized prior to the MLFD.

4.3.1 Chemical Bath Deposition

The use of epoxy to bind the ZnS:Ag to the PMMA layer and to hold together the whole MLFD introduced a foreign element to the detection system—one that is at best unnecessary and at worst detrimental to the detection process, and the Geant4 model excluded the epoxy in its model altogether. Thus, in order to avoid using an epoxy, it was attempted to deposit the thin ZnS film on PMMA sheets in a batch process, albeit individually, using chemical bath deposition (CBD). Additionally, CBD allows one to control the thickness of the film deposited depending on the concentration of the solutes in the solution [49].

A ZnS layer is grown on the PMMA substrate by the reaction between a zinc salt for the Zn^{2+} (zinc sulfate was used), thiourea for the S^{2-} ($SC(NH_2)_2$), and an ammonium salt (ammonium nitrate was used) as the complexing agent. The $ZnSO_4$ and $SC(NH_2)_2$ was added to a solution of deionized water in a tall testube sitting on a magnetic plate stirrer (Figure 4-10(a)). Ammonium nitrate was added slowly while stirring the mixture with the magnetic stirrer, at 120°C. First, the free Zn^{2+} is gained from the decomposition of the Zn-amine:

$$[Zn(NH_3)_n]^{2+} \leftrightarrow Zn^{2+} + nNH_3 \tag{4.1}$$

Then, thiourea produces S^{2-} ions by hydrolysis in alkaline medium:

$$SC(NH_2)_2 + OH^- \leftrightarrow SH^- + CN_2H_2 + H_2O \tag{4.2}$$

$$SH^- + OH^- \leftrightarrow S^{2-} + H_2O \tag{4.3}$$

Finally, the ZnS is grown on the PMMA substrate:

$$Zn^{2+} + S^{2-} \leftrightarrow ZnS \tag{4.4}$$

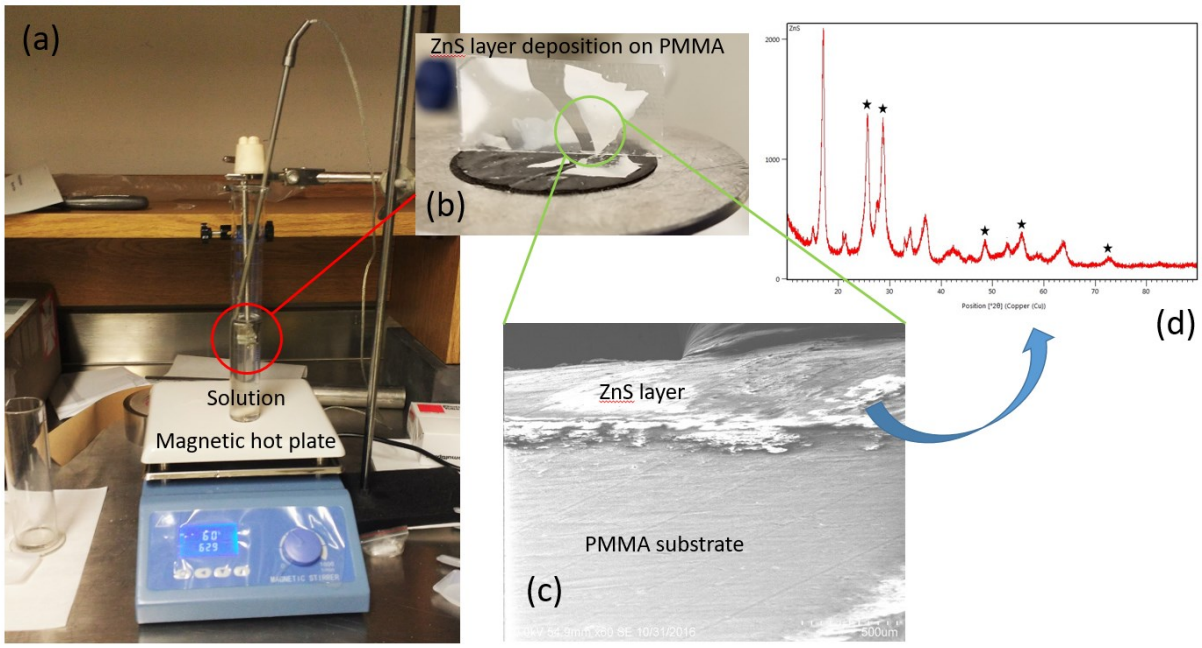

Figure 4-10. (a) Depositing ZnS layer on PMMA substrates using CBD, (b) the deposited ZnS layer, (c) SEM image of the deposited layer, and (d) XRD graph of the deposited layer content.

Images obtained from scanning electron microscopy (SEM) showed non-uniform deposition, and the layer itself was brittle and did not adhere well to the substrate (Figure 4-10(b) and (c)). XRD imaging showed that although ZnS was deposited, the layer still needed activation with dopant Ag. Further, additional lines were observed (Figure 4-10(d)) that were not attributed to ZnS, indicating deposition of other materials as well. For these reasons, this technique was abandoned.

4.3.2 Individual Layer Stacking Method

The polishing and leveling mount allowed one to control the layer thicknesses very precisely. However, prior to using that technique, an initial proof-of-concept was built by coating individual PMMA layers. In this method, a 20 µm thick tape was attached to the edges of a set of 8 × 3 mm PMMA slabs, and a paintbrush dipped in epoxy and ZnS:Ag was coated over the layers. A level squeegee was run over the coated layers to ensure uniform coating. The layers were left to cure, then carefully snapped off the set, and stacked with a thin layer of epoxy. A Teflon mold was

used to hold the epoxied layers into shape while it cured. SEM images (Figure 4-11) showed that the layer thicknesses were quite non-uniform, not only between layers but within the same slab of PMMA as well, and required a large amount of epoxy. Thus, this method of fabrication was abandoned.

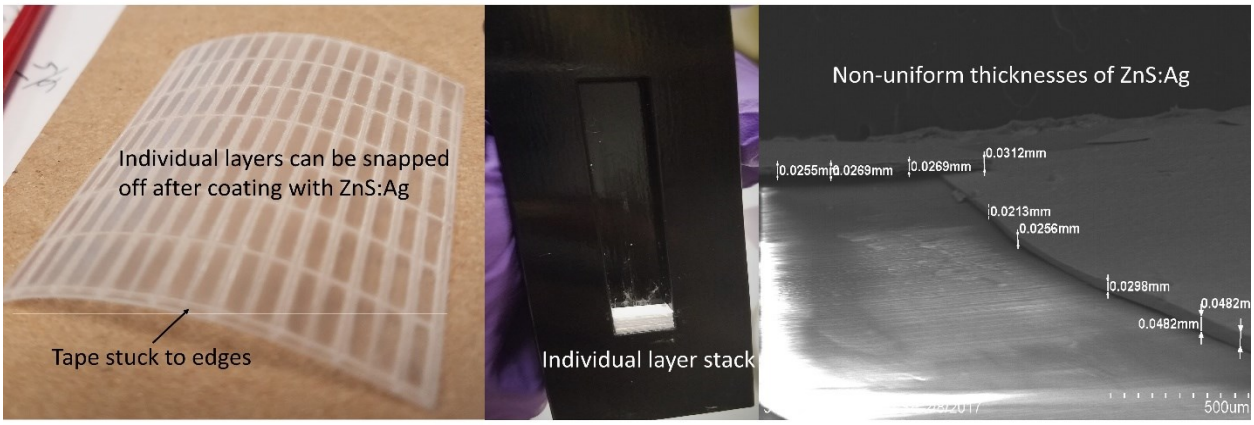

Figure 4-11. Individual 200-µm thick PMMA strips were bought and taped at the edges to provide a benchmark of ZnS:Ag layer thickness. The cured layers were then snapped off and epoxied to create a stack. The thickness of the ZnS:Ag layer was non-uniform.

4.3.3 First MLFD Prototype

The first MLFD prototype was built with steps similar in ideal to the present version, but with lesser precision tools. A large square PMMA disk of 200 µm thickness was taped at the edges with regular 35 µm thick tape. The tape guided the ZnS:Ag layer thickness, which, along with epoxy, was coated on the disk. A flat wiper ensured uniform thickness. A second layer of PMMA disk was then stacked on top of the first layer. The process was repeated till a stack of desired length was obtained. A band saw was used to cut out rectangles out of the cured stack. Smaller rectangular stacks would then be epoxied to form a larger MLFD. This version of the MLFD suffered from using epoxy that yellowed within weeks, rough and jagged edges, non-uniform lengths from sawing, and large air bubbles in the ZnS:Ag layers (Figure 4-12).

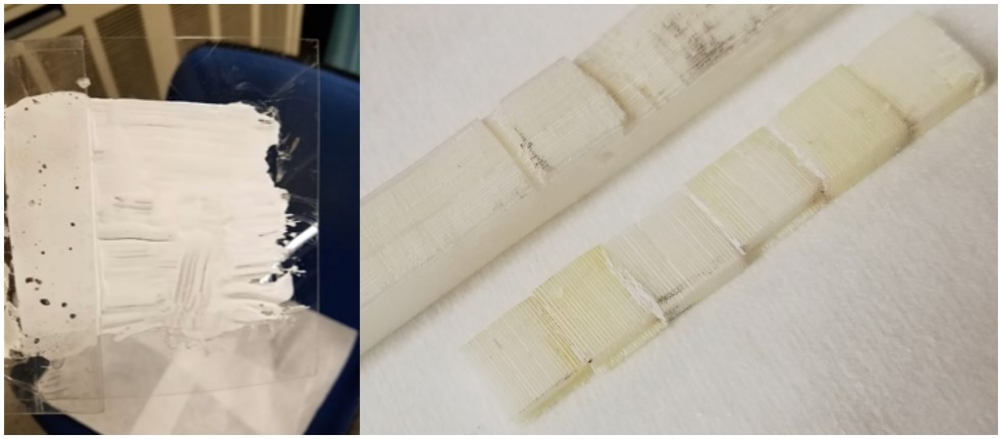

Figure 4-12. Large PMMA disks were coated in ZnS:Ag and stacked (left). The first MLFD prototype (right).

4.3.4 Homogenized Fast Neutron Detector

A variant of the Hornyak button was devised, which was a mixture of PMMA and ZnS:Ag, and had the same dimensions as the MLFD [50]. Unlike the Hornyak button, however, the homogenized detector did not have any half-circle light guides, with the light collection device oriented in a similar fashion to the MLFD. To fabricate the detector, liquid PMMA monomer and ZnS:Ag phosphor (12% by weight) was mixed together and air-cured fully in 7 days (Figure 4-13).

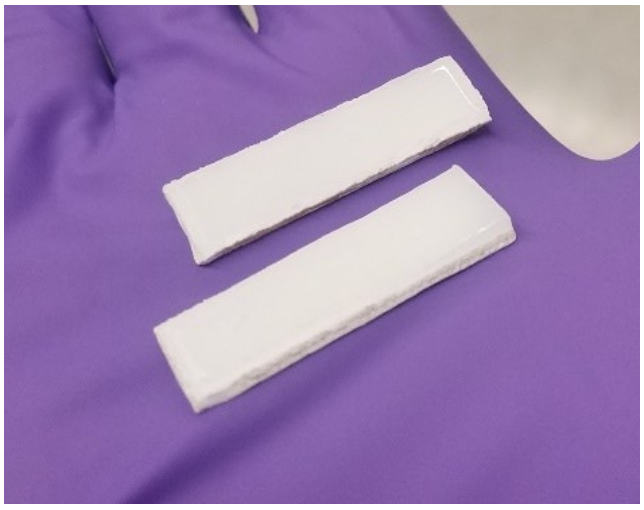

Figure 4-13. The homogenized detector is a variant of the Hornyak button without the light guides.

Simulations in Geant4 showed that a ZnS:Ag mass fraction of 12% in PMMA would exhibit the highest efficiency. The ZnS:Ag molecules were randomly distributed in the PMMA mass, hence the forward-directional protons have lesser probability of depositing energy in the

scintillator than in the layered configuration. However, this lessened probability is beneficial for and may contribute to improved gamma-ray rejection [26]. The neutron detection efficiency of a 5 cm-long homogenized detector was predicted in Geant4 to be 1.3%; about thrice less than that of a 5 cm MLFD. Although the homogenized detector exhibited better performance at very high gamma-ray fluxes (Figure 4-14), the use of PSD and SiPMs (as will be show in later chapters) would allow the MLFD to perform superior to the homogenized detector. Hence, this detector was discontinued.

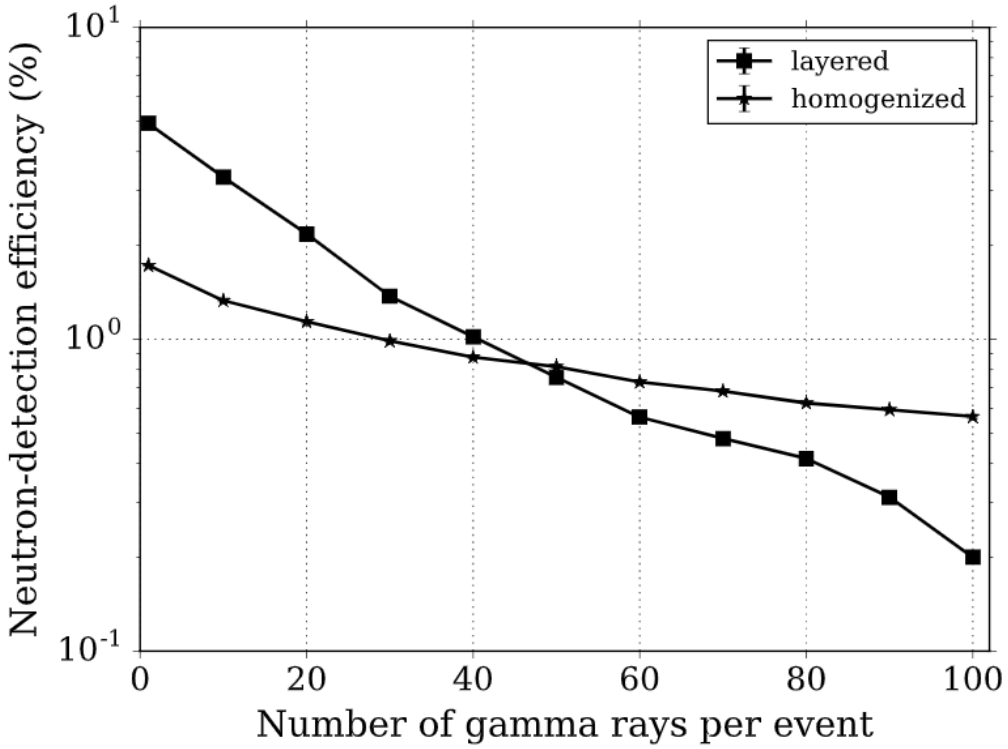

Figure 4-14. Detector performance at different gamma-ray fluxes. 'Event' is equivalent to a neutron in this plot. reproduced with permission from Elsevier [26].

4.3.5 Uranyl Nitrate Back-Filled Micro-Structured Semiconductor Neutron Detectors

Micro-Structured Semiconductor Neutron Detector (MSND) consist of a matrix of micro-structured trenched Si wafers backfilled with neutron-reactive material like ^{6}LiF for thermal neutron detection [51]. MSNDs boast a high thermal neutron detection efficiency due to the large (n,t) cross section of ^{6}Li and clever geometry optimization. It was therefore proposed to evaluate

the MSNDs for fast-neutron detection at TREAT using two approaches: (1) using a hydrogenous material to thermalize the fast neutrons to exploit the high intrinsic efficiency of MSNDs, and (2) substituting the ^{6}Li with a fast-sensitive reactant, such as ^{235}U.

Approach 1: Thermalization

A simple, 7- channel mock-up was designed to represent a portion of a hodoscope, shown in Figure 4-15. A single MSND was modeled in each of the detector channels surrounded by high-density polyethylene (HDPE). The green region was composed of 5% borated polyethylene (BPE). Both HDPE and BPE are efficient at moderating fast neutrons. In addition, the boron content in BPE is a good thermal-neutron absorber, thereby preventing prevent cross-talk, i.e., neutrons entering the target channel entering other channels and being detected. It was necessary to minimize such cross-talk between the hodoscope channels to provide accurate, spatial mapping of fuel motion [52].

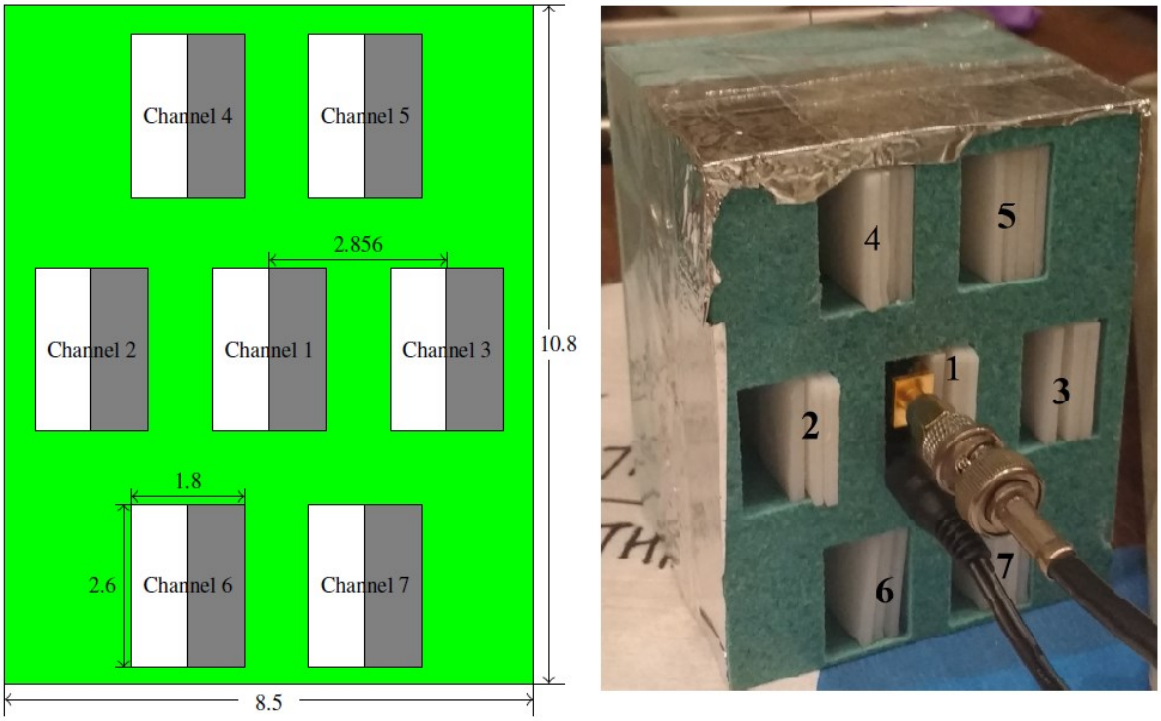

Figure 4-15. (a) MCNP model of the hodoscope mock-up. White regions denote the detector channels filled with HDPE, green regions represent 5% BPE, and gray regions are the MSNDs. Channel 1 is the target channel with the source located it its center. All values are in cm. (b) Experimental setup wherein a single MSND was inserted into each channel one at a time to measure the corresponding count rate.

A model was written in MCNP to estimate the detection efficiency in the mockup, when a sequence of MSNDs was placed into the target channel. A mono-directional ^{235}U thermal fission spectrum was used as the source. The detection efficiency was observed to saturate at about 0.8% when more than 7 MSNDs were used. To evaluate cross-talk quantitatively, the cross-talk ratio (*CTR*) was defined as:

$$CTR = \frac{Number\ of\ counts\ in\ neighbor\ channel}{Number\ of\ counts\ in\ target\ channel} \tag{4.5}$$

To validate the computational results, count rates at different channels from neutrons emitted from a ^{252}Cf source, which was placed at the center of channel 1, were recorded. The experimental results, as listed in Table 4-1, confirmed the existence of significant cross-talk, with the measured cross-talk (all over 60%) being substantially larger than the MCNP model predictions by 10-30% in each channel. A large portion of this difference could be due to neutron scattering not included in the model. Specifically, the walls, floor, ceiling, equipment, and table on which the mock-up was situated, along with any other, nearby hydrogenous objects may have caused neutron-scattering and lead to a higher count rate. However, because both the predicted and measured results were underwhelming, no further work was performed to reduce the discrepancies.

Table 4-1. Measured and Predicted CTRs in different channels. Channel 1 is the target channel [52].

Channel Number	1	2	3	4	5	6	7
Measured net count rate (counts/min)	185.7± 4.31	128.95± 3.58	114.75± 3.37	113.65± 3.37	114.5± 3.38	114.5± 3.38	115.15± 3.39
Measured CTR	-	69.44%	69.11%	61.79%	61.2%	61.66%	62.01%
Predicted CTR	-	50.12%	70.8%	34.95%	50.47%	36.22%	53.4%

Approach 2: Fast-Sensitive Reactants

Uranium was precipitated from a uranyl nitrate solution based on a previously-formulated recipe at KSU [53]. The original particles from the uranyl nitrate precipitate had widths ranging

from 30-160 μm. An attempt was made to reduce the particle size to fit inside the 20-μm trenches using homogeneous precipitation from solution by hydrolysis of urea at elevated temperatures. Such precipitation yielded novel, ammonia-intercalated alphatype hydroxide phases and exhibited a much milder concentration gradient than mechanically adding NH_4OH, resulting in precipitation products of higher purity, smaller particles, and less agglomeration. Homogeneous precipitation of uranyl nitrate was carried out in a pressure cooker at 120°C for 30 minutes. Significant reduction in particle width was observed, with widths of 6-17 μm (Figure 4-16).

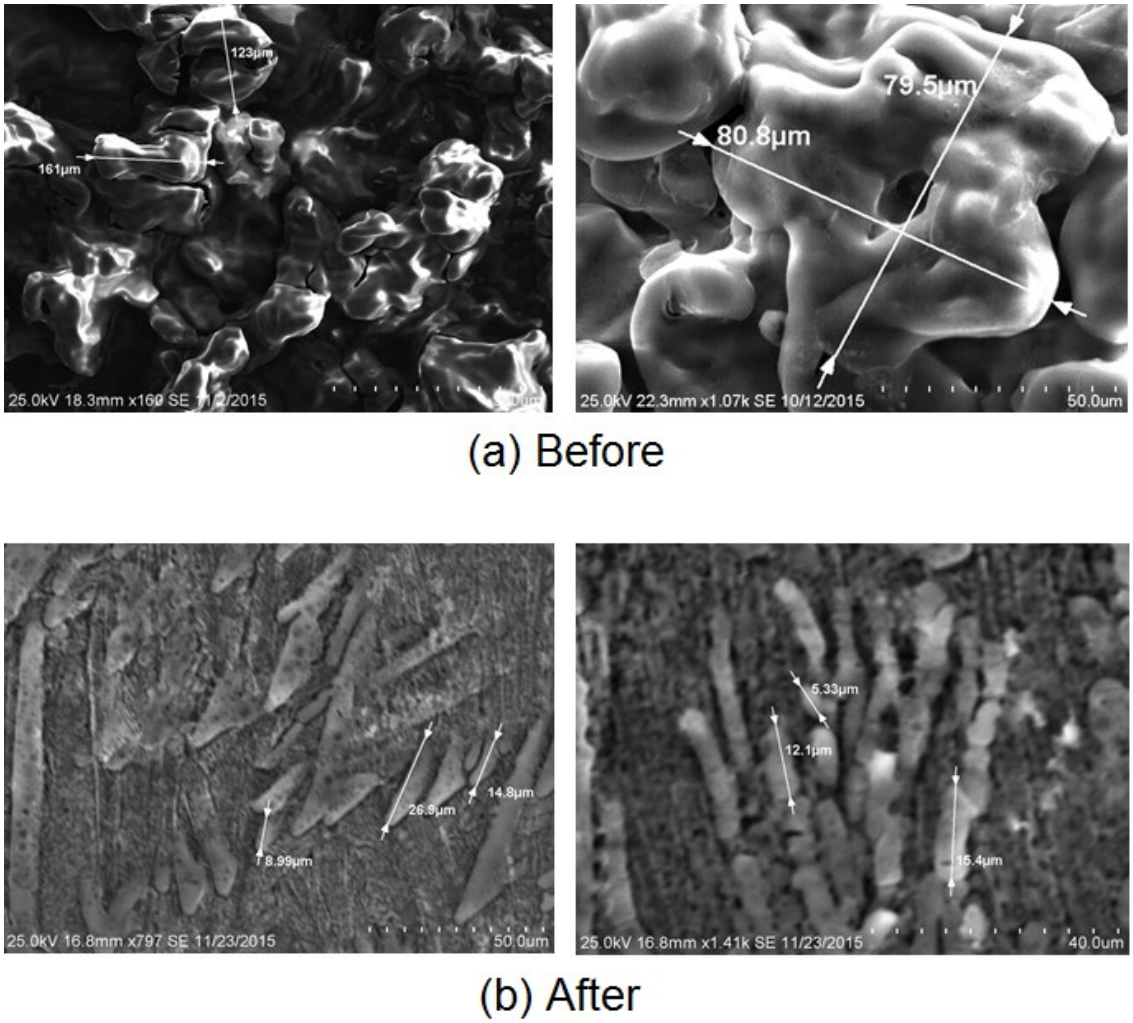

Figure 4-16. (a) Before and (b) after homogeneously precipitating uranyl nitrate.

The MSND was fixed in place to the bottom of a centrifuge tube and the solution was poured over it. The tube was centrifuged for an hour. Scanning Electron Microscopy (SEM) imaging showed that the accumulation of the particles at the entrance caused the major portion of

the trenches to remain empty, as shown in Figure 4-17. The few particles that were able to enter the trench agglomerated together into bigger clumps at the bottom of the column. X-ray fluorescence analysis indicated that a negligible amount of uranium entered the trenches (Figure 4-18), which suggests that uranyl nitrate is unsuitable for this application. Due to the several engineering challenges, the focus eventually shifted to designing a new type of fast neutron detector.

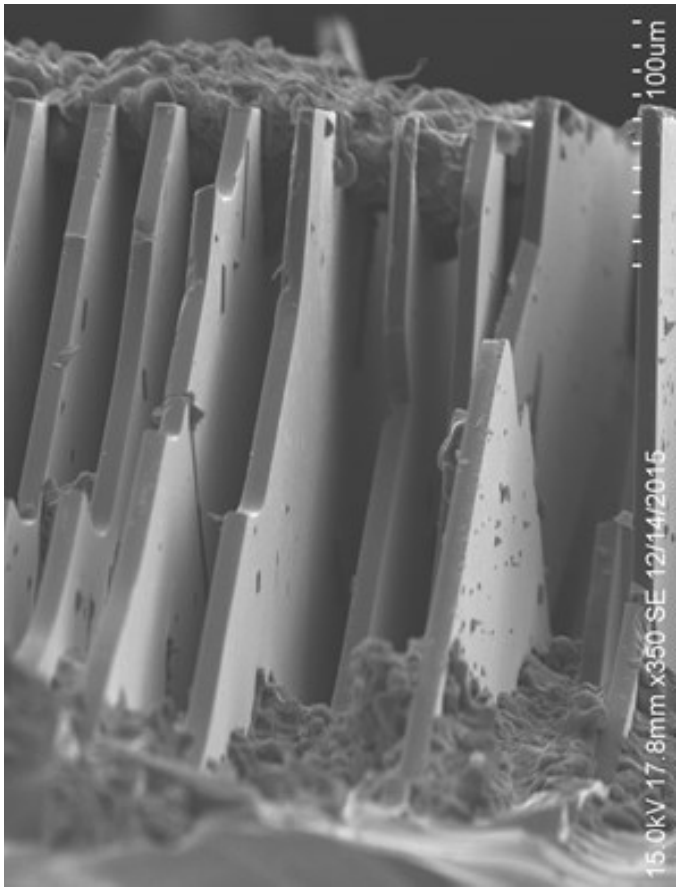

Figure 4-17. SEM image of the under-filled MSND trenches [52].

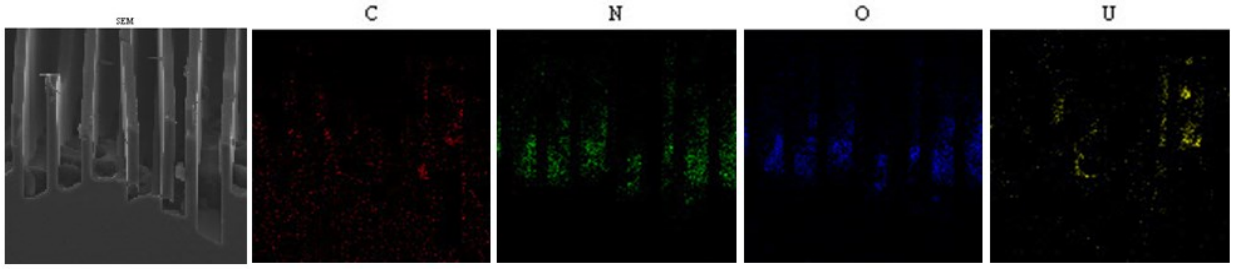

Figure 4-18. X-Ray fluorescence of the trenches after homogeneous precipitation of uranyl nitrate.

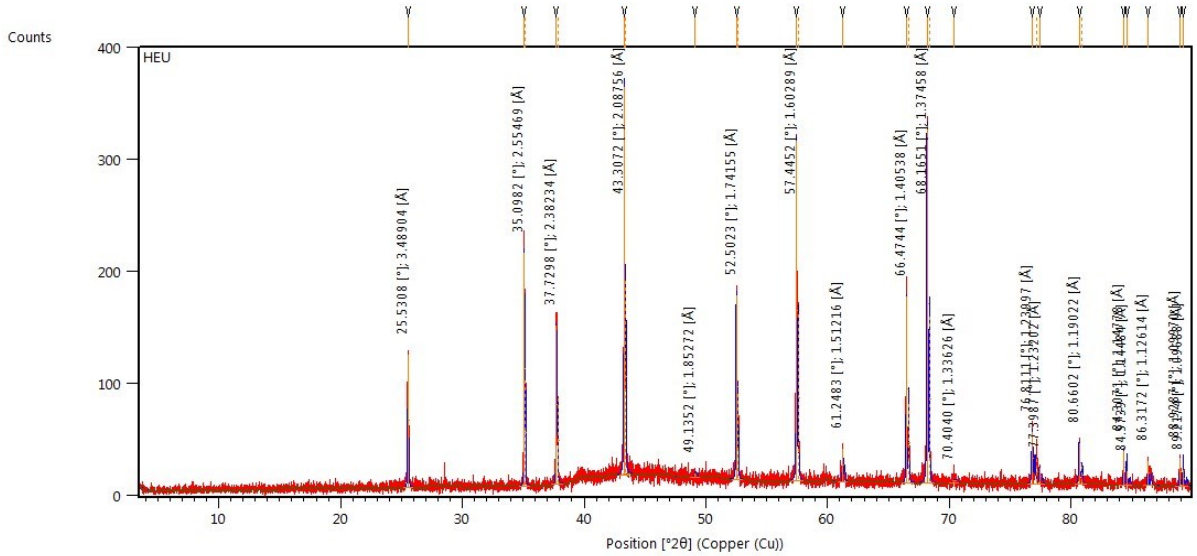

Figure 4-19. X-ray diffraction pattern of the homogeneously-precipitated hydroxide phases of uranium.

After thorough consideration from theoretical simulations of detector performance results and ease of manufacturing, it was decided that the MLFD was the most promising candidate for both fuel motion imaging as well as active interrogation. Hence, the remaining chapters are focused on the performance and characteristics of the MLFD.

Chapter 5 - Characterization

This chapter explores the physical and chemical characteristics of the materials that constitute the scintillator that reflect their desirable detection properties, and the pulse characteristics that decide the timing properties of the scintillator.

5.1 Physical Characteristics

Optical and scanning electron microscopy (SEM) with a Hitachi S-3400N SEM was used to characterize the thicknesses and surface features of the PMMA sheets and ZnS:Ag layers. Surface profilometry was used to study surface morphology and roughness using a diamond-tipped L stylus of a Dektak 150 Profilometer with a resolution of 0.139 μm.

5.1.1 Layer Profile

SEM imaging showed that the ZnS:Ag + epoxy layer thicknesses had an average value of 35 μm with a 22.8% standard deviation measured over 106 layers in a 25.4-mm MLFD, while the PMMA sheets had a 20% tolerance about 200 μm. The darker areas on the 10-mm long device shown in Figure 5-1(a) formed as a result of contrast-dependence due to local sample charging from secondary electrons, and are not indicative of any surface anomaly.

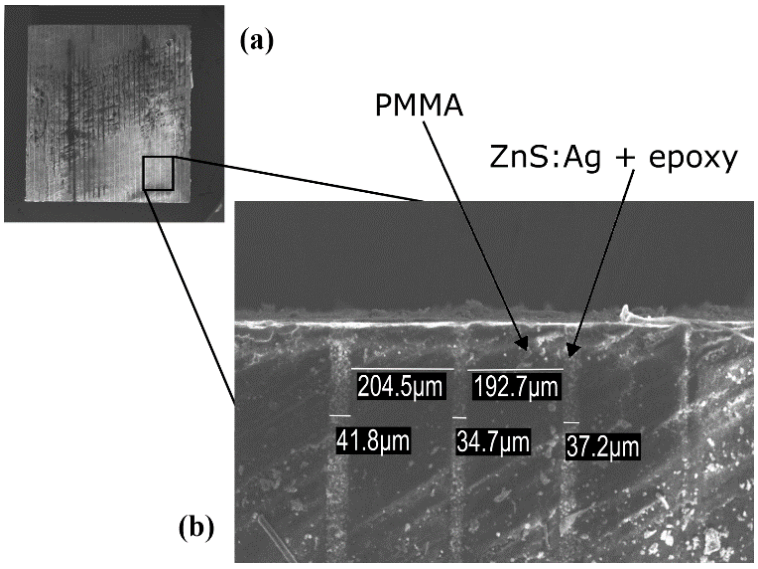

Figure 5-1. SEM images of (a) a 1 cm-long MLFD, and (b) a magnified portion of the detector showing the individual ZnS:Ag layers [54]. reproduced with permission from Elsevier.

5.1.2 Surface Profile

A Dektak Profilometer with a diamond-tipped stylus was used to gauge the surface features produced by micro-milling the MLFD. The surface roughness over a 25.4 mm MLFD had a standard deviation of 3.2 μm (Figure 5-2). Microscopy and surface profilometry indicated that the fabrication process and micro-milling yields ZnS:Ag layers of consistent thickness and optically smooth edges, respectively. The detector had a smooth surface to reduce surface scattering, and thus optical transmission can be assumed to be well described by Snell's law.

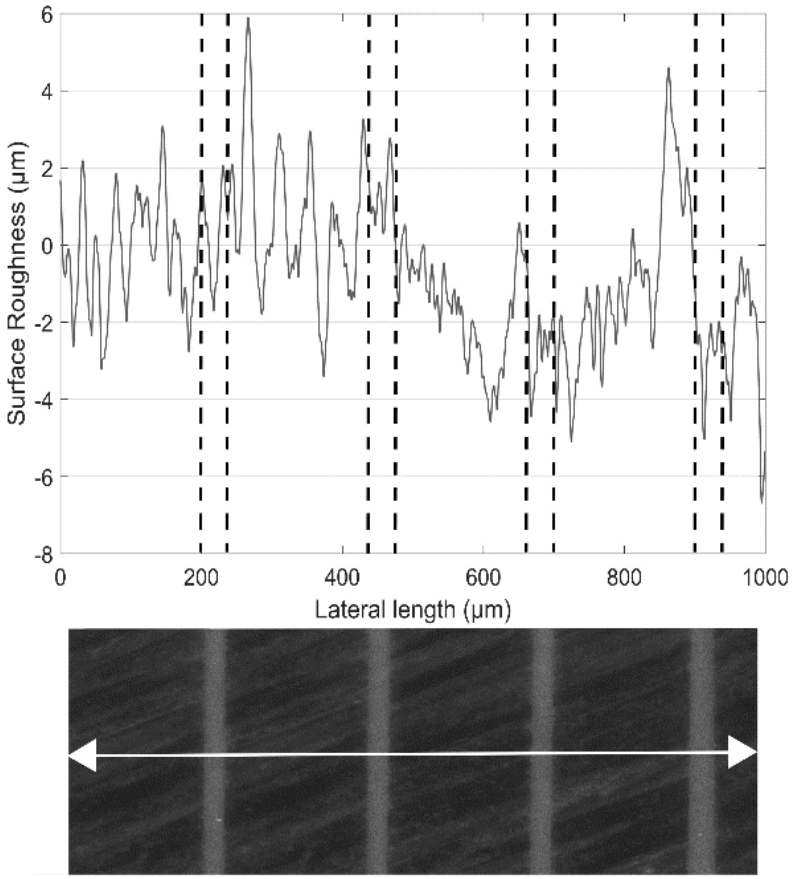

Figure 5-2. Surface morphology over a 1000 μm long line (top) sampled on a 25.4-mm long MLFD. The bottom image (obtained using optical microscopy) shows the line scanned by the profilometer stylus. Reproduced with permission from Elsevier [54].

Light Collection Efficiency

The surface roughness warranted an investigation into the LCE of the MLFD-PMT system, as the edges of each layer might contribute to light attenuation. To calculate the LCE, equation

(2.11) dictates that the charge collected on the anode must be found. To that end, the MLFD-PMT system was connected directly to the digitizer to collect charge pulses. The system was irradiated with monoenergetic 14 MeV neutrons from a D-T generator.

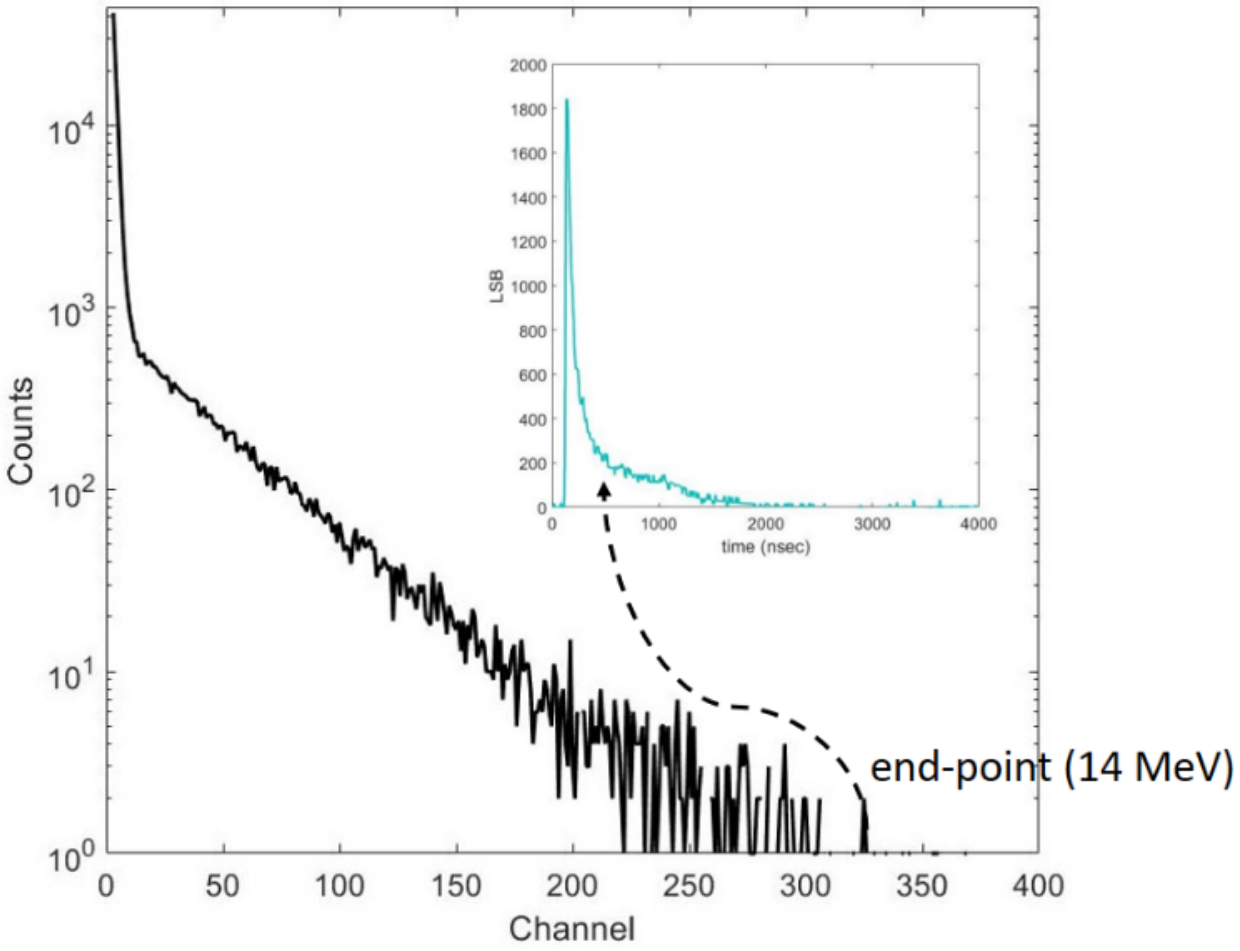

Figure 5-3. Pulse height spectrum of the the MLFD when irradaiated with 14 MeV neutrons. The inset shows the averaged largest pulse at the end point. 1 LSB = 0.03 mV.

As discussed in section 2.2.6, a proton-recoil detector produces a spectrum of energies from zero to the maximum energy of the source. For a monoenergetic 14 MeV source, the 'end point' of the spectrum would be 14 MeV (Figure 5-3). Therefore, the largest pulses collected were considered to be about 14 MeV. Ten of the largest pulses were averaged, and the charge under the averages pulse amounted to 1.71×10^{-9} C (charge sensitivity = 5 fC/LSB), corresponding to 14 MeV. As per simulations, 37 optical photons per keV were produced [26], hence, 14 MeV would

produce 37 × 14,000 = 518,000 photons. The quantum efficiency of the Hamamatsu R6231 PMT used was 26% at 450 nm, and the gain at 1000V was 2.7×10^5. Using these values in equation (2.11):

$$1.71 \times 10^{-9} = 518000 \cdot LCE \cdot 0.26 \cdot 2.7 \times 10^5 \cdot 1.6 \times 10^{-19} \quad (5.1)$$

$$=> LCE = 0.29 \quad (5.2)$$

Thus, the light collection efficiency of the MLFD-PMT system is 29%. Detectors have shown to reach LCE of about 60%, by changing detector geometry [55]. Although a number of assumptions were made to arrive at this value, it can be improved by polishing the surface of the MLFD further and to use the optimized geometry where applicable.

5.2 Chemical Characteristics

A radioluminescent spectrophotometer was used to irradiate the MLFD with x rays and the resulting spectra was recorded for luminescent studies of doped and undoped ZnS.

5.2.1 Photoluminescence

Shown in Figure 5-4 is the photoluminescence (PL) spectra of ZnS doped with 0.01% by weight Ag. The ZnS:Ag microparticles fluoresced approximately four times as intensely as pure ZnS at a wavelength of 450 nm. Both the un-doped and doped spectra exhibited a peak at about 450 nm, although the latter exhibited a sharper peak. Both the un-doped and doped peaks were asymmetric. There is a steeper rise on the higher-energy (lower wavelength) side than on the lower-energy (higher wavelength) side. The asymmetry could be attributed to valence band-tail recombination which develops due to fluctuations of charged defects.

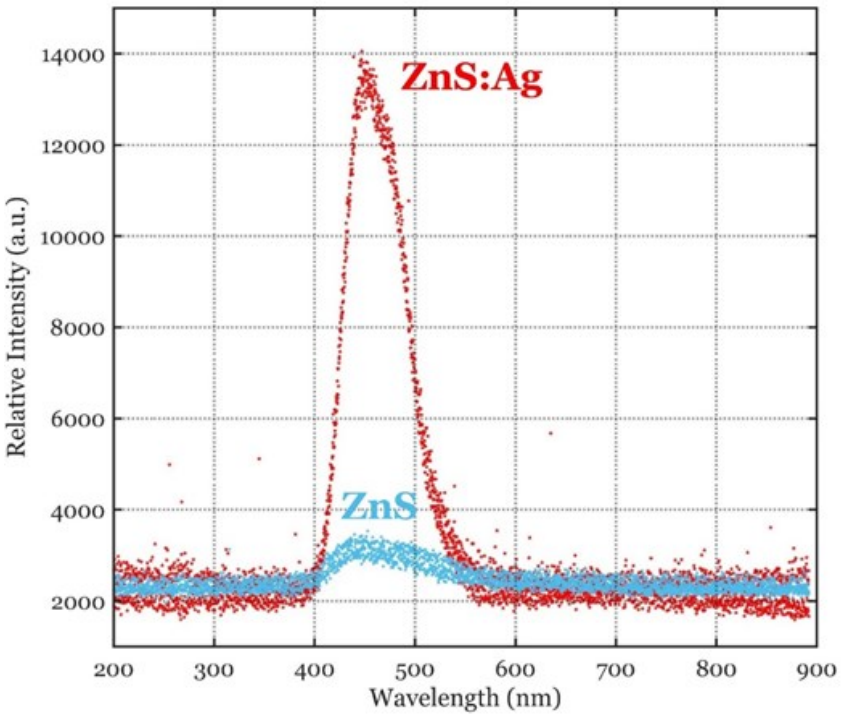

Figure 5-4. PL spectra of doped and un-doped ZnS phosphor.

5.3 Pulse Characteristics

For accurate identification of neutrons in a high gamma-ray flux, it was desirable for the detector to have a fast scintillation response to avoid pulse-pile up, and the ability to discriminate between neutrons and gamma-rays. Therefore, the following section investigates the MLFD for the aforementioned characteristics.

5.3.1 Decay Modes

As stated by equation (2.13), scintillation pulses can be characterized by the fast and slow decay components. While the fast component usually dominates, both components can be a function of the differential energy loss. When the energy loss dependence is strong on the time components, the overall decay time becomes dependent on the type of incident particle [56]. Such scintillators enable pulse-shape discrimination. The basis of PSD lies in the fact that heavy charged particles like protons cause higher ionization and excitation density than fast electrons in the scintillator, which results in different decay times, modes and their intensity. For ZnS:Ag, heavy particle excitation has previously resulted in scintillation light pulses with a fast decay component

of 70 ns with a light yield contribution of 85%, an intermediate component of 900 ns with 13% contribution, and a slow decay component of 10,000 ns with a 2% contribution [57]. Electron excitation of ZnS:Ag, on the other hand, has been observed to exhibit a much different fast decay component of 10 ns [58]. The fast component is considered to be an exponential decay relating to a mono-molecular process, the intermediate component may either be exponential, or a quadratic-hyperbolic decay relating to a bimolecular electron-hole recombination process, while the slow component corresponds to the thermal release of electrons from traps into the conduction band [32]. The difference in decay times for heavy particle and electron excitation makes for a strong case to explore the decay characteristics of the MLFD, as gamma-ray separation is an important prerogative in this endeavor.

5.3.2 Decay Times

The MLFD connected to a PMT was irradiated with a ^{252}Cf, and an algorithm was developed in MATLAB (05) to collect pulses from the DPP-PSD software, and according to the long and short gates, sorted the pulses into neutron (proton)-induced and gamma-ray (electron) induced pulses (Chapter 6 will discuss at length about the experimental setup required to gather this data). 100- and 1000-pulse averages were taken for neutrons and gamma rays respectively, but the high number of particles incident upon the detector produced extremely large data files, making it difficult to collect a greater number of pulses for averaging. The average neutron-induced pulse, $N_n(t)$, as shown in Figure 5-5(a), was fitted by a tri-exponential fitting function:

$$N_n(t) = 0.0754e^{-\frac{t}{9920}} + 0.1704e^{-\frac{t}{702.66}} + 0.754e^{-\frac{t}{76.37}} \tag{5.3}$$

A tri-exponential function had the highest R^2 value. Additionally, literature values have mentioned the existence of a tri-exponential decay as described in Chapter 5. Thus, neutron-induced scintillation pulses show 3 exponential decay times: a fast component of 76.37 ns with a light yield contribution of 75.4%, an intermediate component of 702.66 ns with a contribution of 17.04%, and a slow component of 9920 ns with a contribution of 7.54%. Gamma-induced pulses from ^{252}Cf show one exponential component of 12.03 ns (Figure 5-5(b)), represented by the following equation:

$$N_\gamma(t) = 1.096e^{-\frac{t}{12.03}} \tag{5.4}$$

Pulses from Ĉerenkov radiation exhibited a similar exponential decay component to that of gamma rays, of 12.93 ns. Both the neutron and photon decay times agree with values from the literature [32], assuming proton and alpha-particle (both heavy ions) excitation in ZnS:Ag phosphors share similar decay characteristics. The difference in decay times is evident in Figure 5-5, where the neutron-induced pulse has a considerably longer tail than the photon-induced pulse. The large difference in decay times of neutron and photon-induced pulses indicated that the MLFD would be capable of discriminating between neutron and gamma rays easily.

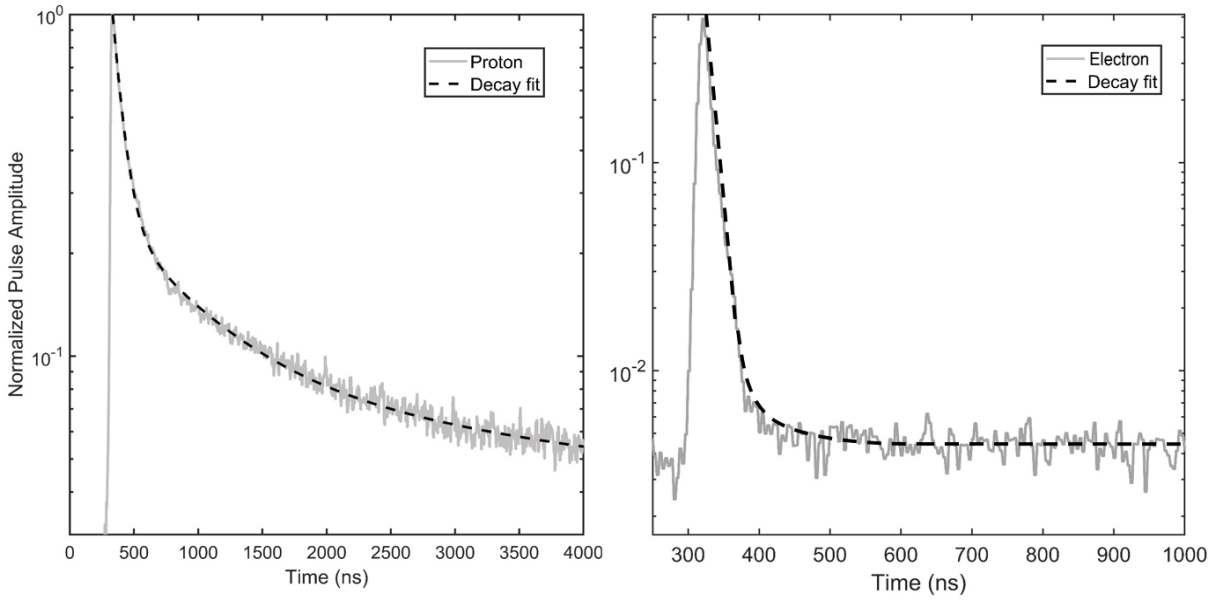

Figure 5-5. Pulse averages for (a) neutron-induced pulse (left), and (b) gamma-ray induced pulse (right). An exponential curve was used to fit the decay component of the pulses. Reproduced with permission from Elsevier [66].

Chapter 6 - Performance Analysis

Once the MLFD was instrumented and characterized, it was set to be tested for performance. To quantify performance, the detection efficiency and the gamma-ray rejection capabilities were determined. Pulse-shape discrimination was then performed to confirm the accuracy of the efficiency and gamma-ray rejection values.

6.1 Detection Efficiency

A 25.4 mm MLFD (Figure 6-1) and a 25.4 mm Hornyak button (Figure 6-2) were separately attached to the Hamamatsu PMT using optical grease. The MLFDs were irradiated with (a) ^{137}Cs (4.5Ci) for background gamma-ray rejection and determination of the discriminator bias threshold, and (b) with an unshielded isotropic ^{252}Cf (40,203n n/s) source for determining the fast-neutron detection efficiency. The ^{137}Cs source activity was determined such that it matched the gamma-ray activity of the ^{252}Cf. To establish a basis of comparison between the performances of the MLFDs and the Hornyak button, both were tested using the same setup. To obtain the neutron net counts, a background is run with the source and the PMT, without the MLFD or the Hornyak button, in the same orientation, and the counts are subtracted from the count rate when the source, detector, and PMT is present.

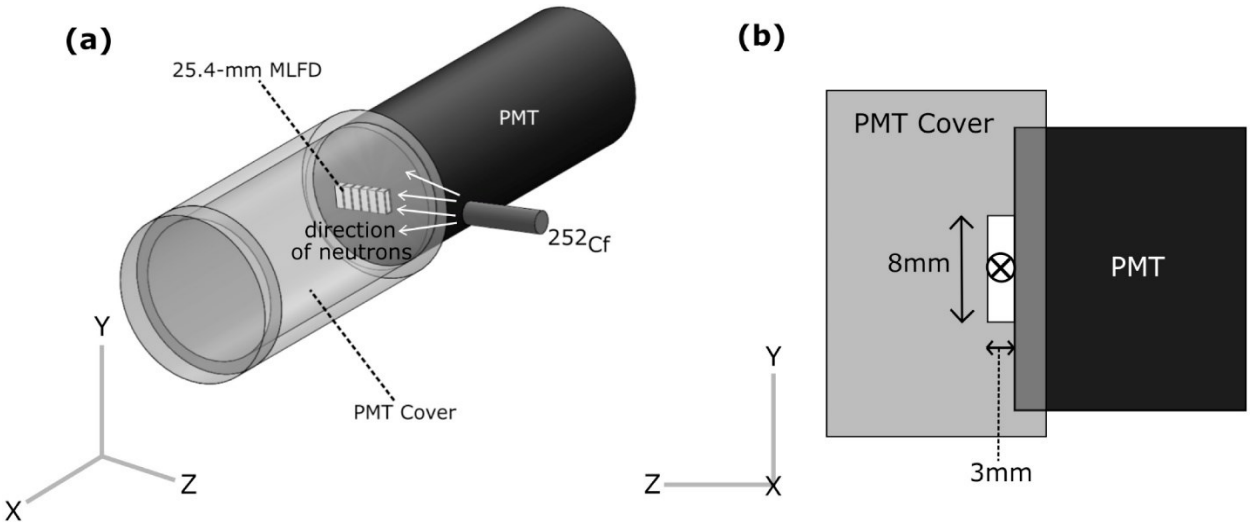

Figure 6-1. (a) MLFD mounted to a PMT relative to a ^{252}Cf source. The PMT cover ensures a light-proof setup; in this diagram it is shown to be translucent to emphasize the experimental orientation of the MLFDs, (b) same setup from different axes view. The 'x' marks the plane the neutrons are perpendicularly incident upon. Reproduced with permission from Elsevier [54].

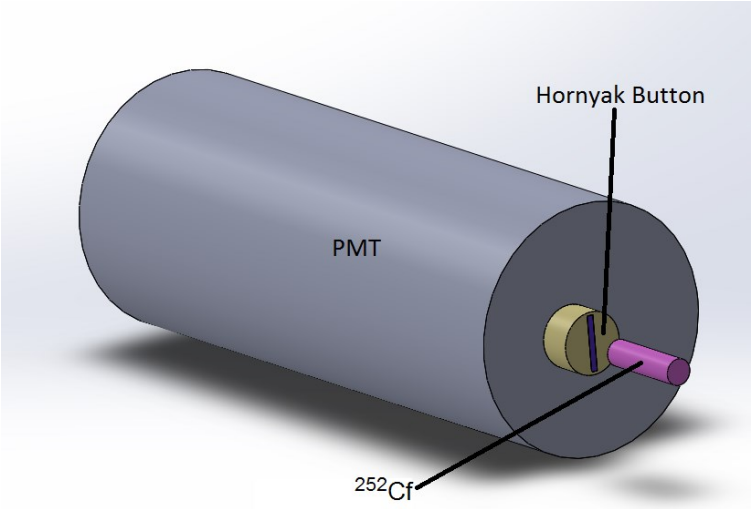

Figure 6-2. Orientation of the ^{252}Cf source with respect to the Hornyak button as oriented at TREAT. The Hornyak button in this diagram was not painted with a reflector, to illustrate the detector-source orientation clearly.

To calculate the solid angle between the isotropic disk ^{252}Cf source and the rectangular face of the detector (where the center of the source is directly above a corner of the 8 mm × 3 mm detector face) as shown in Figure 6-1(b), the distance *r* in Figure 6-3 is:

$$r^2 = d^2 + r_s^2 + x^2 + y^2 - 2r_s\sqrt{x^2+y^2}\cos\left[\phi_s - \cos^{-1}\left(\frac{x}{\sqrt{x^2+y^2}}\right)\right] \tag{6.1}$$

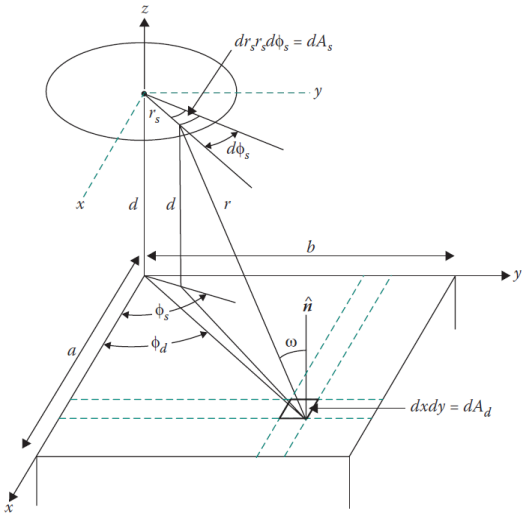

Figure 6-3. Solid angle for a disk source with its center directly above one corner of a detector with a rectangular aperture [59].

Equation (2.25) can, in this case, be written as:

$$\Omega = \frac{1}{4\pi A_s d^2}\int_0^{R_s} dr_s r_s \int_0^{2\pi} d\phi_s \int_0^{a} dx \int_0^{b} dy \left\{1 + \frac{r_s^2}{d^2} + \frac{x^2}{d^2} + \frac{y^2}{d^2} - 2\frac{r_s}{d}\sqrt{\frac{x^2+y^2}{d^2}}\cos\left[\phi_s - \cos^{-1}\left(\frac{x}{\sqrt{x^2+y^2}}\right)\right]\right\}^{-\frac{3}{2}} \quad (6.2)$$

Because R_s/d (R_s being the source radius), a/d and b/d are less than 1, the expression in brackets can be expanded in the series. Retaining only the first four terms [59]:

$$\Omega = \frac{\omega_1\omega_2}{4\pi}\left[1 - \frac{3}{4}\varphi^2 - \frac{1}{2}(\omega_1^2+\omega_2^2) + \frac{1}{8}(5\varphi^4 + 3\omega_1^4 + 3\omega_2^4) + \frac{5}{4}\varphi^2(\omega_1^2+\omega_2^2) - \frac{35}{64} + \frac{5}{12}\omega_1^2\omega_2^2 - \frac{35}{16}\varphi^4(\omega_1^2+\omega_2^2) - \frac{7}{32}\varphi^2(9\omega_1^4 + 9\omega_2^4 + 10\omega_1^2\omega_2^2) - \frac{7}{16}\omega_1^2\omega_2^2(\omega_1^2+\omega_2^2) - \frac{5}{16}(\omega_1^6+\omega_2^6)\right] \quad (6.3)$$

where $\omega_1 = a/d$, $\omega_2 = b/d$, and $\varphi = R_s/d$.

Therefore, the solid angle between the isotropic disk ^{252}Cf source and the rectangular face of the detector (where the center of the source is directly above the center of the 8 mm × 3 mm detector face), as was the case in the experimental setup, was calculated by multiplying equation (6.3) four times. The detector face was divided into four equal rectangles such that the source is at the corner for each rectangle but at the center for all of them together, as shown in Figure 6-4. Appendix-#2 contains a code written in MATLAB to determine the solid angles for varying detector-to-source distances, that utilize the equations used above.

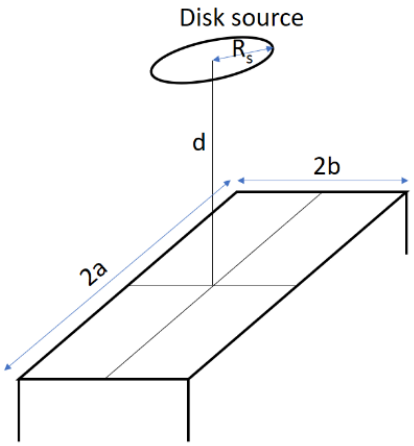

Figure 6-4. A disk source whose center is located directly above the center of a detector with a rectangular aperture. The solid angle is equal to four terms, each given by equation (6.3).

The orientation emulated the placement of the Hornyak buttons in the hodoscope with respect to the fast neutron beam from the fuel element. The source was placed 100 mm away from the MLFD (to ensure minimal variation in flux across the length of the MLFD at this distance). The PMT was biased at 1000 V. The scintillator, PMT and radioactive sources were placed inside an electrically-insulated light-tight box, and were connected to an ORTEC 113 preamplifier and amplifier via feedthroughs in the light-tight box. The amplifier was connected to an MCA (an oscilloscope was added to view the pulses), and was finally read out to a computer to display the pulse height spectrum using the Maestro software (Figure 6-5). Each measurement was run thrice for 10 h.

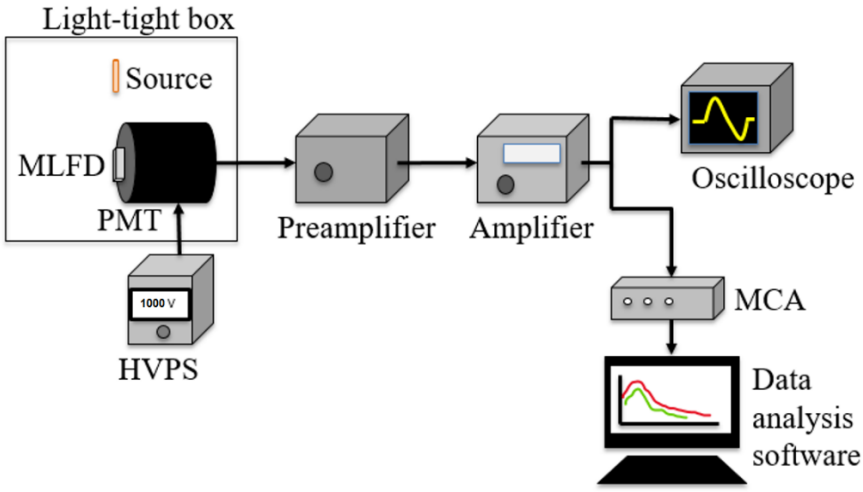

Figure 6-5. MLFD-PMT detection system setup with necessary NIM equipment.

Although the energy response of ZnS:Ag to protons is not well-characterized, inorganic materials have been known to show non-proportional response to nuclear recoils, especially at lower energies [60]. Using characteristic gamma-ray energies to calibrate neutron energies would also prove futile for calibration, as the scintillation light yield for a nuclear recoil of a given energy is quenched, and thus less than the output from an electron recoil of the same energy [61]. Hence, the PHS bins were not calibrated for energy and are represented as channels or discriminator voltage, corresponding to the amount of charge deposited in the anode. The lower level discriminator (LLD) was set at the channel for which the count rates from ^{137}Cs were negligible in comparison to the counts from ^{252}Cf. The average pulse height of a photon, and hence the LLD, was 250 mV (corresponding to channel 22 in the multi-channel analyzer software for the selected gain). Although a direct correlation between energy and pulse height has not been established, it is commonly known that pulse height increases with increasing energy deposition. Thus, it has been reasonably assumed that in Figure 6-6, as one moves to the right of the -axis, the energy deposited increases.

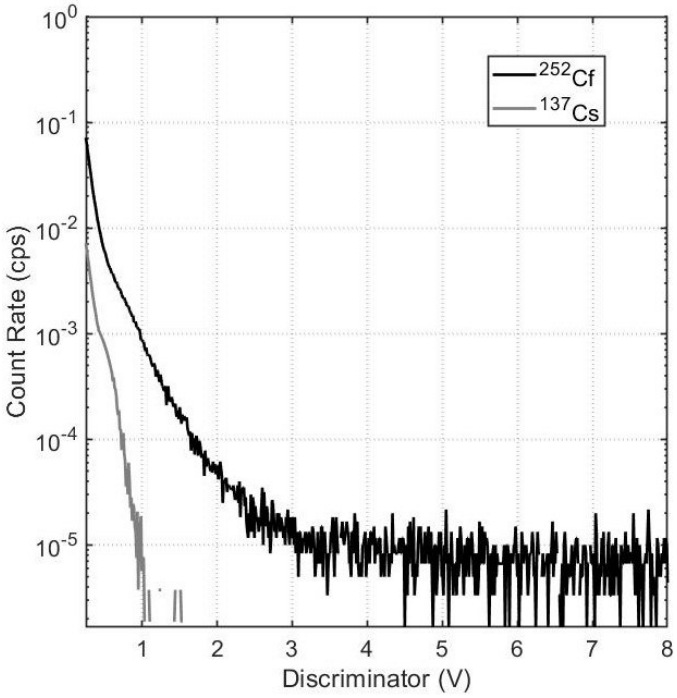

Figure 6-6. PHS of a 25.4 mm MLFD when irradiated with ^{252}Cf and ^{137}Cs. Reproduced with permission from Elsevier [47].

The intrinsic fast neutron detection efficiency for the 25.4 mm MLFD was determined to be 8.10 ± 0.13 %, with the aforementioned LLD. The intrinsic gamma-ray detection efficiency was 0.012 ± 0.002 %. For comparison, a 25.4 mm Hornyak button was determined to have a fast neutron detection efficiency of 3.22%. Since longer lengths were predicted to produce higher efficiencies, 3 different lengths of MLFD were fabricated, limited by the diameter of the PMT: a 12-mm, 25.4-mm, and a 40-mm long MLFD (Figure 6-7).

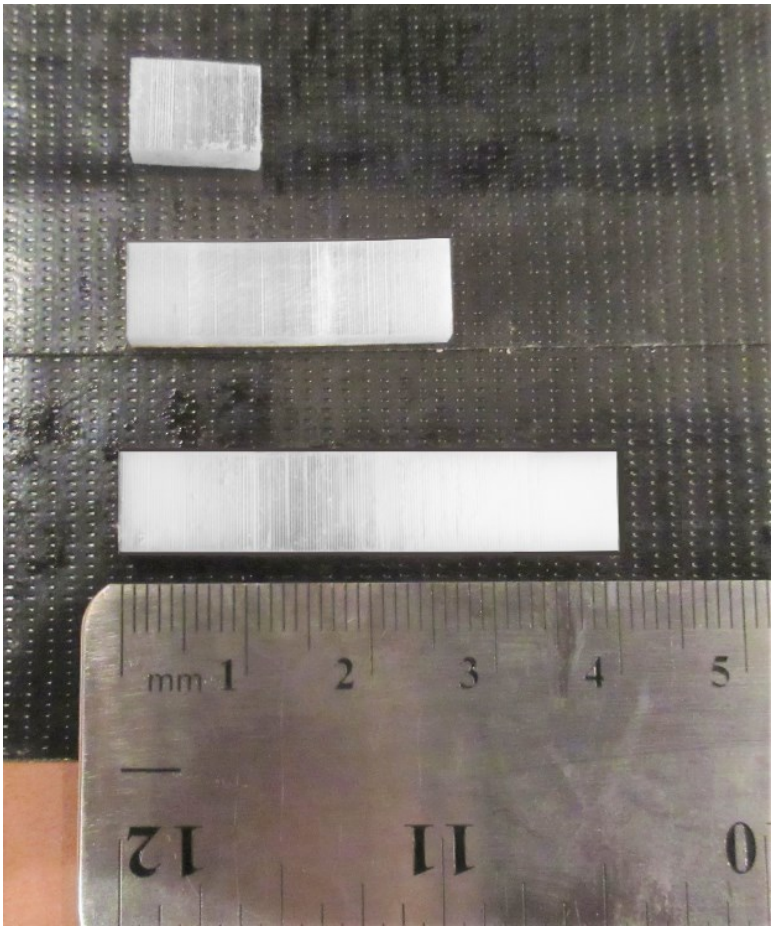

Figure 6-7. Three lengths of MLFDs were fabricated and tested: 12 mm, 25.4 mm, 40 mm [47].

The three MLFD's were optically coupled, separately, to the PMT. Each MLFD was irradiated with a ^{137}Cs source (166,500 /s at the time of the experiment) to determine the LLD setting, and with a ^{252}Cf source (40,203 n/s at the time of the experiment) to determine its fast-neutron detection efficiency. ^{252}Cf produces approximately four gamma rays per neutron during its spontaneous fission [47], so the ^{137}Cs source was chosen with an activity closest to the number of gamma rays emitted from the ^{252}Cf source.

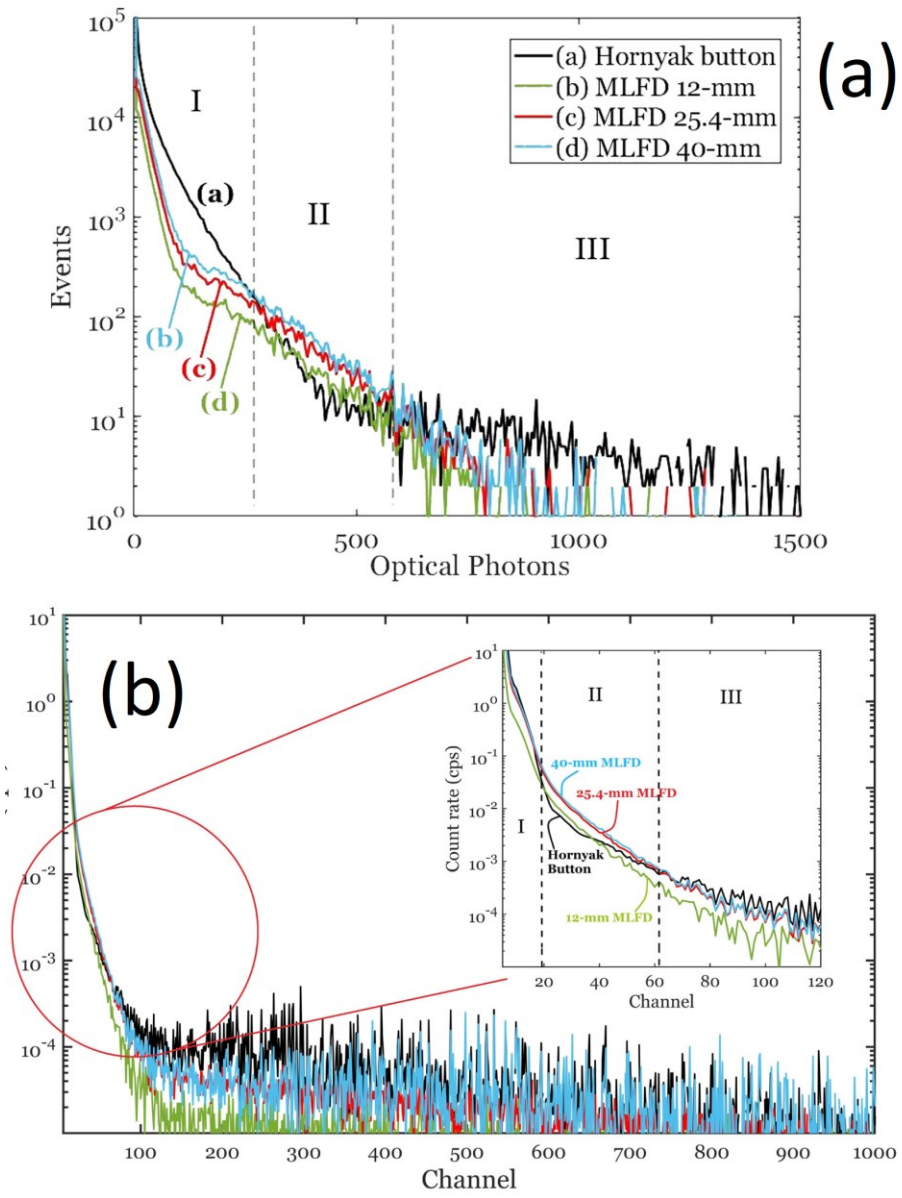

Figure 6-8. (a) Theoretical combined neutron, gamma-ray, and Ĉerenkov spectra of the three MLFDs compared to the Hornyak button spectra, on being irradiated with a ^{252}Cf source, and (b) experimental spectra of the MLFDs compared to the Hornyak button when irradiated with an unshielded ^{252}Cf source. The spectral trends are shown in the inset in the initial channels. Reproduced with permission from Elsevier [47].

Shown in Figure 6-8(a) are the theoretical full spectra, including effects from Ĉerenkov generation in the scintillator, gamma rays, and neutrons. As expected, the net count rate increases throughout the spectrum for increasing lengths of MLFD. There are three sections of interest in the spectra: regions I, II and III. Region I depicts an area where count rates from Ĉerenkov and

gamma radiation dominate over neutron count rates, especially for the Hornyak button. The steeper slope of the MLFD curve as compared to that of the Hornyak button depicts the superior gamma-ray rejection capabilities of the former. In region II, the Ĉerenkov contribution is negligible, and the MLFD slope is produced almost exclusively from neutrons [26]. The MLFD count rate is higher than the Hornyak button count rate in region II, owing to the greater volume of scintillation material, higher probability of neutron interaction, and improved light collection in the MLFD. For the Hornyak button, the region II curve continues the same slope at it did in region I, and is still dominated by gamma and Ĉerenkov radiation. In region III, the MLFD count rates drop slightly below the Hornyak button count rates. The experimental spectra (Figure 6-8(b)) agreed with the predicted spectra in regions I and II, but differ in region III, where the 40-mm MLFD count rate exceeds the Hornyak button count rate beyond channel 400. Shown in Figure 6-9 are the detection efficiencies for the 3 MLFD lengths.

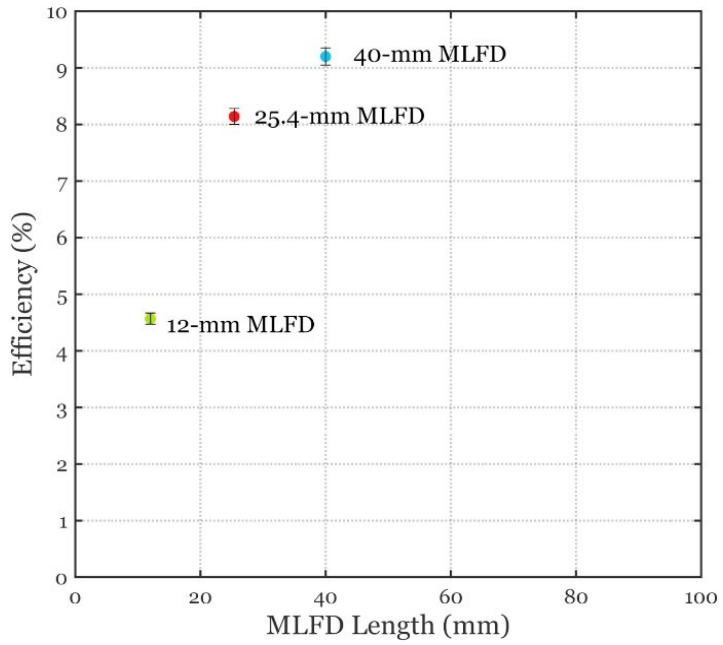

Figure 6-9. Intrinsic detection efficiencies for the 3 MLFDs for a bare, isotropic ^{252}Cf source [47]. Reproduced with permission from Elsevier [47].

Effects of Epoxy

To explain the disparity between the ideal and fabricated detectors in Figure 6-8, one must note the key differences between the experimental setup and the theoretical model. The simulation assumed an ideal MLFD, and therefore modeled the scintillator without any epoxy. The fabricated

MLFD contains a homogeneously mixed epoxy ($C_{21}H_{25}ClO_5$) and ZnS:Ag in each scintillation layer. The presence of the epoxy in the ZnS:Ag layer reduces the advantage of forward-propagating protons in the ZnS:Ag layer and therefore lowers their probability of interaction. The homogeneous mixture of epoxy and ZnS:Ag consequently also causes lower interaction of forward-propagating Ĉerenkov and gamma rays, a desirable quality (although additional Ĉerenkov radiation may be generated from gamma-ray interaction in the epoxy as well, Figure 6-10). Another effect of the inclusion of the epoxy is the reduction in the total number of layers for any given length of an ideal MLFD, thereby reducing the ZnS:Ag content by 11.2% (by weight). The total amount of hydrogen is reduced very slightly (1.1%) because the H in the epoxy compensates for the missing PMMA layers. This difference will clearly result in reduced scintillation and light collection. On the other hand, the cured epoxy also contains an undetermined amount of chlorine, leading to additional counts by the $^{35}Cl(n,p)^{35}S$ and $^{35}Cl(n,\alpha)^{32}P$ reactions (Table 6-1), especially beyond 2 MeV (Figure 6-11). This phenomenon might explain the slight minor increase in count rates observed at higher channels. However, the chlorine content is unknown because, while chlorine is a part of a by-product that should have been expelled out of the epoxy upon curing, an appreciable portion of it remains in the cured plastic as hydrolyzable and inactive chlorine [47]. For the initial channels, the lower content of ZnS:Ag, and diminished forward-propagated detection for both neutrons and gamma rays may offset the slight increase in counts due to the aforementioned reactions with chlorine. Additionally, chlorine is known to degrade the optical properties and induce de-lamination over time.

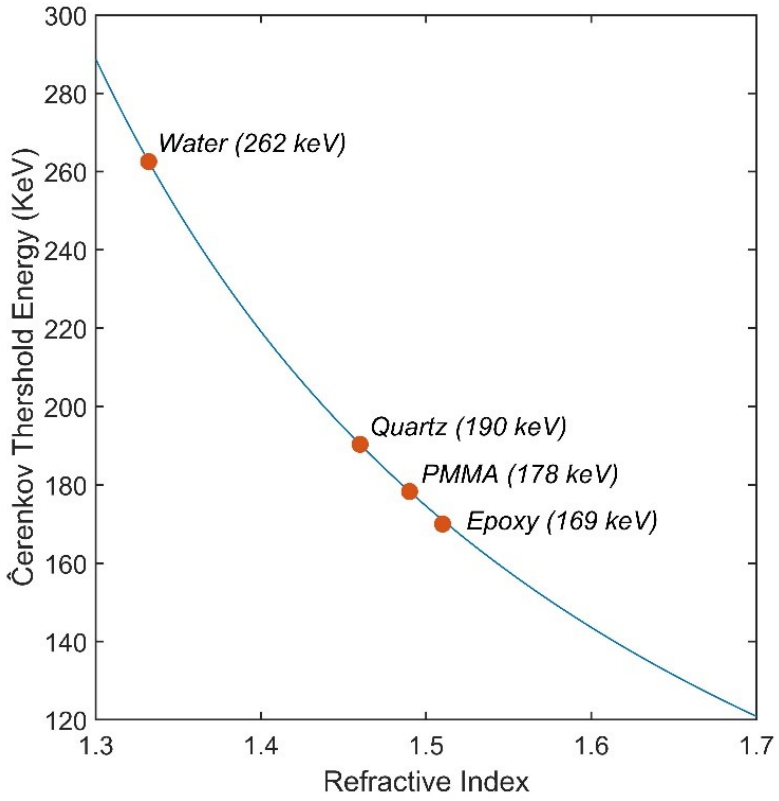

Figure 6-10. Gamma-ray interaction in the epoxy can produce Ĉerenkov radiation, as given by equation (2.4).

Table 6-1. Threshold energies for various reactions occurring in the scintillation layer of the MLFD.

Reaction	Q-value	Threshold energy
$^{32}S(n, p)^{32}P$	−0.93 MeV	0.957 MeV [62]
$^{35}Cl(n, p)^{35}S$	0.615 MeV	No threshold [63]
$^{35}Cl(n, \alpha)^{32}P$	0.937 MeV	No threshold [63]

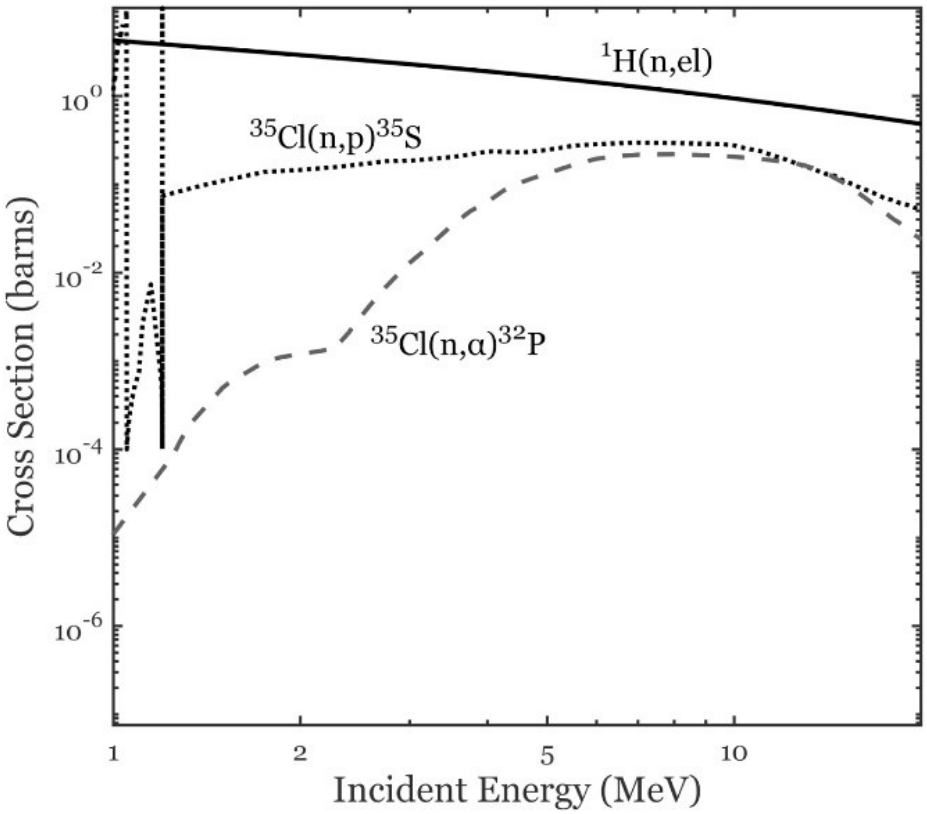

Figure 6-11. Neutron cross-sections of reactions from chlorine in the epoxy. For comparison, the main elastic scattering reaction of neutrons with hydrogen is shown. Reproduced with permission from Elsevier [12].

6.2 Gamma-Ray Rejection

In a pulse height spectrum, an LLD is usually set to discriminate counts below the set value. All events—neutrons, gamma-rays, background, electronic noise—below the LLD are rejected. Hence, the neutron detection efficiency and the gamma-ray detection efficiency both decrease with increasing LLD. The optimum LLD is usually dependent on the application. The detection efficiency is calculated as a function of the number of counts above this threshold.

The *n/γ ratio* increases with increasing LLD (Figure 6-12), although raising the LLD beyond channel 22 would start rejecting a significant portion of fast neutron-induced counts, thereby reducing the neutron detection efficiency. It is interesting to note that the 25.4-mm MLFD has an initial higher *n/γ ratio* than the 43-mm MLFD, but beyond channel 51, the longer MLFD has the higher *n/γ ratio*. Shown in Table 6-2 are the neutron and gamma-ray detection efficiencies of the MLFD above an LLD of 250 mV.

Table 6-2. Intrinsic fast-neutron detection efficiencies and their *n/γ ratios* for different MLFD lengths, with the LLD set at 250 mV.

MLFD length (mm)	Gamma-ray detection efficiency (%)	Fast-neutron detection efficiency (%)	n/γ ratio at LLD 250 mV
12	0.009	4.75 ± 0.09	527.77
25.4	0.012	8.10 ± 0.13	675.00
43.0	0.021	9.15 ± 0.14	435.71

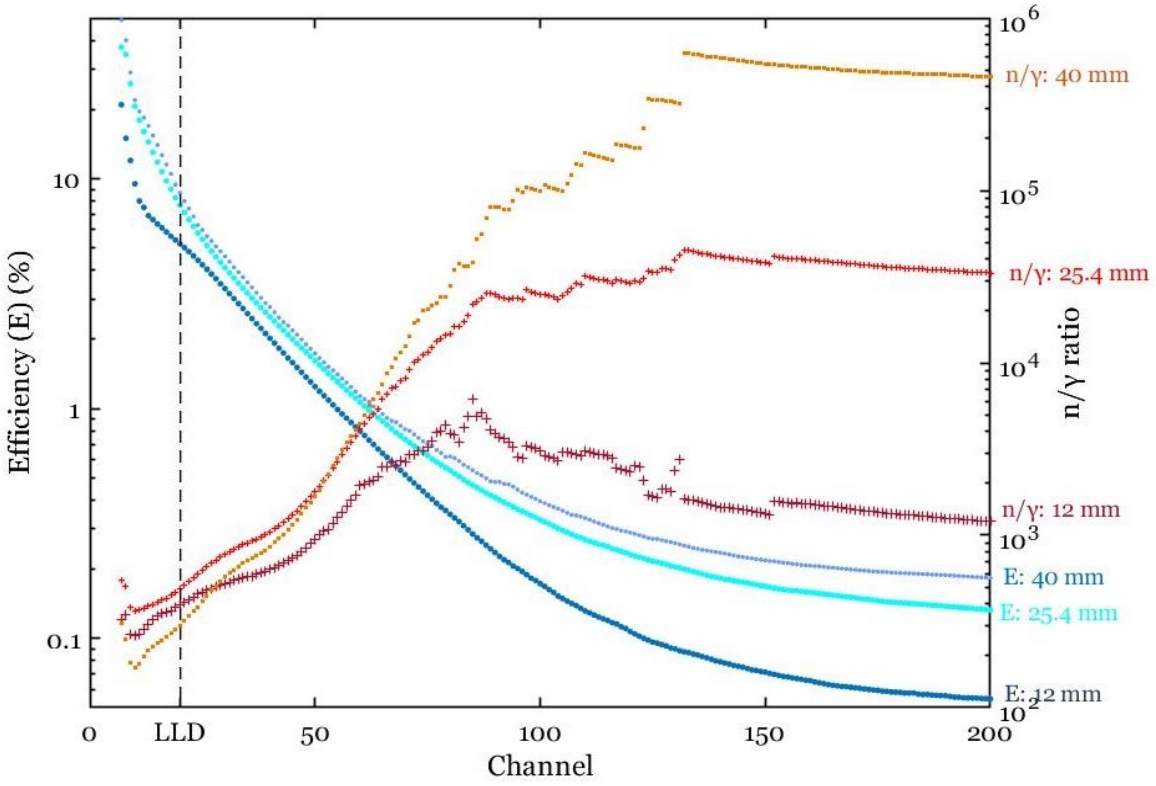

Figure 6-12. Intrinsic fast neutron detection efficiencies (E, left y-axis) and the corresponding *n/γ ratio* (right y-axis) for the 3 lengths of the MLFDs.

The fast neutron detection efficiency essentially becomes a function of the LLD, and the application would dictate whether gamma-ray rejection or higher neutron detection efficiency is the more important feature required. With the aim of removing gamma-ray, Ĉerenkov radiation and background contamination without compromising neutron events, pulse shape discrimination was performed.

6.3 Pulse Shape Discrimination

To test the PSD properties of the MLFD, the 40-mm long detector was optically coupled to the PMT. A bare ^{252}Cf (32,279 neutrons/s) was used as the mixed neutron and gamma-ray source, while ^{137}Cs (125,800 γ/s) was used as the gamma-ray source, to irradiate the 8 mm × 3 mm face of the MLFD. The scintillator, PMT and radioactive sources were placed inside an electrically-insulated light-tight box. The assembly was connected to a fast digitizer and computer outside the dark box via bulkhead feedthroughs. To minimize cross-talk between cables and components, cables were kept as short and separated from one another as possible. The PMT was biased at 1000 V. The source was placed 10 cm from the front face of the MLFD; this distance was chosen such that point source approximations could be applicable. Digitized pulse data was acquired using a CAEN 14-bit DT5730 digitizer, which has a sampling rate of 500 MS/s. The DPP-PSD software was used to collect waveforms for post-process analysis, while CAEN's CoMPASS software produced real-time PSD information. CoMPASS also provided data for calculating the FoM post-process. MATLAB codes were written (Appendix-#5) post-process to separate the neutron and gamma-ray waveforms for determining decay characteristics. The CAEN DT5730 digitizer allowed for on-board real-time pulse shape discrimination according to previously-set short, long and pre-gates, while also enabling post-processing data offline. The gates can be set by the user before data acquisition takes place, along with a range of other settings [64].

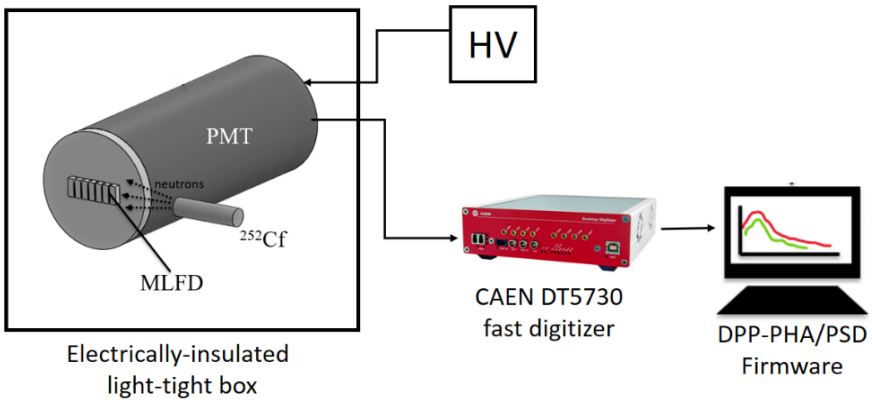

Figure 6-13. Experimental setup showing the source-and-detector orientation and the electronics and components used to acquire pulse data. Reproduced with permission from Elsevier [66].

Shown in Figure 6-14 are the short and long gates selected to separate neutrons (proton-induced pulse) and gamma rays (electron-induced pulse). The charge integration starts from a

negative pre-gate, and a baseline gate is determined to set a reference for the total charge integration within the long and short gates.

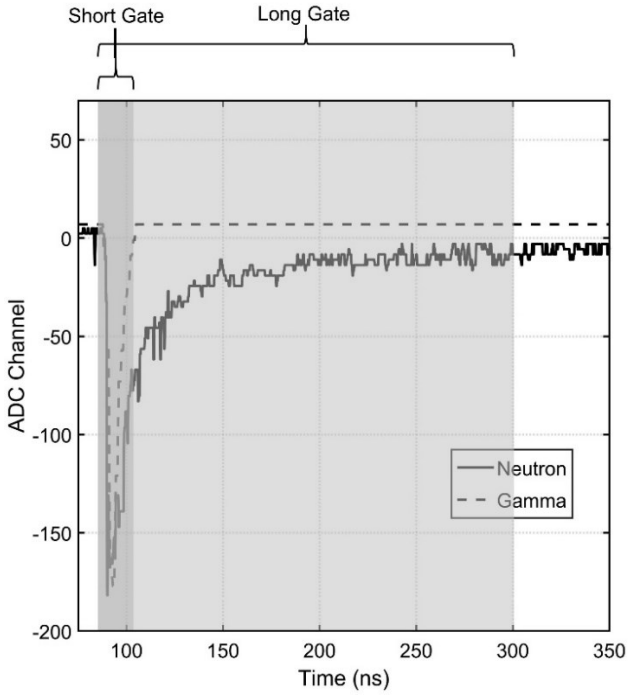

Figure 6-14. . Single neutron and photon pulses from the MLFD when irradiated with ^{252}Cf, as seen from the DPP-PSD software. The short and long gates can be varied according to the user [66].

Shown in Figure 6-15(a) shows the response of the MLFD to a bare ^{252}Cf source with a short gate of 40 ns and a long gate of 300 ns. The PSD plots were obtained using a MATLAB listed in Appendix-#6. Two clearly separated bands can be seen, with a vertical band overlapping the bottom band under ADC channel 500. The identities of the various peaks and features in Figure 6-15(a) were verified by performing separate irradiations (Figure 6-15 (b),(c),(d)). The response of the MLFD to the ^{252}Cf was first compared to its response to a ^{137}Cs source of activity that matched closely with the gamma-ray emission from ^{252}Cf. The results of Figure 6-15(b) clearly demonstrate that the lower band comes from gamma-ray irradiation, while the upper band in Figure 6-15(a) is from neutrons, which is not present in the response from ^{137}Cs irradiation. Figure 6-15(c) was obtained by irradiating the PMT without the MLFD (in the same orientation as with the MLFD) to account for Ĉerenkov illumination and direct gamma-ray interactions in the PMT photocathode and glass envelope. Although the amount of Ĉerenkov radiation generated in the PMMA layer was not experimentally determined, the Geant4 model predicted that the Ĉerenkov

light produced in MLFD is negligible [26]. Another experiment was performed with no source present, but with the MLFD coupled to the PMT, to account for electronic noise and background radiation. The vertical band in Figure 6-15(d) below ADC channel 500 has clearly developed from electronic noise. Comparing Figure 6-15(c) and (d), Ĉerenkov radiation has a moderate contribution to the detected light. The response plots indicate that the electronic noise, Ĉerenkov, and gamma-ray induced pulses have similar PSD ratios. The gamma-ray band is also quite shorter than the neutron band across the x-axis, a phenomenon that is in marked contrast with the longer gamma-ray bands found in plastic scintillator responses [65]. These results demonstrate the inherent ability of the MLFD to reject gamma rays. A very clean separation of neutrons from gamma rays, Ĉerenkov radiation, and electronic noise is achieved with the MLFD.

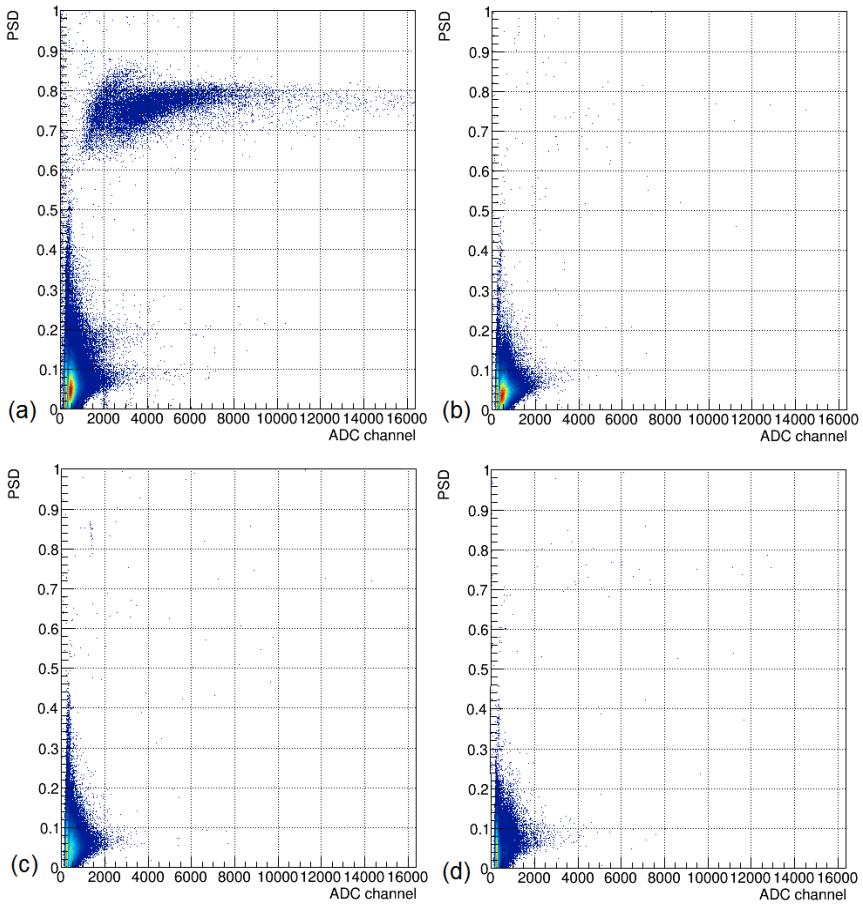

Figure 6-15. Pulse-shape discrimination contour plots showing MLFD-PMT system responses to irradiation with (a) ^{252}Cf, (b) ^{137}Cs, (c) ^{252}Cf without the MLFD, and (d) no source present [66].

To summarize, Figure 6-16 represents the different features of the MLFD response to bare ^{252}Cf. The neutron signal is represented by (i), and (ii) represents gamma-ray and Ĉerenkov events. The origin of (iii) has been considered to be from pulse-pile up of gamma-rays from ^{252}Cf, as this feature was not present in the MLFD response to ^{137}Cs (Figure 6-15(b)). Electronic signal contributes to (ii), and is also responsible for the vertical line labelled (iv). Figure 6-16 clearly indicates that pulse height discrimination is not enough by itself to reject gamma rays and Ĉerenkov radiation without significantly reducing the neutron count in the MLFD-PMT detection system. Due to the large difference in PSD ratios of neutrons and gamma-rays, PSD can easily discriminate between neutrons and non-neutron events. However, it is commonly known that PSD is inaccurate and can even fail at very low energies, because the tails of neutron pulses of small energies can fall within the short gate, thereby resulting in an incorrect PSD ratio. This phenomenon likely explains the absence of events in the neutron band below channel 1000, and indicates the misclassification of neutrons of lower energy.

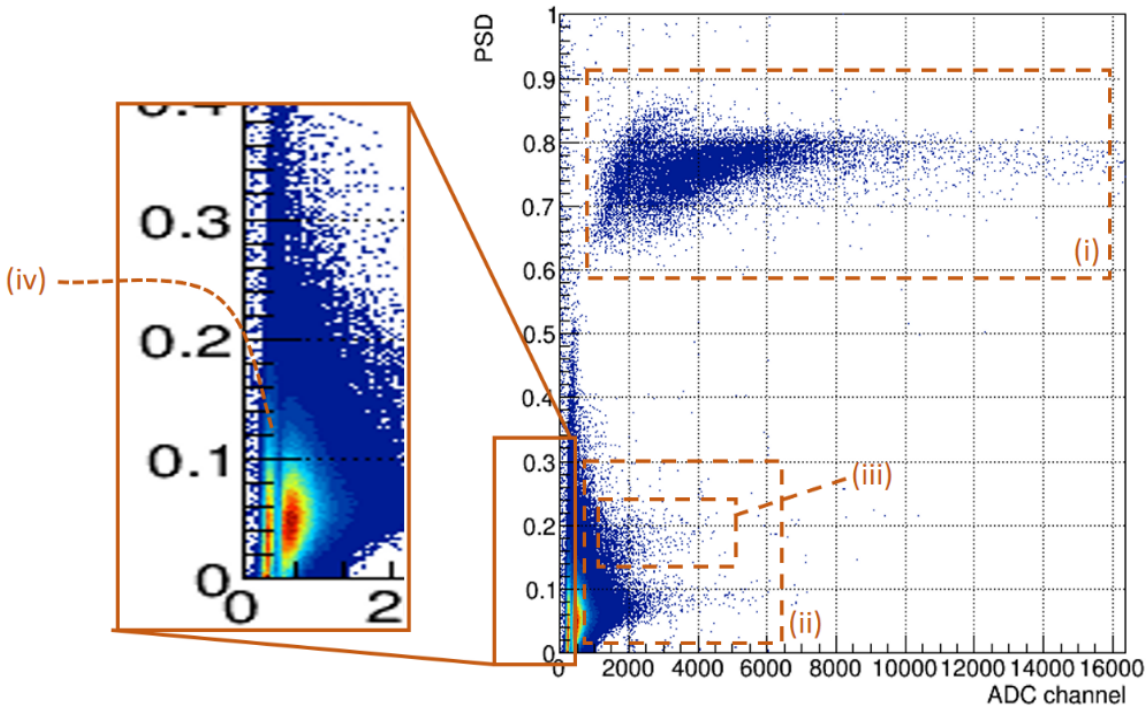

Figure 6-16. Notable features of the contour PSD plot for ^{252}Cf irradiation of the MLFD. Reproduced with permission from Elsevier [66].

6.3.1 Neutron Detection Efficiency after PSD

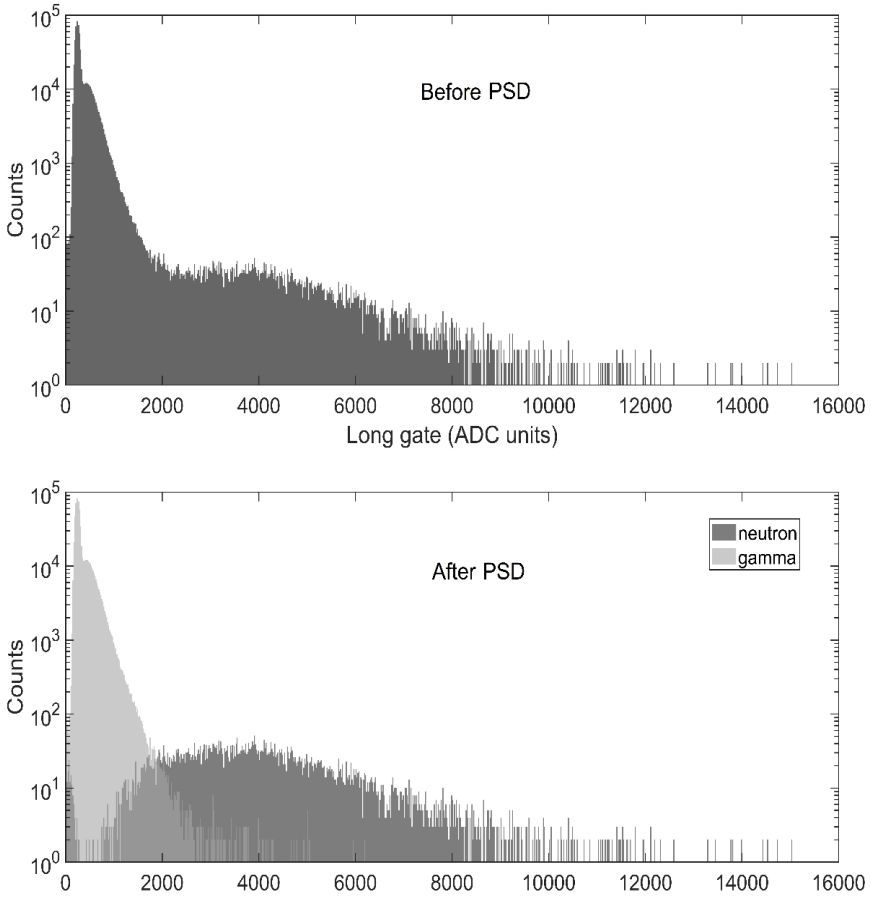

Figure 6-17. ^{252}Cf fission spectrum as observed by the MLFD before PSD (top), and after PSD (bottom) [66]. Reproduced with permission from Elsevier [66].

The result of performing PSD on the MLFD upon ^{252}Cf irradiation is shown in Figure 6-17. Shown in the top image is the ^{252}Cf fission spectrum before performing PSD, while data in the bottom figure was obtained after performing PSD. With the lower level discriminator (LLD) set to 0, both neutrons and gamma rays were mixed in the spectrum. The bottom figure includes events from gamma rays, Ĉerenkov radiation, and electronic noise, but shows the spectra from neutron and gamma rays separately. The different spectra reassert the fact that pulse height discrimination alone would either include significant number of gamma-ray events, if LLD is set at channel 2000 approximately, a significant portion of neutrons are also discounted. For achieving higher reliability of data, pulse shape discrimination becomes necessary.

PSD Performance

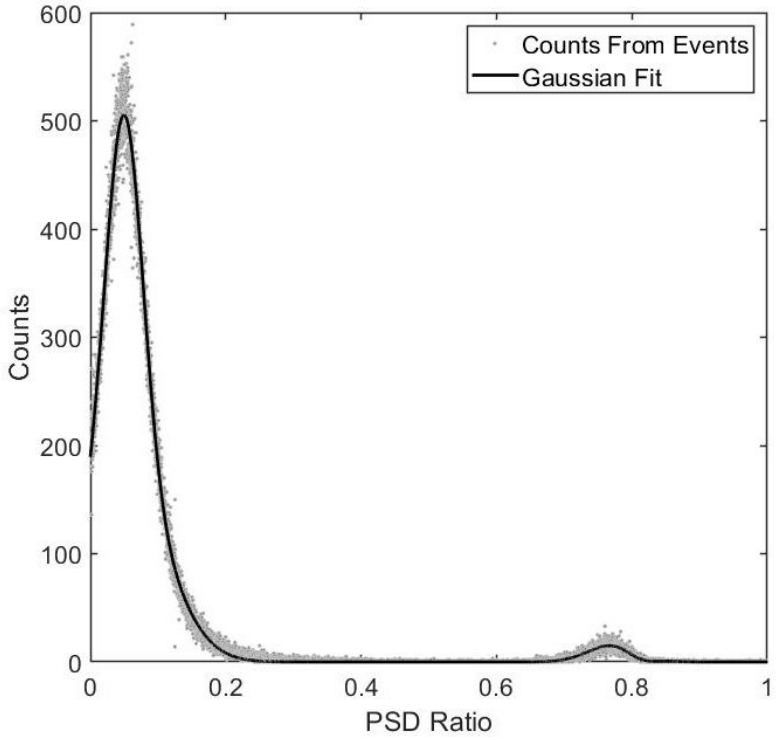

Figure 6-18. Plot of counts versus PSD ratio to quantify the PSD capability of the detection system [66].

To quantify the goodness of neutron-gamma separation, the FoM for the 300-40 ns combination was determined, using equation (2.15). To obtain the centroids and the FWHM values of the neutron and photon peaks, a Gaussian fitting was performed (Figure 6-18), which accurately described the data ($R^2 = 0.99$ for the photon peak, $R^2 = 0.90$ for the neutron peak). The taller of the peaks represents the counts collected from electronic noise, Ĉerenkov radiation, and gamma rays. The other peak represents counts almost exclusively from neutrons.

The selection of the gates can have a large impact on the quality of separation of particles. Data acquisition with several combinations of long and short gates was performed; the FoM for each combination being the determinant in selecting an optimum combination. From Table 6-3, the 300-40 ns combination of long-short gate has the highest FoM. This combination was used throughout the rest of the study. It is interesting to note that all of the combinations produced an FoM of over 1.27, the threshold value for acceptable discrimination. It is evident that the delayed component plays a more significant role than the prompt component in determining the PSD ratio.

Table 6-3. Different combinations of short and long gates used and their corresponding FoM calculated in order to determine the optimum gate windows. The highlighted values represent the optimal gates for the highest FoM.

Long Gate (ns)	Short Gate (ns)	FoM
300	50	4.38
300	40	4.56
300	30	4.18
250	40	3.92
150	50	3.68
150	40	3.89
150	30	3.58
80	40	2.54

Discrimination in increasing gamma-ray fluxes

Liquid scintillators and other PSD scintillators are commonly known to have reduced discrimination capabilities in environments with high gamma-ray fluxes [3]. For plastic scintillators, degradation in PSD performance was previously observed at an x-ray flux of about 3×10^7 γ/s, due to pulse pile-up effects at high count rates corrupting the digital PSD algorithm [67]. In fact, at high fluxes, the detector dead time may increase high enough to paralyze the detector, causing misidentification of pulse types. To gauge the performance of the MLFD in higher gamma-ray backgrounds, the 40 mm MLFD was irradiated with a 0.1 Ci AmBe source. The distance of the source from the MLFD was decreased from 17 cm to 0.3 cm to increase the gamma-ray flux incident on the MLFD. The FoM decreased from 4.68 at 0.4 mR/hr to 4.05 at 1287.7 mR/hr, as shown in Figure 6-19. It should be noted that the FoM remains above 4 even in high gamma-ray fluxes, and no severe degradation of PSD performance or corruption of the signal was observed in any of the cases. In all cases, the FoM has remained above 1.27, the minimum acceptable threshold. Hence, the quality of discrimination remains acceptable even in high-flux mixed radiation fields.

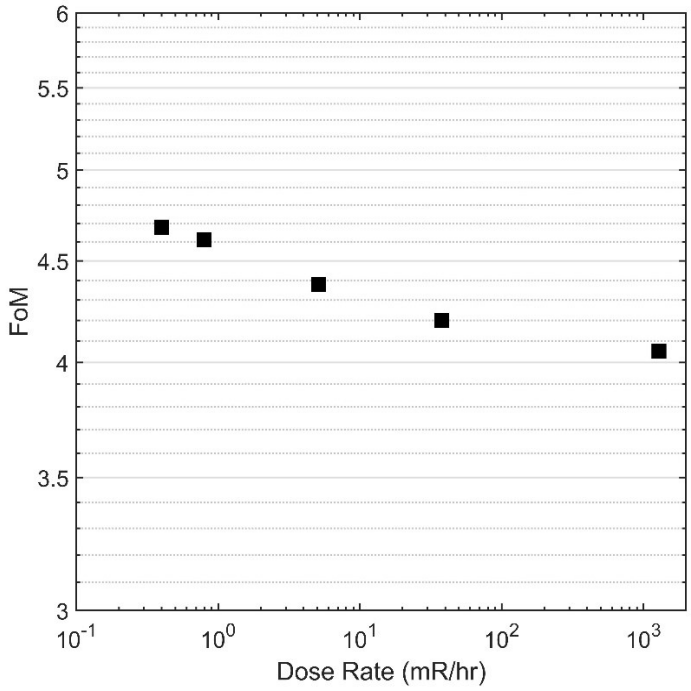

Figure 6-19. Measured FoM values of the MLFD for increasing gamma-ray dose rates from AmBe.

6.3.2 Photodetection with Silicon Photomultipliers

Thus far in the described work, the MLFD had been coupled to a PMT for scintillation light collection. Pulse shape discrimination of neutrons and gamma-ray events using the charge integration technique indicate that the MLFD can potentially be used in active and passive interrogation and Special Nuclear Materials (SNM) searches, which require the detection system to be compact and robust. PMTs are generally quite bulky and not easily portable, while silicon photomultipliers (SiPMs) are more rugged and require comparatively much lesser power to operate. Additionally, modeling in Geant4 has shown that the detection efficiency of the MLFD increases with increasing length of the detector [26]. The logical next step in the development of the MLFD for the aforementioned applications is to replace the PMT with SiPMs.

Numerical simulations had predicted that the gamma-ray contribution to count rate could be eliminated by using pulse-height discrimination alone [26], but Figure 6-17 indicates that there was significant overlap in neutron and gamma pulse-height spectra. To study if the photomultiplier window was responsible for the discrepancy between experimental results and numerical predictions, the PMT was replaced with a SiPM.

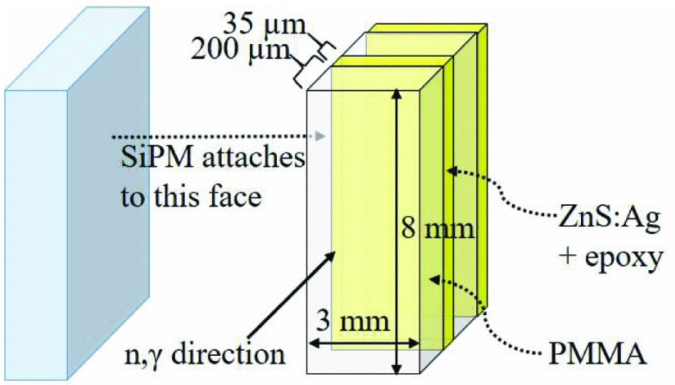

Figure 6-20. The PMT was replaced with a SiPM, with all other conditions, including orientation, remaining the same.

The mounted PCB was directly connected to a digitizer and oscilloscope via the standard output. A bare ^{252}Cf (32,279 neutrons/s) was used as a mixed neutron and gamma-ray source, while ^{137}Cs (125,800 γ/s) and ^{60}Co (14,448 γ/s) were used as gamma-ray sources, to irradiate the 8 mm × 3 mm face of the MLFD. 252Cf produces approximately four gamma rays per neutron per spontaneous fission, so the ^{137}Cs source was chosen to mimic the gamma-ray activity of the ^{252}Cf source. The scintillator, SiPM, and radioactive sources were placed inside an electrically-insulated light-tight box. Digitized pulse data was acquired using a CAEN 14-bit DT5730 digitizer with a sampling rate of 500 MS/s.

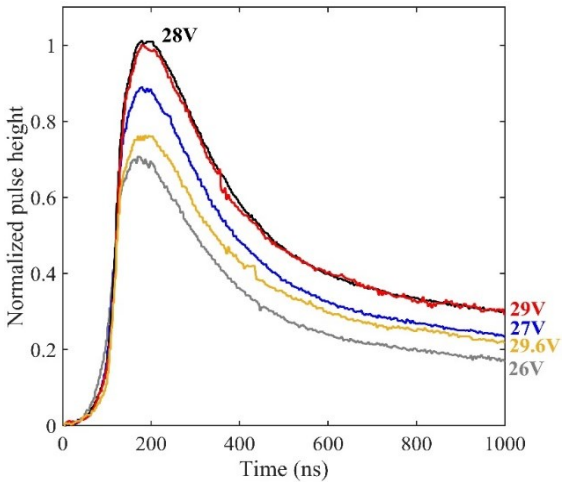

Figure 6-21. Neutron pulses (averaged over 500) produced by the MLFD at different operational bias voltages. A MATLAB code was used to extract the pulses from neutron events.

The MLFD was irradiated with a ^{252}Cf source at different operating voltages, and pulses were recorded as shown in Figure 6-21. The pulse height steadily increased on increasing the bias

voltage from 26 V to 28V. Beyond 29 V, the pulse height starts to decrease. These trends are expected, because with increasing overvoltage, the gain of the SiPM, and hence the pulse height, increases. However, with increasing overvoltage, the cross-talk between pixels also increases, leading to dark current impeding device operation. Therefore, the operating voltage of the SiPM-coupled MLFD was chosen to be 28 V.

Noise pulses (measured without any source present) were indistinguishable from gamma-ray pulses (measured in the presence of the aforementioned gamma-ray sources), as shown in Figure 6-21. Pulse-shape discrimination was used to distinguish between the neutron-originating pulses from the gamma ray-ones. Beyond 29.2 V, larger random pulses were observed on the oscilloscope, which were considered to be thermal or shot noise. The average gamma-ray pulse not only has a much shorter tail than that of the neutron pulse, but it is also considerably smaller.

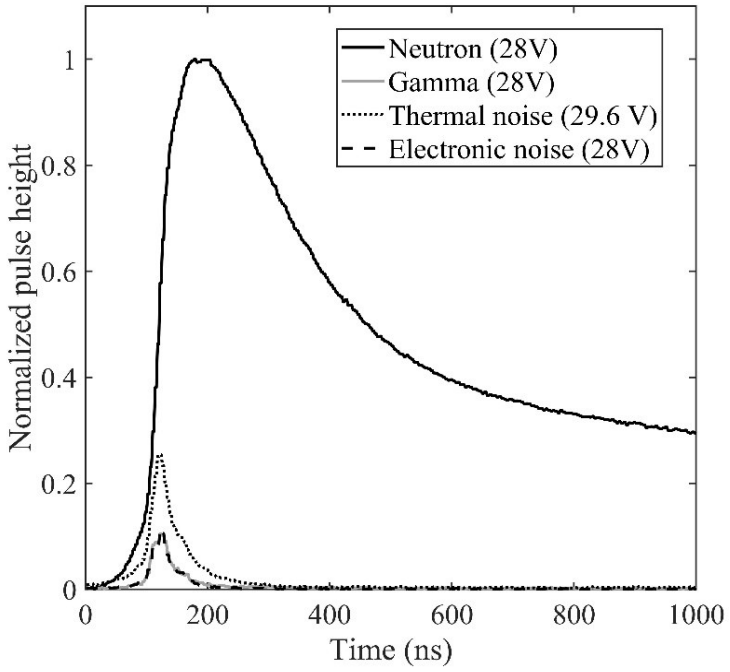

Figure 6-22. 500-average pulses produced by the MLFD upon neutron, gamma-ray irradiation. Electronic, background, and thermal noise are also shown for comparison [68].

It is interesting to compare the pulses of the MLFD-PMT system versus the MLFD-SiPM system. While the average neutron pulse tail remains the same in both the PMT and SiPM systems, the average relative gamma-ray amplitude in the SiPM system is much lesser than in the PMT system.

A relatively short amplitude of the gamma-ray pulse implies that simple pulse height discrimination would be sufficient to achieve a neutron-only spectrum. Shown in Figure 6-23(a) and (b) are pulse charge spectra of a 1-hour measurement, in which several individual gamma-ray pulses were plotted along with an averaged neutron pulse. A low LLD would be sufficient to remove a majority of gamma-rays from the spectrum. In comparison, in the PMT system (Figure 6-23(c)), the LLD would have to be higher to reject an appreciable amount of gamma-ray pulses, which would also remove neutron pulses, thereby lowering the neutron detection efficiency.

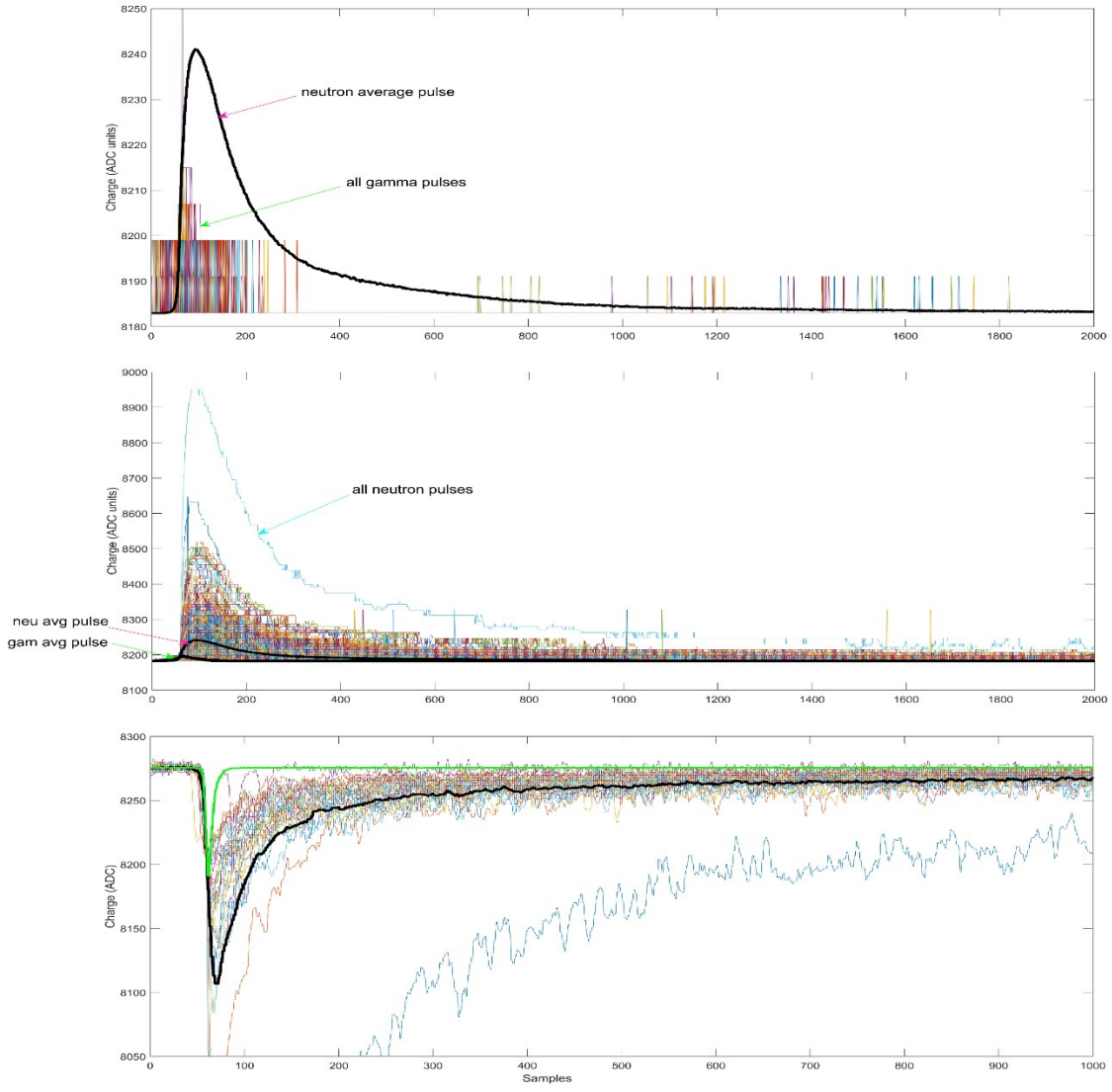

Figure 6-23. ^{252}Cf irradiation of (a) SiPM system showing an averaged neutron pulse compared to all gamma-ray pulses, (b) SiPM system showing all neutron pulses and average gamma-ray and neutron pulse, and (c) PMT system showing all neutron pulses and averaged neutron and gamma-ray pulse.

6.3.3 Pulse Shape Discrimination in the MLFD-SiPM vs. MLFD-PMT Systems

The PSD plots for the MLFD-PMT and MLFD-SiPM systems were compared. A bare ^{252}Cf (32,279 neutrons/s) was used as the mixed neutron and gamma-ray source, while ^{137}Cs (125,800 γ/s) was used as the gamma-ray source, to irradiate the 8 mm × 3 mm face of the MLFD. As shown in Figure 6-24, the MLFD-PMT system has a clear separation of neutron and gamma-ray events. An extended neutron branch was observed, along with a short but considerably denser gamma-ray branch. The corresponding spectrum shows an overlap in the gamma-ray and neutron spectra. The neutron count rate for the MLFD-PMT system was 0.34 cps, while the gamma-ray count rate was 16.15 cps.

The MLFD-SiPM system has a denser, extended neutron branch, however, no distinct gamma-ray branch was observed. This is expected, because the pulses recorded from gamma-ray sources were identical to the ones from electronic or background noise (no source present), and a threshold was applied to reject noise. For the MLFD-SiPM system, the neutron count rate was 0.78 cps, and the gamma-ray count rate was 0.078 cps.

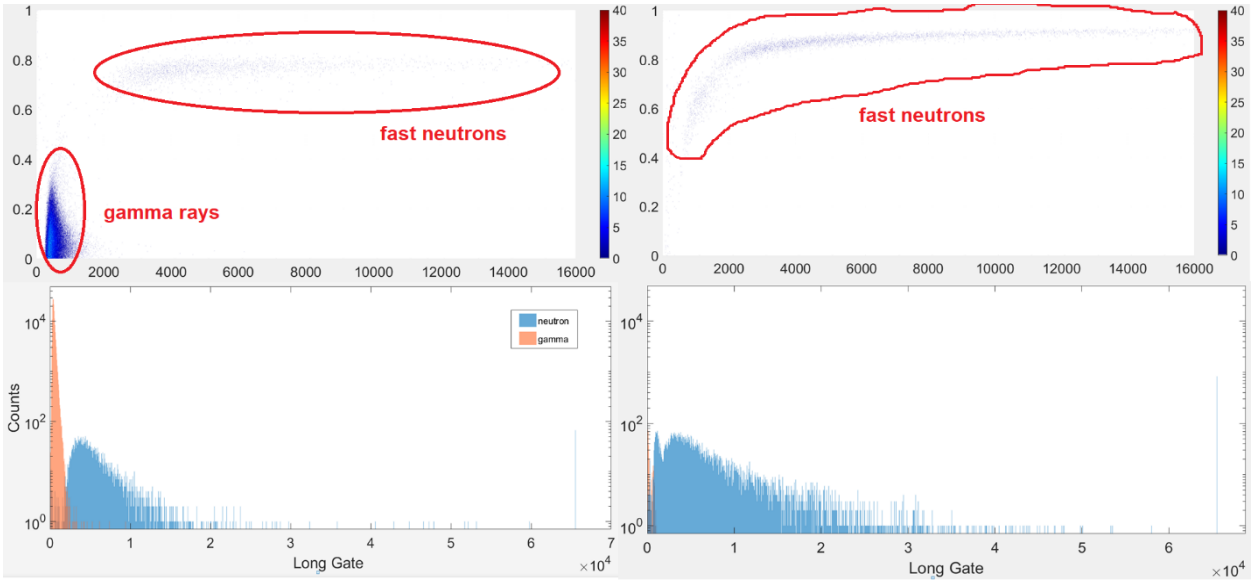

Figure 6-24. (Top) pulse-shape discrimination plot of the MLFD coupled to a PMT (left), and to a SiPM (right), and (bottom) their respective spectra after performing PSD.

The MLFD-SiPM detection system exceeds the performance of the MLFD-PMT system in that the gamma-ray sensitivity of the former seems to be negligible. This result proves what was

originally predicted [69]; that the MLFD design is essentially gamma-ray insensitive. The presence of gamma-ray induced scintillation light when the MLFD is coupled to the PMT, but not when it is coupled to the SiPM, indicates the generation of Ĉerenkov radiation in the PMT window. This contribution can be misclassified as background gamma-rays and overwhelm the detector response. Additionally, the neutron count rate is also greater in the MLFD-SiPM system possibly due to the lower dead time accounting from the lower gamma-ray count rate. Consequently, the fast neutron detector does not require additional pulse-shape discrimination. Neutron events can be confidently identified by simply setting a threshold to reject background or electronic noise.

Finally, the neutron and gamma-ray detection efficiencies were calculated once again with the MLFD-SiPM system, with a 6 mm long MLFD, the length limited by the dimension of a single SiPM. Listed in Table 6-4 are the detection efficiencies for the MLFD-PMT, MLFD-SiPM systems, and Hornyak Button.

The importance of setting an appropriate LLD is emphasized in the efficiencies reported in Table 6-2 versus Table 6-4. The LLD used in calculating the efficiency values in Table 6-2 were determined using an LLD (at channel 21) before using PSD to determine the portion of neutrons discounted or gamma-ray events included in the neutron detection efficiency. The LLD was set too low, thereby including false positives in the efficiency value. The method of using ^{137}Cs to set an LLD in an MLFD-PMT system is not favorable in reducing gamma-ray insensitivity of the detection system, because the MLFD is not linearly calibrated for gamma-rays. Therefore, although PSD is not required by the MLFD to discriminate gamma-ray events, it is required to set an appropriate LLD, which can be performed during detector calibration and does not require to be included in the detection system itself. In Table 6-4, the LLD was set by using PSD to determine the channel beyond which gamma-ray counts are zero. This LLD is at a higher channel for the MLFD-PMT system as compared to the MLFD-SiPM system due to the former contributing to a greater number of Cerenkov photons in the spectrum.

Table 6-4. Detection efficiencies of the MLFD-SiPM system. A bare ^{252}Cf (32,279 neutrons/s) was used as the neutron and gamma-ray source, while ^{137}Cs (125,800 γ/s) was used as the gamma-ray source.

Detection System (6 mm MLFD)		Fast Neutron Det. Efficiency	γ-Ray Det. Efficiency
	MLFD-PMT	0.85%	1.2×10^{-6}

With PSD	MLFD-SiPM	1.02%	-
Without PSD (LLD)	MLFD-PMT	0.62%	2.4×10^{-5}
	MLFD-SiPM	1.01%	-
Hornyak Button (25.4 mm), with PSD	PMT	0.4%	10^{-6}

6.4 Directional Nature of the MLFD

In section 3.1.2, MCNP models showed that irradiating the MLFD parallel to the photodetector orientation (front irradiation) resulted in a higher count rate than irradiating perpendicular to the photodetector orientation (side irradiation). However, higher energies were deposited in the ZnS:Ag layer for the side irradiation as compared to front irradiation. To validate this phenomenon experimentally, the MLFD-SiPM system was irradiated from the front and sides with a ^{252}Cf source. The neutron counts were found to be higher for the front irradiation than for the side irradiation. On the other hand, the maximum energy deposited in the crystal (corresponding to the maximum light output) was highest the side irradiation, and least for the front irradiation. These experimental observations validate the simulated results (Figure 6-25), and are expected, because for side irradiation, the neutrons and protons encounter more PMMA than ZnS:Ag, respectively, hence deposit higher fraction of energies, but light output is lesser due to lesser interaction with ZnS. On the front face, the amount of neutron energy transferred in the PMMA is lesser, because of the intervening layers of ZnS, hence the maximum energy deposited is lesser. However, due to the greater amount of ZnS that the protons encounter, the total light emitted is much higher, even for the lower energy depositions. The simulations and experiments were both conducted on a two-dimensional plane. If the source irradiates the top of the MLFD, such that it is perpendicular to the photodetector face, then gamma-ray and Ĉerenkov contribution will be considerably higher due to the photodetector being in the path of the forward-propagational recoil electrons, while the neutron counts will be lower due to the layers no longer contributing their advantageous functions as compared to when the radiation strikes on the front face.

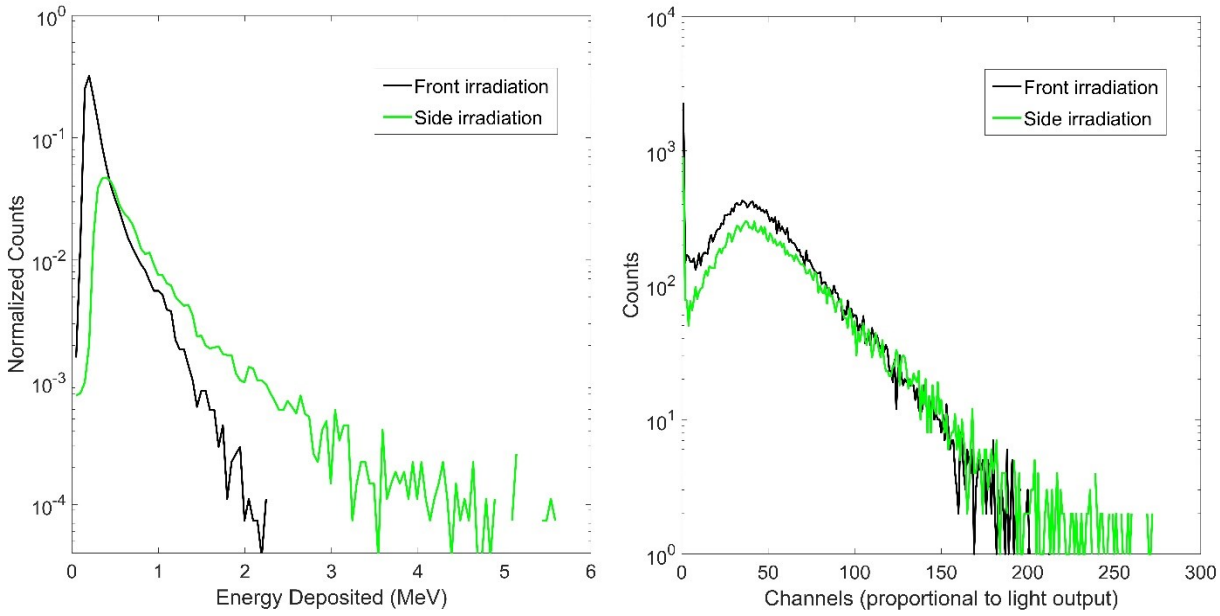

Figure 6-25. Front- and side-irradiation of the MLFD by a bare ^{252}Cf source from MCNP simulation results (left), and experimental results (right).

6.5 MLFD-SiPM Array

The MLFD-SiPM was shown to be gamma-insensitive with a relatively low LLD. These results showed promise for the applicability of the MLFD-SiPM system in SNM searches in high-flux environments. To test this hypodissertation, an array of 4 SiPMs in a 2 × 2 fashion was tested as a "pixel"-type imager.

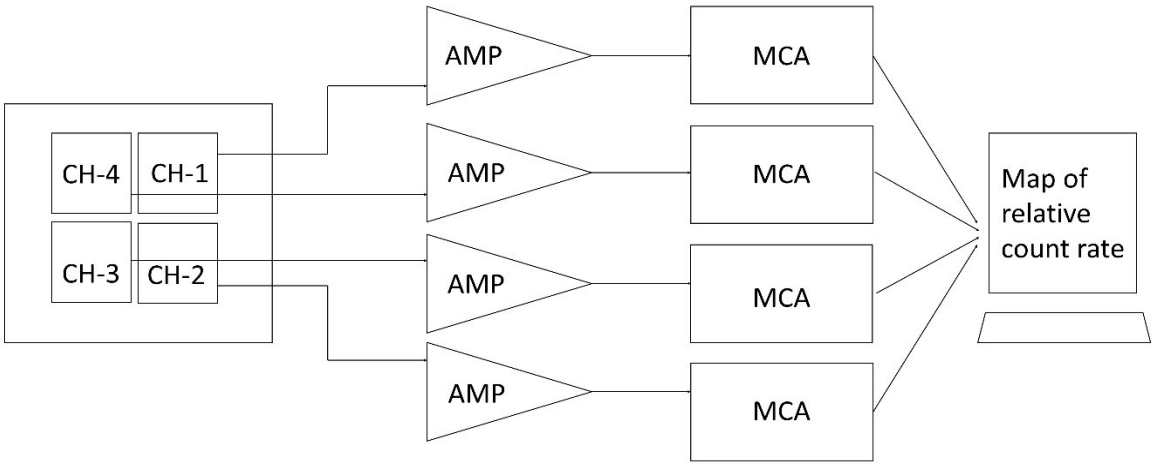

Figure 6-26. Electronic schematic diagram of the experimental setup of the MLFD-SiPM array system.

The 4 SiPMs each had a separate, individual output (1 V max.) which were connected to 4 corresponding amplifiers, and MCAs acting as counters as well as to record spectra (Figure 6-26. Electronic schematic diagram of the experimental setup of the MLFD-SiPM array system.). All the amplifiers and MCAs were checked to be performing uniformly. A 12× amplification was applied in order to fully occupy the 12 V range of the MCAs. 4096 channels were used to allow a modestly low LLD. At first, a background was run to establish the LLD for electronic and background noise, found to be 16 for all four channels (or SiPMs). Next, ^{137}Cs having the same activity as a ^{252}Cf was used to irradiate the array, yet the LLD for gamma rays remained at 16 (see Figure 6-27). This was expected, as per previously found results. Finally, a ^{252}Cf source was placed 5 cm away from the SiPM array center. As can be seen in Figure 6-27, the background and gamma-ray spectra almost exactly overlap, and the same LLD can be used for both. Once again, this result is expected, because a background pulse and a gamma-ray pulse were observed to have the same amplitude and tail for the MLFD-SiPM system (Figure 6-22). The count rate for the gamma-ray spectra was slightly higher than the background spectra (Table 6-5). The count rate for the ^{252}Cf spectra was also only slightly higher than the ^{137}Cs spectra up to LLD 16, indicating that the chosen LLD was sufficient to reject 100% of gamma-rays, while also not discounting a large portion of the neutrons — without requiring PSD.

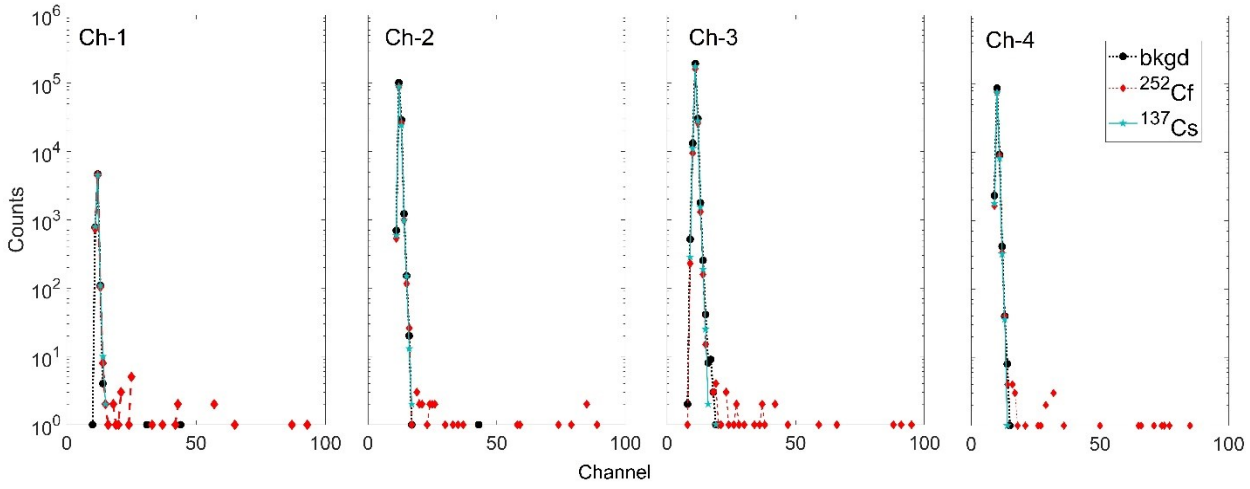

Figure 6-27. Spectra from all 4 channels upon irradiation with a bare ^{252}Cf, ^{137}Cs matching the activity of the ^{252}Cf, and without any source (background).

Table 6-5. Count rates for various sources with respect to the LLD applied.

Source of radiation	Count rate up to LLD 16 (avg. of 4 channels), cps	Count rate above LLD 16 (avg. of 4 channels), cps
Background and electronic	222.56 ± 0.61	0
^{137}Cs	231.67 ± 0.62	0
^{252}Cf	235.33 ± 0.63	0.08 ± 0.012

The fast-neutron response was measured for five distances from the edge of the SiPM array: 2.5 cm, 3 cm, 6 cm, 12 cm and 18 cm, for 10 minutes each, as shown in Figure 6-28. The count rate decreased with distance due to the decrease in solid angle between the source and the MLFD. At a distance of 18 cm, the count rate dropped to 0.002 cps (average of all 4 channels), with channel 4 having recorded 0 counts in 10 minutes. The LLD was kept at channel 16, at which the background count rate was 0.

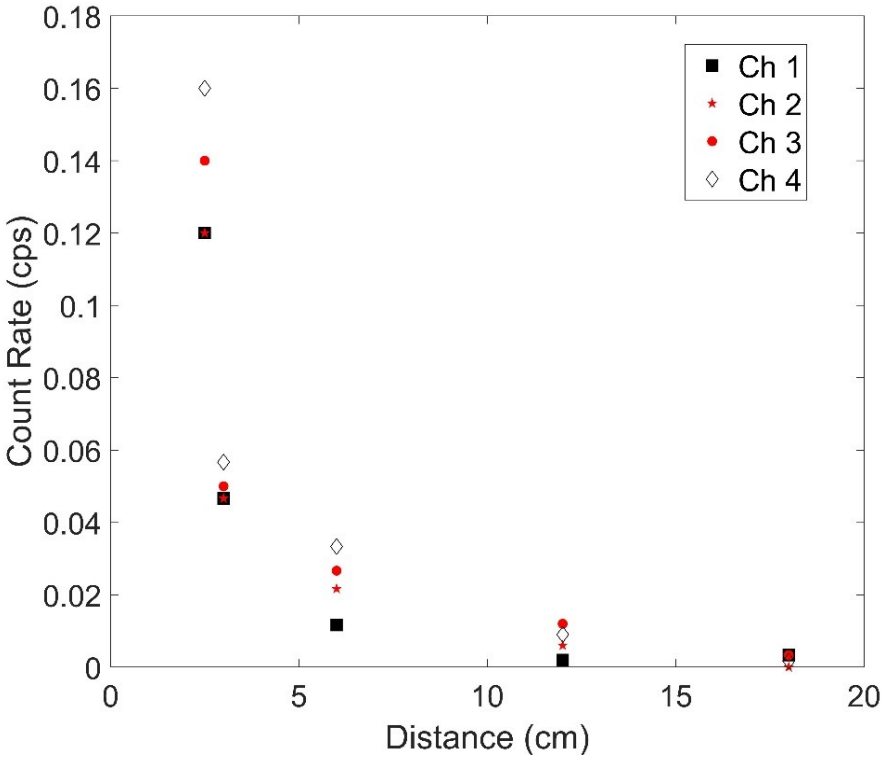

Figure 6-28. Count rate for a bare ^{252}Cf source above LLD. The background and gamma-ray count rates are both zero at this LLD.

6.5.1 Neutron Source Location: Imaging Performance

A Job file was written (Appendix-#7) for Maestro to save spectra collected by the MCA for a specified amount of time, looping over a specified number of times. The Job file allows one to collect data over a given period during which the target may have moved, and therefore provides real-time data of the neutron source location. A MATLAB code was written (Appendix 8) to extract the counts from the Job files' spectra and to construct a map of the relative count rate for each channel (i.e., SiPM). The map would be used to indicate the location of the neutron source corresponding to the channel with the highest relative count rate. To determine the minimum time required by the SiPM array to correctly predict the direction of location of the neutron source, the neutron source was placed at several locations with varying source-to-detector distances, and the map was generated for varying lengths of time.

Directional dependence of MLFD response

For the source placed 5 cm away from the center of the MLFD-SiPM array, enough data was collected in 30 seconds to produce a correct prediction of the source location. Therefore, the 4-SiPM array can refresh real-time data every 30 seconds. The ^{252}Cf was placed in 8 different locations with respect to the MLFD-SiPM array (shown in Figure 6-29): top, top right, right, bottom right, bottom, bottom left, left and top left. A 30-second measurement was run for each location, all of them 5 cm from the center of the array. Four ^{137}Cs and four ^{60}Co sources were randomly strewn around the MLFD-SiPM array in order to emulate a background of gamma radiation. The color maps indicate the direction of location of the neutron source. Yellow indicates the highest count rate relative to the other channels, while redder hues indicate a lower relative count rate.

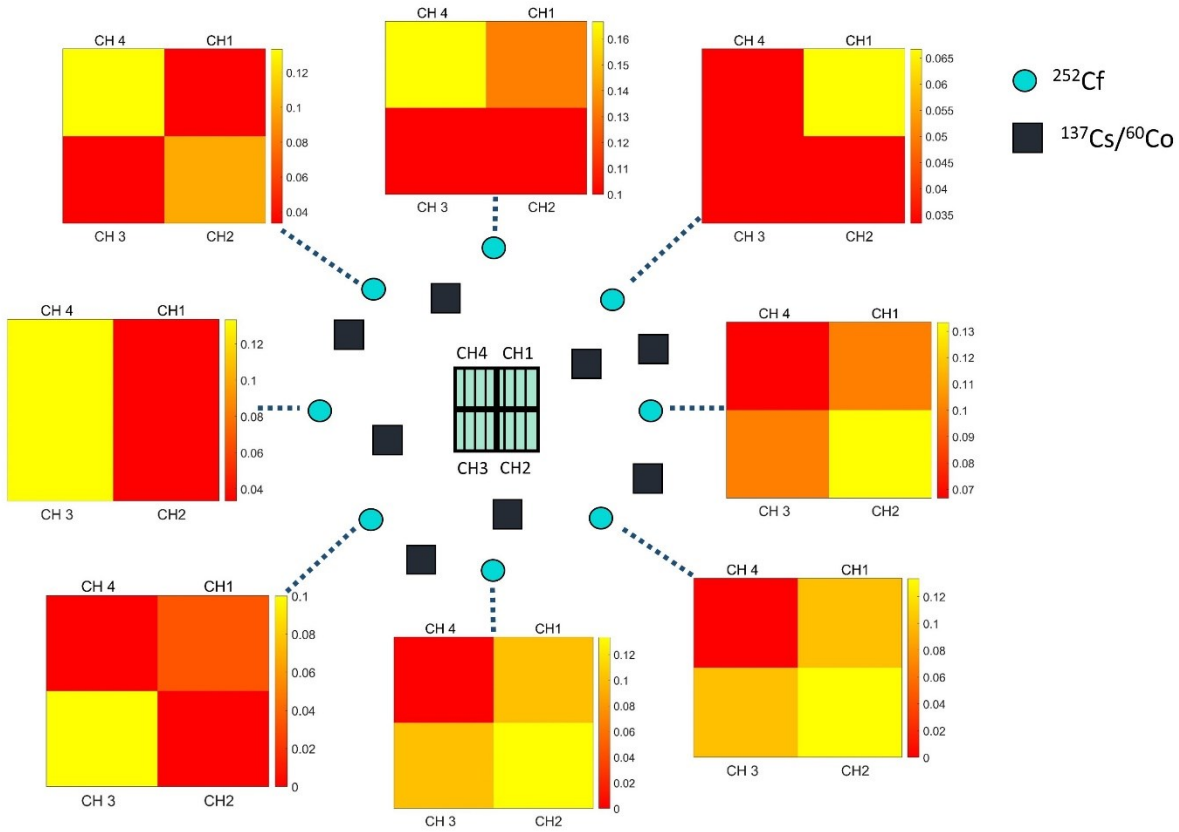

Figure 6-29. Map showing relative count rates using color intensities for each of the 4 channels to indicate location of neutron source, four 8 different locations, in a 30-second interval. The colorbars next to the map indicate count rates.

The source-to-detector distance was increased to 6 cm, and then to 18 cm, which is the previously-established maximum allowable distance for the imaging system to be able to record counts above background in an extended timeframe of 10 minutes. However, the minimum time required to correctly predict the source location would be higher than this value, since the count rate at this distance might not be sufficient for the 4 channels to record enough data to predict the source location. The measurement time was increased from 10 minutes until the imager successfully predicted the neutron source location, with gamma-ray sources also present, for 10 consecutive runs. Shown in Table 6-6 are the minimum times required for the MLFD-SiPM array to correctly determine the neutron source location, predicted correctly for 10 consecutive measurements.

Table 6-6. Minimum times required to correctly predict the source location.

Source-to-detector distance (cm)	Minimum time for data collection to correctly predict source location
3	30 seconds
6	5 minutes
18	20 minutes

Chapter 7 - Conclusions

A novel technology has been developed and characterized for fast-neutron detection in a mixed radiation environment. Manufacturing the Micro-Layered Fast-Neutron Detector (MLFD) is straightforward, and the devices can be mass-produced inexpensively. The main features of the MLFD includes:

- High-efficiency fast-neutron detection; efficiency scalable by simply adding layers
- Suitable for mixed radiation environments due to maximum background rejection without requiring any additional techniques or electronics
- Suitable for high flux radiation environment due to being low-noise and low- Ĉerenkov contaminated
- Compact, portable design
- High-reliability data due to low false positives and minimal discarding of neutron pulses

Fast-neutron detectors have historically suffered from low detection efficiency, additional gamma-ray rejection electronics, overwhelmed detector response at high radiation fluxes, and Ĉerenkov contamination in the signal. Most notably, the Hornyak Button was used at TREAT to image the fuel motion during simulated accident conditions. However, its detection efficiency was low, and the count rates at high reactor power levels were not reliable due to Ĉerenkov radiation dominating the counts. Plastic scintillators have become popular in recent years, however, they usually require additional devices for pulse shape discrimination and therefore complicate the detection system.

The MLFD is a proton-recoil scintillator that uses ZnS:Ag as the scintillating medium and PMMA as the neutron converter. ZnS:Ag has not been widely used due to its self-absorption of light, thus reducing light output. However, the MLFD uses a layered geometry to circumvent the optical absorption and allows one to harness the positive traits of the material, such as high light yield for heavy, charged particles, and low conversion efficiency for fast electrons. The PMMA doubles as a light guide for the photons. In addition, the layered geometry reduces the probability

of Ĉerenkov radiation collection by orienting the photodetector parallel to the neutron beam along the longest length of the MLFD. The neutron detection efficiency can be scaled by simply increasing the number of layers, which was found to be 9.2% for a bare, ^{252}Cf source at 43 mm length of the MLFD.

The MLFD was found to be inherently insensitive to gamma-rays, especially when coupled to SiPMs. When coupled to a PMT, the PMT photocathode window can generate Ĉerenkov radiation from the gamma-ray background, and contaminate the signal. Pulse-shape discrimination is not required for a MLFD-SiPM system, and a low LLD is sufficient to reject background noise and gamma-rays. In fact, even with a PMT, the PSD ratio was found to be 4.56. It is the ZnS:Ag that is responsible for such a clear separation of neutron-induced signals from the gamma-ray ones, because the proton decay time is 700 ns (fastest) and 10 μs (slowest), while the electron decay time is 10 ns. Even in high radiation fields of about 1000 mR/hr, the MLFD performance remains above acceptable values (minimum acceptable is 1.27) with minimal degradation. Furthermore, the MLFD outperforms plastic scintillators in discriminating between neutrons and gamma rays. However, the presence of the epoxy is detrimental to the neutron detection efficiency of the MLFD due to a reduction in total hydrogenous material from an "ideal" model that does not include epoxy.

The MLFD is easy and inexpensive to mass-produce in a short amount of time, requiring widely-available equipment and materials. The fabrication method is a simple four-step established process, and does not require a clean room or any specialized machinery.

When the neutron beam direction is known, the MLFD works well as a fast-neutron detector, and is thus suitable for fuel motion imaging at facilities such as the TREAT Hodoscope. Additional electronics are not required for pulse shape discrimination, and a low LLD is sufficient to reject the majority of gamma-rays. A PMT will work for smaller lengths of the MLFD, but if long lengths of the MFLD are required, an array of SiPMs is the more compact choice of photodetector. A 43-mm MLFD has a fast-neutron detection efficiency of 9.2%. Ĉerenkov events are minimized in two aspects: their generation is reduced by having lesser PMMA, and their collection is further reduced by having intervening ZnS:Ag layers, and most importantly, by collecting light from the sides. At higher power levels, the parallel-to-beam PMT orientation

significantly prevents Ĉerenkov events and therefore allows the MLFD to have a linear response. If SiPMs are used, a low LLD can be used to achieve a gamma-ray detection efficiency of 0%.

If the source location is unknown, as is the case for SNM searches, the MLFD-SiPM array imager was shown to accurately predict neutron source location in a mixed radiation field of gamma rays and neutrons. A proof-of-concept was developed with just four SiPMs, which was able to correctly determine the direction of neutron source within 5 cm in a 30-second measurement interval, in a background of gamma radiation. For distances up to 18 cm, 20-minute intervals are required. The MLFD-SiPM array imager does not require any additional electronics for pulse shape discrimination, hence it is a small, compact, lightweight imager which can be carried around with ease and discretion.

The Future of the Micro-Layered Fast-Neutron Detector

The MLFD is a very promising, new technology that has been developed to TRL-6. If commercialization is desired for deployment, the next step would be to mass-produce the MLFD using the established procedure detailed in this dissertation, and test it in a simulated or real-world environment.

The MLFD-SiPM array imaging system produced results that warrants further engineering of the device to build a more effective, compact and portable system. Currently, the imager requires a minimum of 30 seconds to accurately determine source location. Ideally, the imager should have a convergence time of under one second to compete with existing technology. The PCB can house an amplifier and counter, as well as an on-board digital display that can be programed easily using an Arduino to show a colormap similar to the one shown in the previous chapter. A larger number of SiPMs would further improve the neutron count rate, improve the image resolution, the minimum time required to detect position, and be able to locate sources at farther distances, allowing a closer real-time mapping of source movement. Caution must be exercised if using more than one SiPM as a single unit (or channel), in which case the summing of SiPM outputs into one channel may lead to increase in electronic noise, and may also lead to noticeable cross-talk between SiPMs, leading to higher errors in counting.

The MLFD-SiPM system was shown to produce low levels of Ĉerenkov events, which is an improvement over the Hornyak Button-PMT system that showed non-linear detector response at high power levels. The reason for this non-linearity was attributed to Ĉerenkov events overwhelming the detector performance at high power, however, this was not verified. Both the Hornyak Button-PMT system as well as the MLFD-SiPM system could be tested at the KSU TRIGA Mk II research nuclear reactor at different power levels to test this theory.

If further research to improve and optimize the performance of the MLFD itself is desired, a first step would be to find ways of increasing the neutron detection efficiency. One such possible step is the use of ZnS-based core/shell quantum dots (QD). QD's are nanometer-scale particles, as compared to the micron-sized particles used in this project, and therefore boast a larger total surface area. A larger surface area, along with QD passivation using a core/shell arrangement, increases the total light yield of the material. If ZnS:Ag micro-grains could be replaced by QD's, the results would be interesting to study. Furthermore, depending on the type of QD used, a large Stoke's shift can cause light self-absorption. To prevent self-absorption, the phenomenon of Forster Resonance Energy Transfer can be implemented using a chromophoric dye.

Another avenue to pursue with the MLFD would be detector calibration. Corelating the channel numbers, or voltage, with the energy of the incident particles was not possible in this study due to the shortage of multiple neutron sources with specific energy emissions. Although a DT-generator was available at K-State, which produces neutrons with energies up to 14 MeV, a second source with a different specific energy is required for calibration. Gamma-ray calibration of the MLFD is not a proper method to calibrate for energy, as the MLFD is designed to *reject* gamma rays.

A third avenue would be to fabricate a MLFD without any epoxy, in order to determine if the epoxy is detrimental to the MLFD performance. Alternatively, existing Geant4 codes can be modified to include the epoxy in the model to numerically verify the effects of epoxy. Furthermore, for SNM search applications, the parabolic geometry should be compared to the standard rectangular geometry, experimentally.

References

[1] "Resumption of Transient Testing," 2013. [Online]. Available at https://www.energy.gov/ne/articles/resumption-transient-testing.

[2] A. de Volpi, R. J. Pecina, R. T. Daly, D. J. Travis, R. R. Stewart, and E. A. Rhodes, "Fast-neutron hodoscope at TREAT: development and operation," 1975. *Nucl. Technol.*, vol. 27, no. 3, pp. 449–487.

[3] M. E. Ellis, K. Duroe, and P. A. Kendall, "Pulse-shape discrimination scintillators for homeland security applications," 2016. *Int. J. Mod. Phys. Conf. Ser.*, vol. 44, no. 2010, pp. 1–11.

[4] D. S. McGregor and J. K. Shultis, *Radiation Detection: Concepts, Methods, and Devices*, 2020. 1st ed., Boca Raton, CRC Press.

[5] "Particle Data Group Summary Data Table on Baryons," 2007. lbl.gov.

[6] "Neutron Energy," undated. [Online]. Available at https://www.nuclear-power.net/nuclear-power/reactor-physics/atomic-nuclear-physics/fundamental-particles/neutron/neutron-energy/.

[7] G. F. Knoll, *Radiation Detection and Measurement*, 2010. 4th ed. New York, John Wiley & Sons, Inc..

[8] D. E. Cullen, "Sampling ENDL Watt Fission Spectra," 2004. U.S. Department of Energy, Lawrence Livermore National Laboratory, Livermore, California.

[9] A. B. Smith, P. R. Fields, and J. H. Roberts, "Spontaneous fission neutron spectrum of ^{252}Cf," 1957. *Phys. Rev.*, vol. 108, no. 2, pp. 411–413.

[10] H. R. Bowman, S. G. Thompson, and J. O. Rasmussen, "Gamma-ray spectra from spontaneous fission of 252Cf," 1964. *Phys. Rev. Lett.*, vol. 12, no. 8, pp. 195–198.

[11] W. C. Roentgen, "Further observations on the properties of x rays," 1897. *Arch. Roentgen Ray*, vol. 3, no. 3, pp. 80–88.

[12] *Database NEA N ENDF/B-VII.1*. .

[13] D. Dawson, R. Fleck, and A. Wadham, "Radiation damage to materials," 1993. Module 4 of Course 228. Available from canteach.candu.org, pp. 1–12.

[14] A. Borisevicha, V. Dormenevb, M. Korjika, D. Kozlova, V. Mechinskya, and R. W. Novotnyb, "Optical transmission radiation damage and recovery stimulation of DSB : Ce inorganic scintillation material Optical transmission radiation damage and recovery stimulation of DSB : Ce^3+ inorganic scintillation material," 2015. *J. Phys. Conf. Ser*, Conference Series 587: 012063.

[15] F. J. Bryant and P. S. Manning, "Radiation damage and decay characteristics of zinc selenide emission bands and their equivalence to zinc sulphide emission bands," 1974. *J. Phys. Chem. Solids*, vol. 35, pp. 97–101.

[16] R. Mao, L. Zhang, R. Zhu, and S. Member, "Optical and scintillation properties of inorganic scintillators in high renergy physics," 2007. in *IEEE Trans on Nucl Sci*, pp. 2285–2291.

[17] https://en.wikibooks.org/wiki/Basic_Physics_of_Nuclear_Medicine/ Scintillation_ Detectors.", undated.

[18] S. Gundacker, R. M. Turtos, E. Auffray, and P. Lecoq, "Precise rise and decay time measurements of inorganic scintillators by means of x ray and 511 keV excitation," 2018. *Nucl. Inst. Methods Phys. Res. A*, vol. 891, no. November, pp. 42–52.

[19] M. J. I. Balmer, K. A. A. Gamage, and G. C. Taylor, “Comparative analysis of pulse shape discrimination methods in a ^{6}Li loaded plastic scintillator,” 2015. *Nucl. Inst. Methods Phys. Res. A*, vol. 788, pp. 146–153.
[20] N. Zaitseva*, B.L. Rupert, I. Pawelczak, A. Glenn, H.P. Martinez, L. Carman, M. Faust, N. Cherepy, and S. Payne.*, “Plastic scintillators with efficient neutron/gamma pulse shape discrimination,” 2012. *Nucl. Inst. Methods Phys. Res. A*, vol. 668, pp. 88–93.
[21] C. E. Dickerman, “Studies of fast reactor core behavior under accident conditions,” 1970. *Nucl. Saf. User*, vol. 11, pp. 195–205.
[22] A. DeVolpi, “Fuel-Motion Diagnostics and Cineradiography", 1982. Technical Report, [Available online]: https://www.osti.gov/servlets/purl/6060946.
[23] L. Ocampo, J. Johnson, S. Thompson, J. Hix, S. Watson, and D. Chichester, “TREAT Fuel Motion Summary Report - SETH A-E Experiments,” 2019. Technical Report, Idaho National Laboratory.
[24] K. Morishima and 33 others., “Discovery of a big void in Khufu’s Pyramid by observation of cosmic-ray muons,” 2017. *Nature*, vol. 552, no. 7685, pp. 386–390.
[25] S. D. Clarke, M. C. Hamel, M. M. Bourne, and S. A. Pozzi, “Detectors for active interrogation applications,” 2017. *Phys. Procedia*, vol. 90, pp. 266–270.
[26] W. Fu, P. Ghosh, M. J. Harrison, D. S. McGregor, and J. A. Roberts, “A Geant4 evaluation of the Hornyak button and two candidate detectors for the TREAT hodoscope,” 2018. *Nucl. Inst. Methods Phys. Res. A*, vol. 889, pp. 39–46.
[27] D. L. Chichester, S. M. Watson, J. T. Johnson, and D. M. Wachs, “The TREAT fast-neutron hodoscope and plans for restoring it to operation,” 2015. in *Transactions of the American Nuclear Society*, pp. 112-377.
[28] J. T. Johnson, S. J. Thompson, S. M. Watson, and D. L. Chichester, “Optimization of a fast neutron scintillator for real-time pulse shape discrimination in the transient reactor test facility (TREAT) hodoscope,” 2016. *IEEE Trans on Nucl Sci*, vol. 75, pp. 5–8.
[29] D. Cester, M. Lunardon, G. Nebbia, L Stevanato, G. Viesti, S. Petrucci, and C. Tintori, “Pulse shape discrimination with fast digitizers,” 2014. *Nucl. Inst. Methods Phys. Res. A*, vol. 748, pp. 33–38.
[30] L. Kui-nian, Z. Xian-Peng, G. Qiang, J. Peng, and T. Geng, “Characterization of the new scintillator — Cs 2 LiYCl 6 :Ce3+*,” 2016. *Chinese Phys. C*, vol. 32, pp. 1–8.
[31] A. Lintereur, J. Ely, J. Stave, and B. Mcdonald, “Neutron and Gamma Ray Pulse Shape Discrimination with Polyvinyltoluene,” 2012. Technical Report, Pacific Northwest National Laboratory.
[32] J. B. Birks, *The Theory and Practice of Scintillation Counting*, 1964. 1st ed., Great Britain, Pergamon Press.
[33] Y. Nishiwaki, T. Tsuruta, and K. Yamazaki, “Detection of fast neutrons by etch-pit method of nuclear track registration in plastics,” 1971. *J. Nucl. Sci. Technol.*, vol. 8, no. 3, pp. 162–166.
[34] A. Piruska, I. Nikcevic, S. H. Lee, C. Ahn, W.R. Heineman, P.A. Limbach, and C.J. Seliskar, “The autofluorescence of plastic materials and chips measured under laser irradiation,” 2005. *Lab Chip*, vol. 5, no. 12, pp. 1348–1354.
[35] A. Datta, S. Biswas, S. Kar, and S. Chaudhuri, “Multicolor luminescence from transition metal ion (Mn 2 + and Cu 2 +) doped ZnS nanoparticles,” 2007. *J. Nanosci. Nanotechnol.*, vol. 7, pp. 3670–3676.
[36] P. H. Borse, N. Deshmukh, R. F. Shinde, S. K. Date, and S. K. Kulkarni, “Luminescence

quenching in ZnS nanoparticles due to Fe and Ni doping," 1999. *J. Mater. Sci.*, vol. 34, pp. 6087–6093.
[37] D. Qin, G. Yang, G. He, L. I. Zhang, Q. Zhang, and L. Li, "The investigation on syndissertation and optical properties of Ag-doped ZnS nanocrystals by hydrothermal method," 2012. *Chalcogenide Lett.*, vol. 9, no. 11, pp. 441–446.
[38] S. K. Lee *et al.*, "Comparison of new simple methods in fabricating ZnS(Ag) scintillators for detecting alpha particles," 2011. *Nucl. Sci. Technol.*, vol. 1, pp. 194–197.
[39] M. J. Urffer, "Design of a Neutron Detector Capable of Replacing He-3 Detectors Utilizing Thin Polymeric Films," 2012. The University of Tennessee, Knoxville.
[40] J.N. Abdurashitov, V.N. Gavrin, A.V. Kalikhov, V.L. Matushko, V.E. Yants, O.S. Zaborskaia, J.M. Adams, J.S. Nico, and A.K. Thompson, "A high resolution, low background fast neutron spectrometer," 2002. *Nucl. Inst. Methods Phys. Res. A*, vol. 476, pp. 318–321.
[41] S. S. Kapoor and V. S. Ramamurthy, *Nuclear Radiation Detectors*, 1986. New Delhi, India, Wiley Eastern Ltd..
[42] A. Karellas and B. R. Thomadsen, *Scintillation Dosimetry*, 2016. Boca Raton, CRC Press.
[43] M. A. Clift, R. A. Sutton, and D. V Webb, "Dealing with Cerenkov radiation generated in organic scintillator dosimeters by bremsstrahlung beams," 2000. *Phys. Med. Biol.*, vol. 45, pp. 1165–1182.
[44] W. Fu, "Modeling and simulation of neutron detectors for the transient reactor test facility," 2019. Kansas State University.
[45] H. J. M. Chichester, "Advanced Fuels Campaign In-reactor InstrumentationOverview." 2015. Technical Report, Advanced Sensors and Instrumentation, Department of Energy.
[46] M. Meshkian, "Monte Carlo simulation of a fast neutron counter for use in neutron radiography," 2015. *Nucl. Inst. Methods Phys. Res. A*, vol. 788, pp. 73–78.
[47] P. Ghosh, W. Fu, M. J. Harrison, P. K. Doyle, J. A. Roberts, and D. S. Mcgregor, "Factors affecting performance of the micro-layered fast-neutron detector," 2020. *Nucl. Inst. Methods Phys. Res. A*, vol. 954.
[48] R. A. Leathers, T. V Downes, C. O. Davis, and C. D. Mobley, "Monte Carlo Radiative Transfer Simulations for Ocean Optics: A Practical Guide," 2004. Technical Report, Naval Research Laboratory.
[49] Q. Liu, M. Guobing, and A. Jianping, "Chemical bath-deposited ZnS thin films : Preparation and characterization," 2008. *Appl. Surf. Sci.*, vol. 254, pp. 5711–5714.
[50] J. A. Roberts, M. J. Harrison, W. Fu, P. Ghosh, and D. S. McGregor, "Fast-neutron detector developments for the TREAT hodoscope," 2019. *Radiat. Phys. Chem.*, vol. 155, pp. 184–190.
[51] D. S. McGregor, W. J. Mcneil, S. L. Bellinger, T. C. Unruh, and J. K. Shultis, "Microstructured semiconductor neutron detectors," 2009. *Nucl. Inst. Methods Phys. Res. A*, vol. 608, pp. 125–131.
[52] P. Ghosh, W. Fu, R. Fronk, D. S. McGregor, and J. A. Roberts, "Evaluation of MSNDs for fast-neutron detection and the TREAT hodoscope," 2016. In *Trans. Amer. Nucl. Soc, vol. 115*, pp. 1009–1012.
[53] M. A. Reichenberger, T. Ito, P.B. Ugorowski, B.W. Montag, S.S. Stevenson, D.M. Nichols, and D.S. McGregor, "Electrodeposition of uranium and thorium onto small platinum electrodes," 2016. *Nucl. Inst. Methods Phys. Res. A*, vol. 812, pp. 12–16.

[54] P. Ghosh, W.Fu, M.J. Harrison, P.K. Doyle, N.S. Edwards, J.A. Roberts, and D.S. McGregor, “A high-efficiency, low-Ĉerenkov Micro-Layered Fast-Neutron Detector for the TREAT hodoscope,” 2018. *Nucl. Inst. Methods Phys. Res. A*, vol. 904, pp. 100–106.
[55] F. A. Danevich, V.V. Kobychev, R.V. Kobychev, H. Kraus, V.B. Mikhailik, V.M. Mokina, and I.M. Solsky, “Impact of geometry on light collection efficiency of scintillation detectors for cryogenic rare event searches,” 2014. *Nucl. Inst. Methods Phys. Res. B: Beam Interact. with Mater. Atoms*, vol. 336, pp. 26–30.
[56] W. R. Leo, *Techniques for Nuclear and Particle Physics Experiments A How-to Approach*, 1994. 2nd ed, Verlag Berlin Heidelberg, Springer.
[57] Y. Koechlin, L. Koch, A. Lansart, and G. Pietri, “Etat actuel du développement des compteurs à scintillation en France,” 1958. In *International Conf. on the Peaceful Uses of Atomic Energy, A/CONF. 15/P/1209*.
[58] T. Asada, M. Masuda, M. Okumura, and J. Okuma, “Decay properties of ZnS(Ag) phosphors,” 1959. *J. Phys. Soc. Japan*, vol. 14, no. 12, p. 1766.
[59] S. Landsberger and N. Tsoulfanidis, *Measurement & Detection of Radiation, 2015*. 4th ed, Boca Raton, CRC Press.
[60] D. Engelkemeir, “Nonlinear response of NaI(Tl) to photons,” 1956. *Rev. Sci. Instrum.*, vol. 27, no. 8, pp. 589–591.
[61] L. Reichhart and 35 others., “Quenching factor for low-energy nuclear recoils in a plastic scintillator,” 2012. *Phys. Rev.*, vol. C85, pp. 1–7.
[62] J. E. Turner, *Atoms, Radiation, and Radiation Protection*, 2007. 3rd ed., Wiley-VCH.
[63] C. Allwork, S. Pitts, Z. Wang, and C. L. Morris, “Neutron efficiency and gamma rejection performance of CLYC and 3 He alternative technologies,” 2015. *IEEE Trans on Nucl Sci*.
[64] C. Allwork, A. Kennington, M. Ellis, M. P. Taggart, and P. J. Sellin, “The effect of digitizer properties on the pulse shape discrimination performance of CLYC,” 2015. *IEEE Trans on Nucl Sci*, pp. 1-5.
[65] A. Jančár, Z. Kopecky, J. Dressler, M. Veškrna, Z. Matěj, C. Granja, and M. Solar, “Pulse-shape discrimination of the new plastic scintillators in neutron–gamma mixed field using fast digitizer card,” 2015. *Radiat. Phys. Chem. J.*, vol. 116, pp. 60–64.
[66] P. Ghosh, D. Laramore, and D. S. McGregor, “Characterization and pulse-shape discrimination of a multi-Stacked structure of ZnS:Ag/PMMA for fast-neutron detection in high-flux environments,” *Nucl. Inst. Methods Phys. Res. A*, vol. 984, 2020.
[67] C. Payne, P.J. Sellin, M. Ellis, K. Duroe, A. Jones, M. Joyce, G. Randall, and R. Speller , 2015. “Neutron / gamma pulse shape discrimination in EJ-299-34 at high flux,” *IEEE Trans on Nucl Sci*.
[68] P. Ghosh, D. M. Nichols, W. Fu, J. A. Roberts and D. S. McGregor, "Gamma-ray rejection of the SiPM-coupled Micro-Layered Fast-Neutron Detector," 2019. *IEEE Nuclear Science Symposium and Medical Imaging Conference (NSS/MIC)*, Manchester, United Kingdom, pp. 1-3.
[69] P. Ghosh, W. Fu, M. J. Harrison, P. K. Doyle, J. A. Roberts, and D. S. Mcgregor, “Progress in Micro-Layered Fast Neutron Detectors,” 2018. *Symposium on Advanced Sensors and Modeling Techniques for Nuclear Reactor Safety*, Mumbai, India.
[70] E. Rutherford and H. Geiger, “An electrical method of counting the number of α-Particles from radio-active substances,” Proc. Royal Soc. London, Series A,vol. 81, No. 546, pp. 141-161, 1908
[71] W.F. Hornyak, “A fast neutron detector,” Rev. Sci. Instrum., vol. 23, pp. 264-267, 1952

Appendix A- Programming Codes

1. G-Code for CNC Milling Machine to cut MLFD rectangles out of mold (shown here for 2 mm of depth)

```
G0 x0 y0 z0
g1 x0 y0 z-1
g1 x-6.175 y0 z-1
g1 x-6.175 y-11.175 z-1
g1 x0 y-11.175 z-1
g1 x0 y0 z-1
g1 x6.175 y0 z-1
g1 x6.175 y-11.175 z-1
g1 x0 y-11.175 z-1
g1 x12.35 y-11.175 z-1
g1 x12.35 y0 z-1
g1 x6.175 y0 z-1
g1 x0 y0 z-1
g1 x0 y0 z-2
g1 x-6.175 y0 z-2
g1 x-6.175 y-11.175 z-2
g1 x0 y-11.175 z-2
g1 x0 y0 z-2
g1 x6.175 y0 z-2
g1 x6.175 y-11.175 z-2
g1 x0 y-11.175 z-2
g1 x12.35 y-11.175 z-2
g1 x12.35 y0 z-2
g1 x6.175 y0 z-2
```

2. MATLAB code for calculating solid angle between the MLFD and ^{252}Cf source

```
aH=4;
bH=1.5  ;
% aH=(15.875/2)+0.065;
% bH=(2.7812/2)+0.065;
dH=(10);
w1 = aH/dH;
w2=bH/dH;
W=Rs/dH;
```

SA_H_circtorec=((w1*w2)/(pi))*(1 - (3/4)*(W^2) - (1/2)*(w1^2+w2^2) + (1/8)*(5*W^4+3*w1^4+3*w2^4) +(5/4)*W^2*(w1^2+w2^2) - (35/64)*W^6 + (5/12)*(w1*w2)^2 - (35/16)*W^4*(w1^2+w2^2) -(7/32)*W^2*(9*w1^4 + 9*w2^4 + 10*w1^2*w2^2) - (7/16)*w1^2*w2^2*(w1^2+w2^2) - (5/16)*(w1^6+w2^6))

3. **MATLAB code to trace optical photons in PMMA. Example code for rectangular geometry with specular reflector:**

```
A = zeros(1000,1);
for whole = 1:1000
   % nr=1000;
   % ar=0;
   % br=6;
   % ar_y=0;
   % br_y=3;
   % i=1;
   % xr=zeros(nr,1);
   % yr=zeros(nr,1);
   % for i=1:nr
   %     xr(i,1)=ar + (br-ar).*rand(1,1);
   %     yr(i,1)=ar_y + (br_y-ar_y).*rand(1,1);
   %
   % end
   % scatter(xr,yr)
   a = 0.0362; % absorption coefficient of plexiglass (1/mm)
   c = 0.03623; % attenuation coefficient of plexiglass(1/mm)
   w0 = .99964; %w0 = (c-a)/c; % single-scattering albedo
   Rb = 1;%Lambertian albedo considering totally reflective surface
   P0 = 1; % source intensity (W)
   N = 12738; % number of photons to trace
   ns = 10; % number of scatters to trace
   %A = 0; % initalize detectors (all photons)
   a1=0;
   b1=6;
   a1y=0;
   b1y=3;
   Abs=0;
   k=0;t=1;l1=1;l2=1;
   flag=0;
   l1=1;l2=1;o=0;
   lambxpos=zeros(N*ns,1);
   lambypos=zeros(N*ns,1);
   detxpos=zeros(N*ns,1);
   detypos=zeros(N*ns,1);
   px=zeros(10000,1);
```

```
    py=zeros(10000,1);
    x=zeros(N,1);
    y=zeros(N,1);
    y_up=zeros(N,1);
    y_low=zeros(N,1);
    countref=0;
    countdet=0;
    ints=zeros(N,1);
    i=1;
    % semicircle
    for i=1:N  % generate points wihtin geomtery of light sources
       x(i)=a1 + (b1-a1).*rand(1,1);
       y(i)=a1y + (b1y-a1y).*rand(1,1);
       z(i)=0;
    end

    for i=1:N
       p=[x(i),y(i),z(i)]; % initial position of isotropic sources (x,y,z)
       x1=p(:,1);
       y1=p(:,2);
    %     hold on;
    %     plot(x(i),y(i),'*')
    %     hold on;
       muz = 1-2*rand; % isotropic source
       phi = 2*pi*rand; % isotropic source
       mux = sqrt(1-muz^2)*cos(phi); % initial x-direction cosine
       muy = sqrt(1-muz^2)*sin(phi); % intitial y-direction cosine
       w = P0; % initial photon weight
       while flag == 0 && w>0.001  %check for till it is absorbed or detected , also && total dist
travelled < allowed
          s = -log(rand)/c;  %geometric path length
          p = p + s*[mux,muy,muz]; % move photon
          x2=p(:,1);
          y2=p(:,2);
          m = (y2-y1)/(x2-x1);
          bb = y1 - m*x1;
          if x1<x2
             t=1;
             k=x1;
             while(k<=x2)
                px(t)=k;
                py(t)=m*px(t)+bb;
                if px(t)>6 || px(t)<0 || py(t)>3
                   countref=countref+1;
                   lambxpos(l1)=px(t-1);
                   lambypos(l1)=py(t-1);
```

```
            %w=w*exp((-c)*sqrt((lambxpos(l1)-x1(i))^2)+(lambypos(l1)-y1(i))^2);
%               hold on;
%               plot([x1,lambxpos(l1)],[y1,lambypos(l1)])
            x1=lambxpos(l1);
            y1=lambypos(l1);
            w=w*Rb;%absorb fraction of photon
            muz = muz;
            phi = 2*pi*rand; % isotropic source
            mux = sqrt(1-muz^2)*cos(phi); % initial x-direction cosine
            muy = sqrt(1-muz^2)*sin(phi); % intitial y-direction cosine
            p=[x1,y1,0];
            l1=l1+1;
            break;
         elseif py(t)<0 && py(t-1)>0
            countdet=countdet+1;
            detxpos(l2)=px(t-1);
            detypos(l2)=py(t-1);
%               hold on;
%               plot([x1,detxpos(l2)],[y1,detypos(l2)])

            w=w*w0;
            Abs=Abs+w;
            ints(i)=w;
            l2=l2+1;
            flag=1;
            break;
         else
            w=w*w0;
            t=t+1;
            k=k+0.01;
         end

      end

   else
      t=1;
      k=x1;
      while(k>=x2)
         px(t)=k;
         py(t)=m*px(t)+bb;
         if px(t)>6 || px(t)<0 || py(t)>3
            countref=countref+1;
            lambxpos(l1)=px(t-1);
            lambypos(l1)=py(t-1);
%               hold on;
%               plot([x1,lambxpos(l1)],[y1,lambypos(l1)])
```

```
            x1=lambxpos(l1);
            y1=lambypos(l1);
            w=w*Rb;
            muz = muz;
            phi = 2*pi*rand; % isotropic source
            mux = sqrt(1-muz^2)*cos(phi);  % initial x-direction cosine
            muy = sqrt(1-muz^2)*sin(phi); % intitial y-direction cosine
            p=[x1,y1,0];
            l1=l1+1;
            break;
         elseif py(t)<0 && py(t-1)>0
            countdet=countdet+1;
            detxpos(l2)=px(t-1);
            detypos(l2)=py(t-1);
%              hold on;
%              plot([x1,detxpos(l2)],[y1,detypos(l2)])

            w=w*w0;
            Abs=Abs+w;
            ints(i)=w;
            l2=l2+1;
            flag=1;
            break;
         else
            w=w*w0;
            k=k-0.01;
            t=t+1;
         end

      end
      if flag == 1
         break;
      end
   end


end
if flag ==1
   flag =0;

end
%Abs=Abs+w;
end
ints(ints==0)=[];
Abs/N;
A(whole)=Abs;
```

```
   %histogram(ints)
end
```

4. MCNP code for simulating proton energy deposition in ZnS:Ag layers for determining directionality of MLFD

```
c filename cell card
1 1 -1.18 -1 imp:n,p,h,e=1
2 3 -4.09 -2 imp:n,p,h,e=1
3 1 -1.18 -3 imp:n,p,h,e=1
4 3 -4.09 -4 imp:n,p,h,e=1
5 1 -1.18 -5 imp:n,p,h,e=1
6 3 -4.09 -6 imp:n,p,h,e=1
7 1 -1.18 -7 imp:n,p,h,e=1
8 3 -4.09 -8 imp:n,p,h,e=1
9 1 -1.18 -9 imp:n,p,h,e=1
10 3 -4.09 -10 imp:n,p,h,e=1
11 1 -1.18 -11 imp:n,p,h,e=1
12 3 -4.09 -12 imp:n,p,h,e=1
13 1 -1.18 -13 imp:n,p,h,e=1
14 3 -4.09 -14 imp:n,p,h,e=1
15 1 -1.18 -15 imp:n,p,h,e=1
16 3 -4.09 -16 imp:n,p,h,e=1
17 1 -1.18 -17 imp:n,p,h,e=1
18 3 -4.09 -18 imp:n,p,h,e=1
19 1 -1.18 -19 imp:n,p,h,e=1
20 3 -4.09 -20 imp:n,p,h,e=1
21 1 -1.18 -21 imp:n,p,h,e=1
22 3 -4.09 -22 imp:n,p,h,e=1
23 1 -1.18 -23 imp:n,p,h,e=1
24 3 -4.09 -24 imp:n,p,h,e=1
25 1 -1.18 -25 imp:n,p,h,e=1
26 3 -4.09 -26 imp:n,p,h,e=1
27 1 -1.18 -27 imp:n,p,h,e=1
28 3 -4.09 -28 imp:n,p,h,e=1
29 1 -1.18 -29 imp:n,p,h,e=1
30 3 -4.09 -30 imp:n,p,h,e=1
31 1 -1.18 -31 imp:n,p,h,e=1
32 3 -4.09 -32 imp:n,p,h,e=1
33 1 -1.18 -33 imp:n,p,h,e=1
34 3 -4.09 -34 imp:n,p,h,e=1
35 1 -1.18 -35 imp:n,p,h,e=1
36 3 -4.09 -36 imp:n,p,h,e=1
37 1 -1.18 -37 imp:n,p,h,e=1
38 3 -4.09 -38 imp:n,p,h,e=1
39 1 -1.18 -39 imp:n,p,h,e=1
```

40 3 -4.09 -40 imp:n,p,h,e=1
41 1 -1.18 -41 imp:n,p,h,e=1
42 3 -4.09 -42 imp:n,p,h,e=1
43 1 -1.18 -43 imp:n,p,h,e=1
44 3 -4.09 -44 imp:n,p,h,e=1
45 1 -1.18 -45 imp:n,p,h,e=1
46 3 -4.09 -46 imp:n,p,h,e=1
47 1 -1.18 -47 imp:n,p,h,e=1
48 3 -4.09 -48 imp:n,p,h,e=1
49 1 -1.18 -49 imp:n,p,h,e=1
50 3 -4.09 -50 imp:n,p,h,e=1
51 1 -1.18 -51 imp:n,p,h,e=1
52 3 -4.09 -52 imp:n,p,h,e=1
53 1 -1.18 -53 imp:n,p,h,e=1
54 3 -4.09 -54 imp:n,p,h,e=1
55 1 -1.18 -55 imp:n,p,h,e=1
56 3 -4.09 -56 imp:n,p,h,e=1
57 1 -1.18 -57 imp:n,p,h,e=1
58 3 -4.09 -58 imp:n,p,h,e=1
59 1 -1.18 -59 imp:n,p,h,e=1
60 3 -4.09 -60 imp:n,p,h,e=1
61 1 -1.18 -61 imp:n,p,h,e=1
62 3 -4.09 -62 imp:n,p,h,e=1
63 1 -1.18 -63 imp:n,p,h,e=1
64 3 -4.09 -64 imp:n,p,h,e=1
65 1 -1.18 -65 imp:n,p,h,e=1
66 3 -4.09 -66 imp:n,p,h,e=1
67 1 -1.18 -67 imp:n,p,h,e=1
68 3 -4.09 -68 imp:n,p,h,e=1
69 1 -1.18 -69 imp:n,p,h,e=1
70 3 -4.09 -70 imp:n,p,h,e=1
71 1 -1.18 -71 imp:n,p,h,e=1
72 3 -4.09 -72 imp:n,p,h,e=1
73 1 -1.18 -73 imp:n,p,h,e=1
74 3 -4.09 -74 imp:n,p,h,e=1
75 1 -1.18 -75 imp:n,p,h,e=1
76 3 -4.09 -76 imp:n,p,h,e=1
77 1 -1.18 -77 imp:n,p,h,e=1
78 3 -4.09 -78 imp:n,p,h,e=1
79 1 -1.18 -79 imp:n,p,h,e=1
80 3 -4.09 -80 imp:n,p,h,e=1
81 1 -1.18 -81 imp:n,p,h,e=1
82 3 -4.09 -82 imp:n,p,h,e=1
83 1 -1.18 -83 imp:n,p,h,e=1
84 3 -4.09 -84 imp:n,p,h,e=1
85 1 -1.18 -85 imp:n,p,h,e=1

```
86 3 -4.09 -86 imp:n,p,h,e=1
87 1 -1.18 -87 imp:n,p,h,e=1
88 3 -4.09 -88 imp:n,p,h,e=1
89 1 -1.18 -89 imp:n,p,h,e=1
90 3 -4.09 -90 imp:n,p,h,e=1
91 1 -1.18 -91 imp:n,p,h,e=1
92 3 -4.09 -92 imp:n,p,h,e=1
93 1 -1.18 -93 imp:n,p,h,e=1
94 3 -4.09 -94 imp:n,p,h,e=1
95 1 -1.18 -95 imp:n,p,h,e=1
96 3 -4.09 -96 imp:n,p,h,e=1
97 1 -1.18 -97 imp:n,p,h,e=1
98 3 -4.09 -98 imp:n,p,h,e=1
99 1 -1.18 -99 imp:n,p,h,e=1
100 3 -4.09 -100 imp:n,p,h,e=1
c
200 2 -0.0012 1 2 3 4 5 6 7 8 9 10 11 12 13 14 15 16 17 18 19
    20 21 22 23 24 25 26 27 28 29 30 31 32 33 34 35 36 37 38
    39 40 41 42 43 -199 imp:n,p,h,e=1
201 0 199 imp:n,p,h,e=0

c surface card
1 RPP -.4 .4 -.15 .15 0 .02
2 RPP -.4 .4 -.15 .15 0.02 .0212
3 RPP -.4 .4 -.15 .15 .0212 .0412
4 RPP -.4 .4 -.15 .15 0.0412 .0424
5 RPP -.4 .4 -.15 .15 .0424 .0624
6 RPP -.4 .4 -.15 .15 0.0624 .0636
7 RPP -.4 .4 -.15 .15 .0636 .0836
8 RPP -.4 .4 -.15 .15 0.0836 .0848
9 RPP -.4 .4 -.15 .15 .0848 .1048
10 RPP -.4 .4 -.15 .15 0.1048 .1060
11 RPP -.4 .4 -.15 .15 0.1060 .1260
12 RPP -.4 .4 -.15 .15 0.1260 .1272
13 RPP -.4 .4 -.15 .15 0.1272 .1472
14 RPP -.4 .4 -.15 .15 0.1472 .1484
15 RPP -.4 .4 -.15 .15 0.1484 .1684
16 RPP -.4 .4 -.15 .15 0.1684 .1696
17 RPP -.4 .4 -.15 .15 0.1696 .1896
18 RPP -.4 .4 -.15 .15 0.1896 .1908
19 RPP -.4 .4 -.15 .15 0.1908 .2108
20 RPP -.4 .4 -.15 .15 0.2108 .2120
21 RPP -.4 .4 -.15 .15 0.2120 .2320
22 RPP -.4 .4 -.15 .15 0.2320 .2332
23 RPP -.4 .4 -.15 .15 0.2332 .2532
24 RPP -.4 .4 -.15 .15 0.2532 .2544
```

```
25 RPP -.4 .4 -.15 .15 0.2544 .2744
26 RPP -.4 .4 -.15 .15 0.2744 .2756
27 RPP -.4 .4 -.15 .15 0.2756 .2956
28 RPP -.4 .4 -.15 .15 0.2956 .2968
29 RPP -.4 .4 -.15 .15 0.2968 .3168
30 RPP -.4 .4 -.15 .15 0.3168 .3180
31 RPP -.4 .4 -.15 .15 0.3180 .3380
32 RPP -.4 .4 -.15 .15 0.3380 .3392
33 RPP -.4 .4 -.15 .15 0.3392 .3592
34 RPP -.4 .4 -.15 .15 0.3592 .3604
35 RPP -.4 .4 -.15 .15 0.3604 .3804
36 RPP -.4 .4 -.15 .15 0.3804 .3816
37 RPP -0.4 0.4 -0.15 0.15 0.3816 0.4016
38 RPP -0.4 0.4 -0.15 0.15 0.4016 0.4028
39 RPP -0.4 0.4 -0.15 0.15 0.4028 0.4228
40 RPP -0.4 0.4 -0.15 0.15 0.4228 0.424
41 RPP -0.4 0.4 -0.15 0.15 0.424 0.444
42 RPP -0.4 0.4 -0.15 0.15 0.444 0.4452
43 RPP -0.4 0.4 -0.15 0.15 0.4452 0.4652
199 SO 50

c data card
mode n p h e
PHYS:N 100 0 0 J J J 1 -1 J J J 0 0
PHYS:H 100 0 -1 J 0 J 1 J J J 0 0 0 0.917
CUT:H j 0.001
F4:N 1  //cellular flux tally
E4 1 1000i 11  //binning mev energy
F6:H 1  //energy deposition
c F8:N 1  //pulse height tally
c FT8 PHL 1 6 1
c E8 0 400i 20
c F16:N 2
c F18:N 2
c FT18 PHL 1 16 1
c E18 0 400i 20
c F26:H 3
c F28:N 3
c FT28 PHL 1 26 1
c E28 0 400i 20
c
F8:N 1 2 3 4 5 6 7 8 9 10 11 12 13 14 15
     16 17 18 19 20 21 22 23 24 25 26 27
     28 29 30 31 32 33 34 35 36 37 38 39
     40 41 42 43
E8   0 400i 20
```

```
F48:H 2 4 T
E48  0 400i 20
SDEF POS 0 0 0 par=N wgt=37000
M1   6000.70c 5
     8016.70c 2
     1001.70c 8
M2   7014.70c -0.7809
     8016.70c -0.2095
     6000.70c -0.0004
c    18049.70c -0.0.0093
M3   30065.70c  1
     16032.70c  1
print
nps 1E9  //relative error 20%
```

5. Extracting pulses from digitizer and performing pulse shape discrimination on the pulses to sort them into “neutron” piles and “gamma-ray” piles in MATLAB

```
clear;
clc;
wave = xlsread('30040_167');
num = wave(:,1);
w = wave(:,2);
long = wave(:,4);
short = wave(:,5);
chargeL=0;
chargeS=0;
n=100;
k1=1;
k2=1;
k=1;
na=1;
ga=1;
neu= zeros(6000,1);
gam= zeros(6000,1);
for j=1:n
for i=k:k+5999
  if long(i)==8000
     QL=0;
  else
     QL=8007-w(i);
  end
  chargeL = chargeL + QL;
  if short(i)==8000
```

```
      QS=0;
   else
      QS=8007-w(i);
   end
   chargeS = chargeS + QS;
end
PSD(j) = (chargeL-chargeS)/chargeL;
if PSD(j) >= 0.56
    for i=k:k+5999
       neutron(k1,na) = w(i);
       number1(k1,na) = num(i);
       k1=k1+1;

    end
      na=na+1;
      k1=1;

else
    for i=k:k+5999
       gamma(k2,ga) = w(i);
       number2(k2,ga) = num(i);
       k2=k2+1;
    end
    ga=ga+1;
    k2=1;

end
k=k+6000;
chargeL=0;
chargeS=0;
end
for x=1:6000
    for y=1:na-1
       neu(x)=neu(x)+neutron(x,y);
    end
    neu(x)=neu(x)/(na-1);
end
for x=1:6000
    for y=1:ga-1
       gam(x)=gam(x)+gamma(x,y);
    end
    gam(x)=gam(x)/(ga-1);
end
filename = 'Neutron.xlsx';
xlswrite(filename,neu,'Sheet1','B2');
xlswrite(filename,number1(:,1),'Sheet1','A2');
```

```
q = {'Wave'};
r = {'Number'};
xlswrite(filename,q,'Sheet1','B1');
xlswrite(filename,r,'Sheet1','A1');
filename = 'Gamma.xlsx';
xlswrite(filename,gam,'Sheet1','B2');
xlswrite(filename,number2(:,1),'Sheet1','A2');
q = {'Wave'};
r = {'Number'};
xlswrite(filename,q,'Sheet1','B1');
xlswrite(filename,r,'Sheet1','A1');
figure(1);
plot(number2(:,1),gam);
figure(2);
plot(number1(:,1),neu);
```

6. Plotting a PSD map in MATLAB

```
clear;
clc;
psd = xlsread('PSD plots');
e_long = psd(:,2);
psdrat = psd(:,5);
hist3([e_long,psdrat],'NBins',[200,200],'CdataMode','auto','LineStyle','none')
myColorMap = parula(256);
myColorMap(1,:) = 1;
colormap(myColorMap);
colorbar;view(2)
```

7. Creating a Job file for Maestro to save spectra from the MCA

```
SET_DETECTOR 2
SET_PRESET_CLEAR

DESCRIBE_SAMPLE "Sipm Array"
SET_PRESET_REAL 30

LOOP 5
CLEAR
START
WAIT
SAVE "CH2FILNAME_???.SPE"
END_LOOP
SET_PRESET_CLEAR
```

CLEAR

8. **MATLAB code to construct visual map of the count rate response from each of the four SiPMs in the array to determine source location**

```
clc;
clear;
num=5;
ch1data=zeros(4094,num);
ch2data=zeros(4094,num);
ch3data=zeros(4094,num);
ch4data=zeros(4094,num);
for n = 1:num
   c1 = sprintf('CH1FILNAME_00%d.Spe',n-1);
   ch1dat = importdata(c1,' ',14);
   ch1data(:,n) = ch1dat.data;
   c2 = sprintf('CH2FILNAME_00%d.Spe',n-1);
   ch2dat = importdata(c2,' ',14);
   ch2data(:,n) = ch2dat.data;
   c3 = sprintf('CH3FILNAME_00%d.Spe',n-1);
   ch3dat = importdata(c3,' ',14);
   ch3data(:,n) = ch3dat.data;
   c4 = sprintf('CH4FILNAME_00%d.Spe',n-1);
   ch4dat = importdata(c4,' ',14);
   ch4data(:,n) = ch4dat.data;
   sumch1=sum(ch1data(:,n));
   sumch2=sum(ch2data(:,n));
   sumch3=sum(ch3data(:,n));
   sumch4=sum(ch4data(:,n));
   dev=zeros(2,2);
   dev(1,1)= sumch4/30;
   dev(1,2)= sumch1/30;
   dev(2,1)= sumch3/30;
   dev(2,2)= sumch2/30;
   imagesc(dev);
   axis on;
   colormap(autumn);
   set(gca,'XTick',[]);
   set(gca,'YTick',[]);
   xlabel('CH 3                CH2') ;
   ax = gca;
   ax.FontSize = 18;
   title('CH 4                CH1','FontWeight','Normal')
   colorbar;
   drawnow;
end
```

Appendix B- List of Supporting Publications

P. Ghosh, D. Laramore, and D. S. McGregor, "Characterization and pulse-shape discrimination of a multi-Stacked structure of ZnS:Ag/PMMA for fast-neutron detection in high-flux environments," Nucl. Instruments Methods Phys. Res. A, p. Vol. 984, 2020.

P. Ghosh, W. Fu, M. J. Harrison, P. K. Doyle, J. A. Roberts, and D. S. Mcgregor, "Factors affecting performance of the micro-layered fast-neutron detector," Nucl. Inst. Methods Phys. Res. A, vol. 954, 2020.

P. Ghosh, D. M. Nichols, W. Fu, J.A. Roberts, D.S. McGregor, "Gamma-Ray Rejection of the SiPM-coupled Micro-Layered Fast-Neutron Detector", IEEE Nuclear Science Symposium and Medical Imaging Conference, 2019.

J. A. Roberts, M. J. Harrison, W. Fu, P. Ghosh, and D. S. McGregor, "Fast-neutron detector developments for the TREAT hodoscope," Radiat. Phys. Chem., vol. 155, 2019.

P. Ghosh, W. Fu, M. J. Harrison, P. K. Doyle, J. A. Roberts, and D. S. Mcgregor, "Progress in Micro-Layered Fast Neutron Detectors," in Symposium on Advanced Sensors and Modeling Techniques for Nuclear Reactor Safety, Mumbai, India, 2018.

P. Ghosh et al., "A high-efficiency, low-Ĉerenkov Micro-Layered Fast-Neutron Detector for the TREAT hodoscope," Nucl. Instruments Methods Phys. Res. A, vol. 904, pp. 100–106, 2018.

W. Fu, P. Ghosh, M. J. Harrison, D. S. McGregor, and J. A. Roberts, "A Geant4 evaluation of the Hornyak Button and two candidate detectors for the TREAT hodoscope," Nucl. Instruments Methods Phys. Res. A, vol. 889, pp. 39–46, 2018.

P. Ghosh, W. Fu, R. Fronk, D. S. McGregor, and J. A. Roberts, "Evaluation of MSNDs for fast-neutron detection and the TREAT hodoscope," in Transactions of the American Nuclear Society 115, 2016, pp. 1009–1012.